FABRICATION AND OPTICAL STUDIES OF AIR-SENSITIVE TWO-DIMENSIONAL MATERIALS

A thesis submitted to the University of Manchester
for the degree of Doctor of Philosophy
in the Faculty of Science and Engineering

2020

By
Daniel J. Terry
School of Natural Sciences
Department of Physics and Astronomy

Contents

Word Count: 34,110

List of Tables

List of Figures

List of Publications

- M. Hamer, E. Tóvári, M. Zhu, M. D. Thompson, A. Mayorov, J. Prance, Y. Lee, R. P. Haley, Z. R. Kudrynskyi, A. Patanè, **D. J. Terry**, Z. D. Kovalyuk, K. Ensslin, A. V. Kretinin, A. Geim and R. Gorbachev, "Gate-defined quantum confinement in InSe-based van der Waals heterostructures", *Nano letters*, vol. 18, no. 6, pp. 3950-3955, 2018

- **D. J. Terry**, V. Zólyomi, M. Hamer, A. V. Tyurnina, D. G. Hopkinson, A. M. Rakowski, S. J. Magorrian, N. Clark, Y. M. Andreev, O. Kazakova, K. Novoselov, S. J. Haigh, V. I. Fal'ko and R. Gorbachev, "Infrared-to-violet tunable optical activity in atomic films of GaSe, InSe, and their heterostructures", *2D Materials*, vol. 5, no. 4, p. 041009, 2018

- N. Leisgang, J. G. Roch, G. Froehlicher, M. Hamer, **D. J. Terry**, R. Gorbachev and R. J. Warburton, "Optical second harmonic generation in encapsulated single-layer InSe", *AIP Advances*, vol. 8, no. 10, p. 105120, 2018

- M. Hamer, J. Zultak, A. V. Tyurnina, V. Zólyomi, **D. J. Terry**, A. Barinov, A. Garner, J. Donoghue, A. P. Rooney, V. Kandyba, A. Giampietri, A. Graham, N. Teutsch, X. Xia, M. Koperski, S. J. Haigh, V. I. Fal'ko, R. Gorbachev and N. R. Wilson, "Indirect to direct gap crossover in two-dimensional InSe revealed by angle-resolved photoemission spectroscopy", *ACS Nano*, vol. 13, no. 2, pp. 2136-2142, 2019

- E. M. Alexeev, D. A. Ruiz-Tijerina, M. Danovich, M. Hamer, **D. J. Terry**, P. K. Nayak, S. Ahn, S. Pak, J. Lee, J. I. Sohn, M. R. Molas, M. Koperski, K. Watanabe, T. Taniguchi, K. Novoselov, R. V. Gorbachev, H. S. Shin, V. I. Fal'ko and A. I. Tartakovskii, "Resonantly hybridized excitons in moiré superlattices in van der Waals heterostructures", *Nature*, vol. 567, no. 7746,

pp. 81-86, 2019

- D. G. Hopkinson, V. Zólyomi, A. P. Rooney, N. Clark, **D. J. Terry**, M. Hamer, D. J. Lewis, C. S. Allen, A. I. Kirkland, Y. Andreev, Z. Kudrynskyi, Z. Kovalyuk, A. Patanè, V. I. Fal'ko, R. Gorbachev, S. J. Haigh, "Formation and healing of defects in atomically thin GaSe and InSe", *ACS Nano*, vol. 13, no. 5, pp. 5112-5123, 2019

- M. Hamer, **D. J. Terry**, R. Gorbachev. UK Patent Application No. 1813343.9 "Electrically Controlled Active Waveguide" Filed: August 2019. The University of Manchester.

- M. R. Molas, A. V. Tyurnina, V. Zólyomi, A. Ott, **D. J. Terry**, M. Hamer, C. Yelgel, A. G. Nasibulin, A. C. Ferrari, V. I. Fal'ko, R. Gorbachev, "Raman spectroscopy of atomically thin GaSe and InSe crystals", under review, 2019

- N. Ubrig, E. Ponomarev, J. Zultak, D. Domaretskiy, V. Zólyomi, **D. J. Terry**, J. Howarth, I. Gutiérrez-Lezama, A. Zhukov, Z. Kudrynskyi, Z. Kovalyuk, A. Patanè, T. Taniguchi, K. Watanabe, R. V. Gorbachev, V. I. Fal'ko, A. F. Morpurgo, "Design of van der Waals interfaces for broad-spectrum optoelectronics", awaiting publication, *Nature Materials*, 2019

- J. Bekaert, E. Khestanova, D. G. Hopkinson, J. Birkbeck, N. Clark, M. Zhu, D. A. Bandurin, R. Gorbachev, S. Fairclough, Y. Zou, M. Hamer, **D. J. Terry**, J. J. P. Peters, A. M. Sanchez, B. Partoens, S. J. Haigh, M. V. Milošević, I. V. Grigorieva, "Enhanced superconductivity in few-layer TaS_2 due to healing by oxygenation", under review, 2019

List of Abbreviations

- 2D - Two-Dimensional
- AFM - Atomic Force Microscopy
- ARPES - Angle-Resolved Photoemission Spectroscopy
- BF - Bright-Field
- BZ - Brillouin Zone
- CB - Conduction Band
- CBM - Conduction Band Minimum
- CVD - Chemical Vapour Deposition
- DF - Dark-Field
- DFT - Density Functional Theory
- DI - Deionised
- DIC - Differential Interference Contrast
- FIB - Focussed Ion Beam
- FWHM - Full Width at Half Maximum
- GaSe - Gallium Selenide
- HAADF - High Angle Annular Dark Field
- hBN - Hexagonal Boron Nitride
- InSe - Indium Selenide
- IPA - Isopropyl Alcohol
- IrrRep - Irreducible Representation
- iX - Interlayer Exciton
- LT - Low Temperature

- LUT - Look-Up Table
- MoS_2 - Molybdenum Disulphide
- $MoSe_2$ - Molybdenum Diselenide
- PDMS - Polydimethylsiloxane
- PL - Photoluminescence
- PLE - Photoluminescence Excitation
- PMMA - Poly(methyl methacrylate)
- PPC - Poly(propylene carbonate)
- PTMC - Post-Transition Metal Chalcogenide
- PVA - Poly(vinyl alcohol)
- RC - Reflectance Contrast
- RT - Room Temperature
- SAED - Selected Area Electron Diffraction
- SEM - Scanning Electron Microscopy
- SHG - Second Harmonic Generation
- Si - Silicon
- SiO_2 - Silicon Dioxide
- STEM - Scanning Transmission Electron Microscopy
- STS - Scanning Tunnelling Spectroscopy
- TEM - Transmission Electron Microscopy
- TMDC - Group VI Transition Metal Dichalcogenide
- UHV - Ultra-High Vacuum
- VB - Valence Band
- VBM - Valence Band Maximum
- WS_2 - Tungsten Disulphide
- WSe_2 - Tungsten Diselenide
- X - Exciton

Abstract

The isolation and study of graphene has led to research into a large number of other atomically thin, two-dimensional (2D) materials. These materials have various fascinating properties that complement those in graphene; allowing for the building of designer van der Waals heterostructures. However, many of these 2D materials are unstable in ambient conditions, restricting their study.

In this work, methods to isolate and protect these materials in an inert argon environment are given; revealing novel insights into the optical properties of few-layer, air-sensitive 2D semiconducting materials and their heterostructures. Specifically, the lack of degradation due to encapsulation enable the observation of Raman spectra and second harmonic generation in monolayer InSe as well as Raman and photoluminescence spectra for few-layer GaSe crystals for the first time.

These isolated 2D semiconductors are then stacked adjacent to one another, forming heterojunctions with a type-II band alignment. These heterojunctions reveal new interlayer excitonic states with an energy that may be tuned by selecting the layer thicknesses. The recombination of these exciton states is suggested to be direct or quasi-direct in momentum-space, in contrast to previous attempts that demonstrated momentum-indirect interlayer excitonic states in 2D semiconductors. These momentum-direct interlayer excitons show bright luminescence and, as their energy is tunable, increase the spectral coverage available for van der Waals heterostructures.

Lastly, the high quality fabrication methods presented also enable the first observation of resonantly hybridised excitons between two closely aligned TMDC monolayers. The close crystallographic alignment promotes the hybridisation of interlayer and intralayer excitonic states, revealing new states that inherit the properties of each excitonic component.

Declaration

I declare that no portion of the work referred to in this thesis has been submitted in support of an application for another degree or qualification of this or any other university or other institute of learning.

Copyright Statement

The following four notes on copyright and the ownership of intellectual property rights must be included as written below:

1. The author of this thesis (including any appendices and/or schedules to this thesis) owns certain copyright or related rights in it (the "Copyright") and s/he has given The University of Manchester certain rights to use such Copyright, including for administrative purposes.

2. Copies of this thesis, either in full or in extracts and whether in hard or electronic copy, may be made only in accordance with the Copyright, Designs and Patents Act 1988 (as amended) and regulations issued under it or, where appropriate, in accordance with licensing agreements which the University has from time to time. This page must form part of any such copies made.

3. The ownership of certain Copyright, patents, designs, trademarks and other intellectual property (the "Intellectual Property") and any reproductions of copyright works in the thesis, for example graphs and tables ("Reproductions'), which may be described in this thesis, may not be owned by the author and may be owned by third parties. Such Intellectual Property and Reproductions cannot and must not be made available for use without the prior written permission of the owner(s) of the relevant Intellectual Property and/or Reproductions.

4. Further information on the conditions under which disclosure, publication and commercialisation of this thesis, the Copyright and any Intellectual Property and/or Reproductions described in it may take place is available in the University IP Policy (see http://documents.manchester.ac.uk/DocuInfo.aspx?DocID=24420), in any relevant Thesis restriction declarations deposited in the University Library, The University Library's regulations (see http://www.library.manchester.ac.uk/about/regulations/) and in The University's policy on Presentation of Theses.

Acknowledgements

Throughout these studies, many people have been incredibly helpful to inform and discuss various aspects of the research undertaken. A special thanks must be given to Roman Gorbachev for his attentive, patient and wise supervision. I would also like to give a massive thanks to Matthew Hamer for his friendly advice and guidance on fabrication as well as to Maciej Molas for happily sharing his expertise on optical measurements.

I must as well thank many others for their advice and instruction in the cleanroom, most notably James Howarth, Matthew Holwill, John Birkbeck, Lee Hague, Gregory Auton, Johanna Zultak, Anastasia Tyurnina and Thomas Bointon. I would also like to thank Endre Tóvári, Samuel Magorrian and Andrey Kretinin for their help in understanding various theoretical aspects of the research undertaken. Furthermore, I would also like to give a big thank you to James Howarth for the many constructive, thought-provoking and entertaining discussions.

I must thank all the staff at the National Graphene Institute for their continuous efforts to keep the building and cleanroom in good working order. Financial support for these studies was graciously given by the EPSRC Graphene NowNano Centre for Doctoral Training and Samsung Electronics Ltd.; of which I am incredibly grateful.

I'd like to thank my church family at Christ Church Manchester for their continued patience, kindness and grace toward me. I would also like to thank my wonderful family for their boundless love and support, without whom none of this would be possible. Moreover, my wife and partner in life, Falon, surely deserves a doctorate in patience. Lastly, to Jesus, with whom all is good and given purpose.

To Ayva Joy Terry, separated now but not for long.

Preface

This thesis is categorised into chapters, each is briefly described as follows.

In chapter 1, the lattice and electronic band structures of graphene and hexagonal boron nitride (hBN) are introduced. Following this, the usefulness of hBN as an encapsulating material in high quality heterostructures is discussed. Then, the band structure features of semiconducting group-VI transition metal dichalcogenides and post-transition metal chalcogenides are presented.

In chapter 2, the methods to isolate, identify and protect air-sensitive two-dimensional materials in hBN whilst in an argon glovebox are presented. The usefulness of this protection and annealing is demonstrated. Lastly, atomic force microscopy and further fabrication procedures are discussed, with an introduction to a novel ultra-high vacuum fabrication system currently under construction.

In chapter 3, the optical methods used to characterise two-dimensional materials are described. This includes a theoretical introduction to and practical implementation of photoluminescence, Raman, polarisation-resolved second harmonic generation and reflectance contrast measurements. Afterwards, the integration of these techniques into an ultra-high vacuum system is discussed.

In chapter 4, optical experiments performed on two post-transition metal chalcogenides in the few-layer regime are presented. Due to their exfoliation in argon and subsequent protection, various optical properties of monolayers and few-layers are observed for the first time.

In chapter 5 & 6, photoluminescence spectra observed for combinations of various air-sensitive semiconducting two-dimensional materials are given, revealing novel Γ point interlayer excitons and resonantly hybridised excitonic states.

In chapter 7, suggested work beyond this thesis that should be undertaken is addressed. Further exploration of the novel excitonic states is suggested alongside the continued investigation of fabrication under an ultra-high vacuum.

Chapter 1

Introduction to 2D Materials

Over the last half-century, the success of continued electronics development has been clear; with increased technological capabilities transforming a multitude of fields [1]. State-of-the-art electronic devices are fabricated from a variety of materials that have a three-dimensional crystal structure. These include semiconductors such as silicon and germanium and metals such as gold and silver - to name just a few. These materials have different electronic properties, allowing for various devices and applications. However, many more materials exist that may continue to add to the capabilities offered by state-of-the-art electronics. Amongst them, two-dimensional (2D) materials have recently presented compelling possibilities.

Briefly, as 2D materials may be exfoliated into atomically thin crystals (even to single layers), the possibility of fabricating electronic devices at the nanoscale limit is intrinsically promoted. Also, as many 2D crystals are available, each with different electronic properties (including metallic, semiconducting and insulating properties amongst others) there exists the building blocks necessary for the creation of new devices made entirely out of 2D materials [2]. The weak van der Waals attraction between adjacent 2D crystal layers allows for simple monolayer isolation via adhesive tape, for precisely controllable layer-by-layer creation of designer heterostructures (with atomically sharp interfaces) as well as for the control of the relative twist angle between adjacent layer lattices. Together, these features present 2D materials as exciting new tools for advancing current technologies.

In this chapter, the properties of various 2D materials are introduced. Initially, the lattice and electronic band structure of the archetypal 2D material,

graphene, is discussed. Following this, the importance of another 2D material, hexagonal boron nitride (hBN), in the design of heterostructure devices is presented. Afterwards, the semiconducting properties of two classes of 2D materials are described with particular emphasis given to their band structures.

1.1 Graphene

Graphene, a monolayer sheet of the layered material graphite, was first experimentally isolated and reported on in 2004 [3]. Since then, graphene has opened up new and exciting avenues of research in a variety of fields. The discovery of isolated graphene earned Professors Andre Geim and Konstantin Novoselov the 2010 Nobel prize in physics "for groundbreaking experiments regarding the two-dimensional material graphene" [4].

The structure of graphene consists of a plane of carbon atoms covalently bonded in a honeycomb lattice; see Fig 1.1. In graphite, such layers are bound by a relatively weak van der Waals attraction, allowing for the isolation of a monolayer by exfoliation [3]. The bonding arrangement in a monolayer of graphene results in an electronic configuration, known as sp^2 hybridisation, whereby each carbon atom is bonded to three other carbon atoms by strong in-plane σ bonds (giving it the greatest intrinsic strength of any material [6]) with the residual electrons forming out-of-plane π bonds, allowing charge transport to occur [7]. Indeed, the first experiments on few-layer graphene probed its electronic properties, with the electric field effect showing that mobilities of $\sim$10,000cm^{2}V^{-1}s^{-1} were achievable at room temperature [3]. This mobility was further enhanced to $\sim$200,000cm^{2}V^{-1}s^{-1} at electron densities of $\sim 2\times10^{11}$cm^{-2} for graphene suspended $\sim$150nm above a silicon/silicon oxide (Si/SiO_2) substrate gate electrode [8]; demonstrating its remarkable transport capabilities. The band structure of monolayer graphene is now well known and can be calculated appropriately with a tight-binding model of the out-of-plane π electrons [7]. In reciprocal space, the electronic band structure of graphene can be represented in what's known as a Brillouin zone (BZ) - the reciprocal space primitive cell. If the real space hexagonal lattice vectors of the graphene primitive cell are given by $\underline{a}_1, \underline{a}_2$ (see Fig. 1.1a), then the edges of the BZ are defined relative to the hexagonal reciprocal lattice vectors $\underline{b}_1, \underline{b}_2$ (such that $\underline{a}_i \cdot \underline{b}_j = 2\pi\delta_{ij}$). The inequivalent corners of the BZ are labelled K and K$'$ and their mid-point M; see Fig. 1.1b. For monolayer

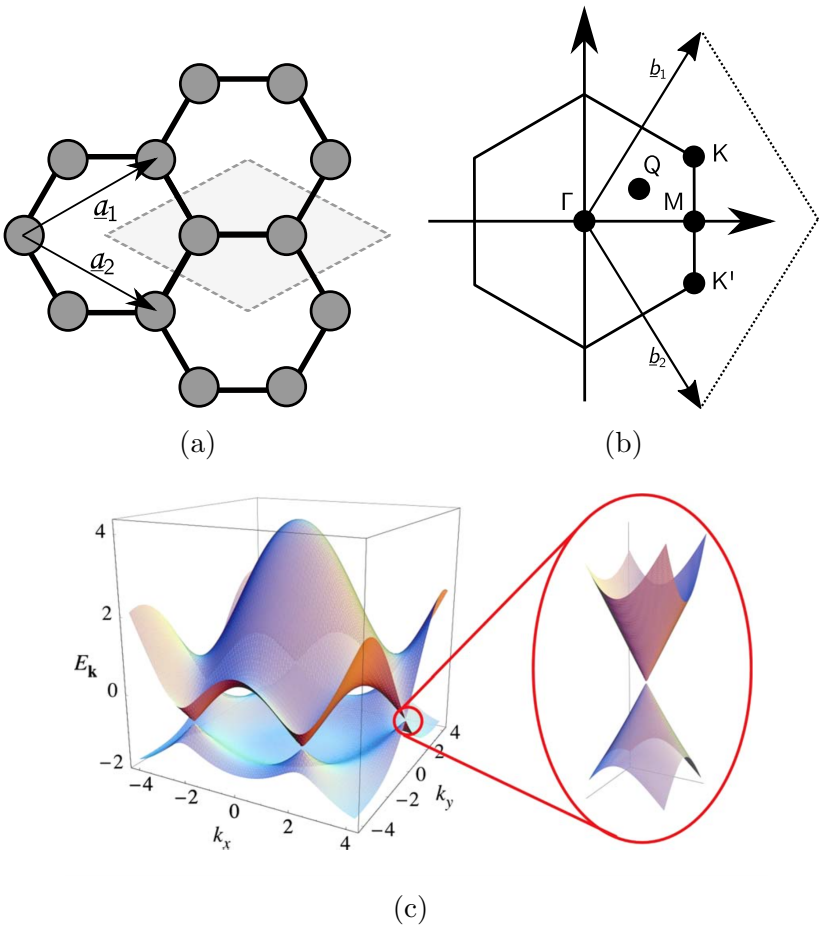

Figure 1.1: The graphene honeycomb lattice demonstrating the lattice vectors $\underline{a}_1$, $\underline{a}_2$ and the unit cell (shaded area) (a), BZ with Γ, Q, M, K, K′ points and the reciprocal lattice vectors $\underline{b}_1$ and $\underline{b}_2$ (b) and electronic band structure (c) of pristine monolayer graphene illustrating the Dirac points; taken from [5].

pristine graphene, the electronic band structure exhibits a cone shape at the BZ corners, where the valence and conduction bands meet. The Fermi level for the undoped case is located at the midpoint (see Fig. 1.1c), giving it semi-metallic properties. As the cones have a linear dispersion relation, the charge carriers behave as massless Dirac fermions. Indeed, for monolayer graphene, the anomalous integer quantum Hall effect was observed, suggesting it's band structure near the Fermi level to facilitate these massless Dirac fermions [9, 10]. Optically, monolayer graphene has been shown to absorb $\pi\alpha \sim 2.3\%$ of white light, another consequence of its unusual band structure [11].

The fascinating properties of graphene has led to the investigations of many

other 2D materials at their atomic limit with the hope that they too will demonstrate other interesting properties of various uses. The isolation of graphene is the beginning of the 2D materials story and motivation in itself for research into other 2D materials.

1.2 Hexagonal Boron Nitride

The exploration of graphene's electronic properties was initially performed on Si/SiO_2 substrate wafers [3]. Although these substrates are useful in providing a gating electrode/dielectric for electronic transport measurements, it was found that such substrates were limiting the maximum obtainable carrier mobility for graphene devices. This was suggested to be due to disorder in the graphene devices through induced charged impurity scattering [12–14] (such charge-impurities also create 'puddles' of charge variation at low concentrations, observable through a scanning single-electron transistor [15]), as well as through SiO_2 phonon scattering [14] and surface roughness [16]. It has been suggested that for these reasons an increase in the carrier mobility by an order of magnitude was observed for suspended graphene at $\sim$5K [8]. However, suspended graphene devices are limited in scope of design, are significantly more difficult to fabricate and at room temperature out-of-plane flexural phonons limit the carrier mobility [17]. A significant breakthrough was achieved by using hexagonal boron nitride (hBN) as a substrate for graphene devices, when Dean et al. found that higher carrier mobilities for non-suspended devices could be achieved [18]. It was suggested that this was due to a few characteristics of hBN, which are examined below.

Firstly, hBN has a similar crystal structure to graphene. It is a layered material of a mixture of covalently and ionically, in-plane, bonded boron and nitrogen atoms occupying the **a** and **b** sublattice sites of a honeycomb lattice respectively; see Fig. 1.2 [19]. As with graphene, the layers are held together by van der Waals forces which allows for the isolation of monolayers [20]. The crystal structure results in an atomically flat surface that mitigates the roughness of any underlying substrates, such as SiO_2 [18, 21]. As graphene has been shown to follow any underlying morphology, placing it on an atomically flat surface drastically reduces its corrugations [22]. In the case of a SiO_2 substrate, these corrugations have been suggested to reduce carrier mobility in graphene by facilitating scattering on flexural, out-of-plane, phonons [16].

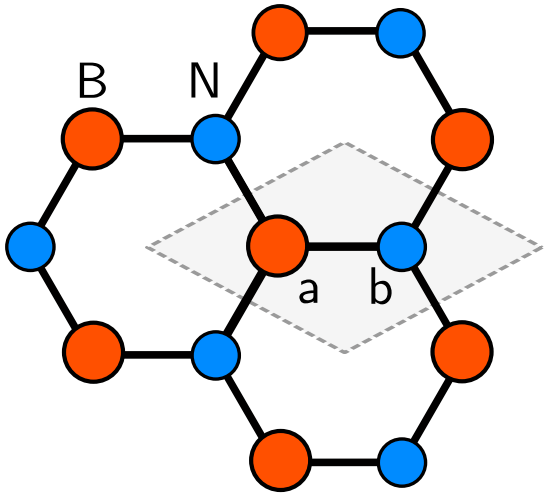

Figure 1.2: The hexagonal boron nitride honeycomb lattice demonstrating the boron and nitrogen atoms at sublattice sites **a** and **b**, respectively, in the unit cell (shaded area)

Secondly, hBN is often used as a refractory material due to its high chemical and thermal stability [23]. The chemical stability is also suggested to reduce the likelihood of charged impurities occurring when compared with SiO_2, reducing scattering in graphene [18]. Indeed, hBN has been shown to have a high uniformity, with no defects or pinholes observable over scales of tens of square microns [24].

Thirdly, hBN may function as a high quality gate dielectric for field-effect devices. Its dielectric constant (or relative permittivity) ϵ is typically quoted as being between 3-4 [25, 26], similar to that of SiO_2 ($\epsilon = 3.9$) [27]. hBN has been shown to have a high breakdown field ($\sim$1Vnm^{-1}), also similar to that of SiO_2 [26]. The insulating behaviour that hBN exhibits is due to its large band gap of $\sim$6eV [28]. This band gap forms because (unlike graphene) the sublattices are inequivalent, breaking inversion symmetry [7]. As a bulk crystal, phonon-assisted luminescence was observed for hBN, suggesting it to have an indirect band gap (the meaning of this is discussed in the following section) [29, 30].

Lastly, hBN was used not only as a substrate dielectric, but also as an encapsulating material for graphene devices [31]. This led to another improvement in device quality, with micrometre length scale ballistic transport observed at room temperature [31]. This improvement is suggested to be due to the reduced effect of contamination from ambient air and fabrication procedures that require the use of polymers and solvents. Alongside improvements in graphene-metal contacting,

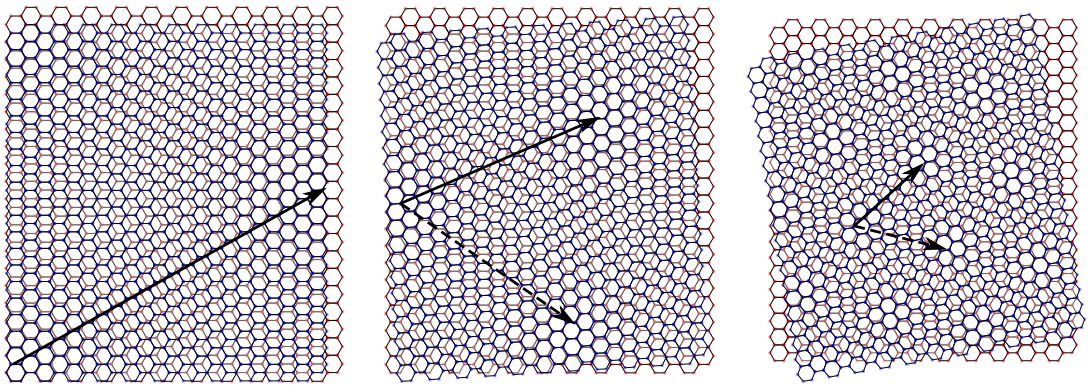

(a) 0° (b) 3.5° (c) 9.4°

Figure 1.3: Schematic of the moiré superlattice structure of graphene (blue lattice) on hBN (red lattice) at specified angles with arrows demonstrating the superlattice vectors. The lattice mismatch is amplified to be 5%.

these encapsulated graphene devices demonstrated mobilities close to the theoretical limit at room temperature and were experimentally limited by the device size at cryogenic temperatures [32]. Other materials, such as muscovite mica and bismuth strontium calcium copper oxide, were tested as encapsulators of graphene for high quality electronic devices. However, none were found to give as high a quality as hBN. This was suggested to be due to the self-cleansing process between hBN and graphene [33]. In this process, contamination at the hBN-graphene interface is squeezed together into agglomerations by van der Waals forces, leaving large clean areas which can be utilised for electronic measurements. This process will be discussed in Ch. 2.

The usefulness of hBN as an encapsulating material does not stop with graphene. It has also been used on a variety of other 2D materials in order to improve their properties. For materials that decompose in ambient air, such as black phosphorus and niobium diselenide, hBN was found to protect the composition sufficiently to allow for high quality electronic measurements to be obtained [34]. For materials displaying photoluminescence, emission line-widths have been found to be significantly reduced as well as being more stable after laser exposure and multiple cooling cycles [35]. This is suggested to be due to surface protection from adsorbents as well as providing a flatter substrate, reducing inhomogeneous broadening of line-widths [35]. Also, as hBN has a relatively large band gap, its affect on luminescent processes in the visible to near-infrared wavelength range is suggested to be negligible, allowing optical probing of the intrinsic properties

of the encapsulated material. For these reasons, in this thesis hBN is used as an encapsulating material throughout device fabrication in order to improve device quality. The bulk hBN used here (provided by the National Institute for Materials Science in Japan [36]) has the highest quality of the known sources [37].

As graphene and hBN have similar crystal lattices with a small mismatch of $\sim$1.8% [38], an effective moiré superlattice structure may form when they are brought together [39]. The resulting superlattice has a period that depends upon the twist angle between the two materials: as this angle increases up to 30°, the period of the superlattice becomes smaller; see Fig. 1.3. At small angles (<1°), the graphene lattice can stretch locally to minimise its energy in the potential of the underlying hBN, forming periodic commensurate domains separated by narrow highly strained regions [39].

The long range moiré periodicity between aligned graphene and hBN has been shown to cause strong reconstruction of the electronic spectrum in graphene, revealing cloned Dirac fermions [40]. In a magnetic field, this superlattice arrangement has also displayed an intriguing energy fractal spectrum known as Hofstadter's butterfly [40, 41]. These induced spectral features have opened a novel way of controlling properties of 2D materials through their relative twist, conceiving a new field known as "twistronics". This will be discussed further in Ch. 5.

1.3 Group VI Transition Metal Dichalcogenides (TMDCs)

1.3.1 Introduction

Group VI transition metal dichalcogenides (TMDCs) form a class of 2D materials that have received a lot of attention in recent years due to their interesting properties that complement those already demonstrated by graphene and hBN. The crystal structure of TMDCs consists of a group VI transition metal atom M (molybdenum or tungsten) bonded to chalcogen atoms X (here sulphur or selenium) in a trigonal prismatic lattice, having an empirical chemical formula of MX_2 [42]; see Fig. 1.4. A monolayer therefore consists of M atoms sandwiched between two planes of X atoms, with adjacent layers bonded by weak van der Waals forces; allowing for the isolation of monolayers $\sim$7Å thick [42, 43].

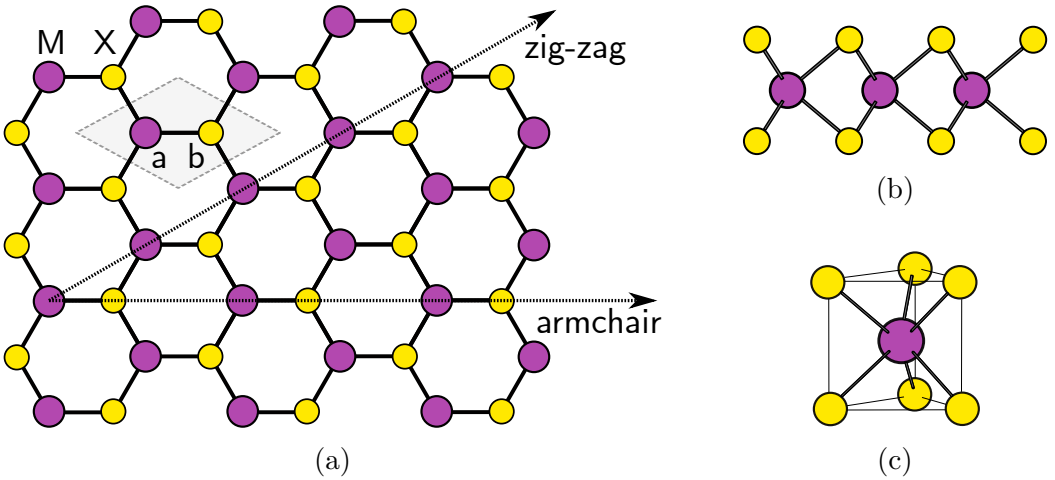

Figure 1.4: The MX_2 lattice demonstrating (a) the metal M (purple) and chalcogen X (yellow) atoms at sublattice sites **a** and **b**, respectively, in the unit cell (shaded area), along with the armchair and zig-zag axes (b) the side-view of the MX_2 crystal structure and (c) and the trigonal prismatic bonding geometry of the crystal.

In their multi-layer form, group VI TMDCs are semiconductors with indirect band gaps in the near infrared wavelength range [44]. A band gap is considered indirect if the valence band maximum (VBM) and conduction band minimum (CBM) are located at different points in the BZ momentum space; requiring an electron to undergo a momentum change when it relaxes to the valence band (VB) and emits a photon. Such a momentum change can occur through the absorption or emission of a lattice vibration quasiparticle known as a phonon. A direct band gap has its VBM and CBM at the same locations in the BZ momentum space. Thus, an electron at this location in the conduction band (CB) can directly emit a photon, not requiring a momentum shift. As monolayers, TMDCs become direct band gap semiconductors demonstrating strong absorption ($\sim$20% per monolayer) near the exciton resonances and two orders of magnitude increase in luminescence quantum efficiency [45, 46]. This direct band gap, alongside other features to be discussed in the following subsection, opens up the exciting possibility of using semiconductors to design novel atomically thin optoelectronic devices combined with the semi-metallic graphene and insulating hBN. As semiconductors, TMDCs offer routes toward better integration between optics and electronics as well as the possibility for better transistors with higher on/off ratios [47–49]. Indeed, devices such as light emitting diodes [50] and photodetectors [51] have been fabricated and measured, showing promising results.

State	Major Orbitals	Minor Orbitals
K_v	M-$d_{x^2-y^2}$,d_{xy}	X-p_x,p_y
K_c	M-d_{z^2}	X-p_x,p_y
Γ_v	M-d_{z^2}	X-p_z
Q_c	M-$d_{x^2-y^2}$,d_{xy}	M-d_{z^2}, X-p_x,p_y,p_z

Table 1.1: Major and minor orbital contributions to the Bloch states at certain points in the BZ for monolayer MX_2 [53].

1.3.2 Band structure

Fundamental to the interesting properties of group VI TMDCs are their electronic band structures. As the atomic configuration for the components of each MX_2 material are similar, the electronic band structures are found to also be similar with only minor differences. The group VI transition metal atoms (molybdenum and tungsten) have electronic configurations with six valence electrons constituting five d-orbitals [52]. The chalcogenide atoms (sulphur and selenium) have electronic configurations with six valence electrons constituting four p-orbitals [52]. Thus, it has been found through first principle calculations that these d- and p-orbitals dominate the band structure of MX_2 [52, 53]. As the crystal structure of MX_2 is hexagonal, the first BZ is also hexagonal; see Fig. 1.1b. In the first BZ of monolayer MX_2, the VBM and CBM (labelled as K_v and K_c respectively) have both been shown to occur at the K and K′ points (the inequivalent edges of the BZ), giving these materials a direct band gap [52, 53]. Secondary conduction band valleys exist halfway between the edges (K or K′) and centre (Γ) of the BZ at locations denoted as Q (labelled as Q_c here); see Fig. 1.5. Also, a secondary valence band maximum occurs at the Γ point, labelled Γ_v in Fig. 1.5.

The d- and p-orbitals that contribute to the Bloch states at these different points in the BZ are demonstrated for monolayer MoS_2 (representative of the TMDCs) in Fig. 1.5. At the K points (K_v and K_c), the Bloch states are mostly composed of metal atom d-orbitals with a minority contribution coming from chalcogenide atom in-plane p-orbitals. At Q_c and Γ_v, the Bloch states are also mostly composed of metal atom d-orbitals but, crucially, contain a contribution from the chalcogenide atom out-of-plane p-orbitals [52–55]; see Table 1.1. As such, the Q_c and Γ_v points are affected by adjacent layers more so than the K_v and K_c points, with the hopping strength increasing when adjacent X-p_z orbitals are brought close. This has the effect of increasing (decreasing) the energy at the

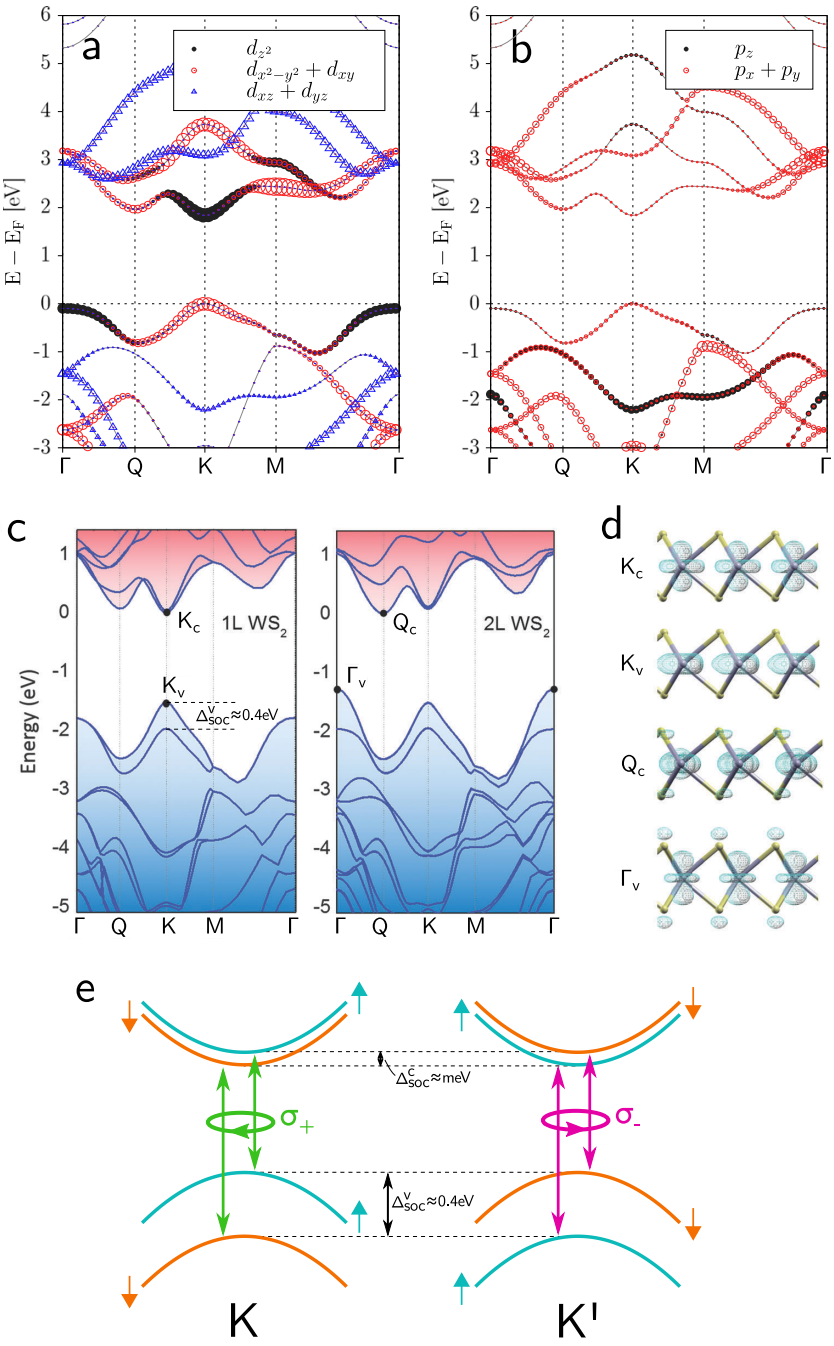

Figure 1.5: Electronic band structures of monolayer MoS_2 with the weights (spin-orbit coupling neglected) of (a) the metal d-orbitals and (b) the chalcogen p-orbitals, of (c) monolayer and bilayer WS_2 demonstrating the band gap position change from K_v/K_c to Q_c/Γ_v and (d) the representative isosurface plots for the states at these positions. (e) Schematic of the spin-valley coupled states at K and K′ for monolayer WX_2 showing the spin-splitting in the conduction and valence bands. Adapted from [54–56].

Γ_v (Q_c) point enough so that for bilayer and thicker MX_2, the band gap decreases and becomes indirect from Γ_v to Q_c [53, 56, 57].

Experimental determination of the electronic band gaps for the different monolayer MX_2 crystals have been attempted using various methods without conclusive agreement. This is due to differences between the techniques employed, each with their own pitfalls [57]. Table 1.2 summarises the monolayer and bulk electronic band gaps obtained so far.

MX_2	Monolayer Band Gap (eV) [57]	Bulk Band Gap (eV) [58]
WS_2	2.3-3.0	1.35
WSe_2	1.9-2.6	1.20
MoS_2	2.1-2.5	1.23
$MoSe_2$	2.1-2.2	1.09

Table 1.2: Comparison of monolayer and bulk MX_2 electronic band gaps. Values taken from [57, 58].

In its monolayer form MX_2 also lacks inversion symmetry, enabling more interesting physical phenomena to occur. A crystal has inversion symmetry, or centrosymmetry, if points $\underline{r}$ in the unit cell are indistinguishable from those at $-\underline{r}$. For TMDCs, it has been shown that because of the broken inversion symmetry and a strong spin-orbit interaction, spin-valley coupling is allowed, a phenomenon whereby carrier spin may be localised to certain locations, or valleys, of the BZ (K and K′); something not usually observed in conventional semiconductors [53, 57, 59]. This phenomenon is explained as follows.

As the crystal structure has mirror reflection symmetry about its metal atom plane, the Bloch states before and after such a reflection must have equivalent energy. As spin is an axial vector, its direction flips after reflection in a plane that it is parallel to. However, when the spin is perpendicular to the plane of reflection, its direction remains the same. It is helpful to consider a similar axial vector angular momentum ($\underline{L} = \underline{r} \times \underline{p}$) under reflection in a plane that it is parallel to. In this case, mirror reflection results in either $\underline{r} \to -\underline{r}$ or $\underline{p} \to -\underline{p}$ and thus $\underline{L} \to -\underline{L}$. As the energy states in the case of a spin flip (for in-plane directed spin) would be identical due to symmetry, there can be no spin-splitting of the energy for these directions. However, for out-of-plane spin, as there is no spin flip from symmetry, the energy states for $+z$ or $-z$ spin vectors do not have to be identical, allowing for a possible splitting of the energy states for opposite spins ($\pm z$) [53, 60]. Also, due to time reversal symmetry, which

states that the momentum and spin switch signs ($\underline{k} \rightarrow -\underline{k}$ and $\underline{s} \rightarrow -\underline{s}$), the spin splitting of the energy states must be opposite at the opposite sides of the BZ, i.e. $E_{\uparrow}(\underline{k}) = E_{\downarrow}(-\underline{k})$ and $E_{\downarrow}(\underline{k}) = E_{\uparrow}(-\underline{k})$ [53, 60–63]. This symmetry requirement then couples the spin states to BZ locations, here the K, K′ positions or valleys. Interestingly, if inversion symmetry in the monolayer was not broken (such that $\underline{k} \rightarrow -\underline{k}$ and $\underline{s} \rightarrow \underline{s}$), no spin splitting would occur at either side of the BZ, disallowing spin-valley coupling [64]. It is this reason why the broken inversion symmetry in MX_2 is deemed crucial for the spin-valley coupling phenomenon [53, 61–63].

As shown in Table 1.1, at the K points (K_v and K_c), the Bloch states are mostly composed of metal atom d-orbitals with a minority contribution coming from chalcogenide atom in-plane p-orbitals. At the valence band position K_v, the majority contribution is composed of $d_{x^2-y^2}$ and d_{xy} orbitals with an orbital quantum number $l = 2$ and a magnetic quantum number m_l dependent on its valley index $\tau = \pm 1$ such that $m_l = 2\tau$ [65]. A spin-orbit interaction may then occur for an out-of-plane spin s_z, altering the band energy by the spin-orbit coupling term $m_l s_z$; following the valley dependence. As TMDCs consist of heavy metallic atoms, this spin-orbit interaction is strong. For the conduction band, K_c has a majority composition of d_{z^2} orbitals with $l = 2$ and $m_l = 0$, giving no spin-orbit energy interaction [65]. More carefully however, other orbitals give small contributions to the spin-orbit coupling at K_c. The minor p_x and p_y orbitals with $m_l = \tau$ and surrounding d_{xy} and d_{yz} orbitals also with $m_l = \tau$ compete to contribute a small spin-orbit energy interaction [53, 54, 66]. This competition has been found to result in MoX_2 and WX_2 having opposite spin splitting in the conduction band. Due to the difference in orbital contributions to the spin-orbit coupling, the valence band at K has a greater spin splitting, typically ∼0.2eV for MoX_2 and ∼0.4eV for WX_2 compared to a few meV in the conduction band for all MX_2 materials [54, 57].

Another interesting feature resulting from the lack of inversion symmetry in MX_2 is that of valley-selective circular dichroism whereby the optical selection rules dictate that the interband transitions at the K and K′ valleys must occur through circularly polarised light [67]. This can be formulated by considering the interband transition matrix elements $\langle \psi_f | \hat{P}_{\pm} | \psi_i \rangle$ for circularly polarised light $\sigma_{\pm}$ (obtained through the electric dipole approximation [68–70] with its square value describing the oscillator strength for interband transitions). $\hat{P}_{\pm} = \hat{P}_x \pm i\hat{P}_y$

describes the momentum operator and $\psi_{i,f}$ the initial and final Bloch states. By considering the rotational symmetry of the Bloch states for the orbitals contributing to the conduction and valence bands, it can be shown that a non-zero interband transition at K and K′ must occur through σ_+ and σ_- polarised light, respectively [53, 71]; see Fig. 1.5. If inversion symmetry was maintained in this system, at the K and K′ points the circularly polarised light would be identical, disallowing this selection rule. However, because of the broken inversion symmetry, the chirality of circularly polarised light may select a valley and a spin due to the spin-valley coupling. This is in contrast to conventional semiconductors which may have spin polarisation induced in their carriers through circularly polarised light, but not spin and valley [57, 72].

1.4 Post-Transition Metal Chalcogenides (PTMCs)

1.4.1 Introduction

Post-transition metal chalcogenides (PTMCs) are another, less thoroughly studied, class of 2D materials that have received an increasing amount of attention in recent years. This is due to their possession of different semiconducting properties that complement those found for TMDCs. The crystal structure of the PTMCs considered here is composed of two post-transition metal atoms M (here gallium or indium are focussed on) predominantly covalently bonded to one another and each to three adjacent chalcogen atoms X (here only selenium is considered) such that a sequence of atomic planes X-M-M-X is formed; see Fig. 1.6 [73–75]. This sequence is sometimes referred to as a tetralayer due to the four quasi-layers [76]. The empirical chemical formula is given as MX here (although it is sometimes referred to as M_2X_2 in the literature [77]). From a top-down view, the crystal structure displays a honeycomb lattice geometry. The interlayer separation has been shown to have a thickness of ∼8Å [78–80].

As with the previously discussed 2D materials, layers of PTMCs are bound by weak van der Waals forces which allow for the isolation of atomically thin monolayers [75, 81, 82]. Layered stacks of PTMCs can be arranged in different orders, known as polytypes, which are shown in Fig. 1.7. The most commonly reported polytypes of crystals of GaSe and InSe to be studied are the ϵ- and γ-types, respectively [75, 83].

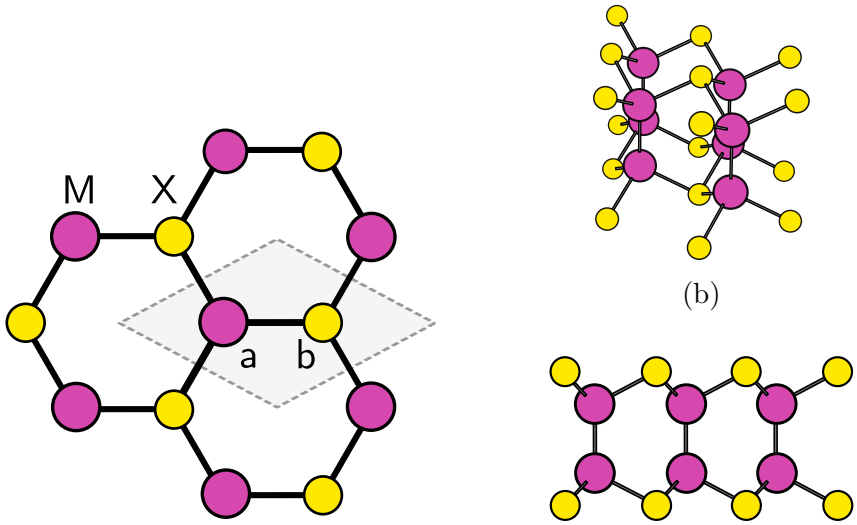

Figure 1.6: The PTMC crystal lattice structure demonstrating (a) the metal M (pink) and chalcogen X (yellow) atoms at sublattice sites **a** and **b**, respectively, in the unit cell (shaded area), (b) the bonding geometry of the crystal and (c) the side-view of the MX crystal structure.

Historically, these PTMC materials were studied in their bulk form due to their promising optical and optoelectronic properties [80, 83, 85, 86]. More recently, however, studies of their few-layer forms have emerged due to the capability to isolate them with the advent of the isolation of graphene. For both PTMC crystals, theoretical and experimental studies have suggested that the band gap increases as the thickness decreases [76, 82, 87, 88]. This is similar to that of TMDCs but with a key difference being that the gap remains "quasi-direct" around the Γ point in the BZ [76, 88]. The band structure will be discussed in more detail in the following subsection. The non-linear optical performance in both PTMC crystals has also been shown to be strong [89–91]. The conversion of light in the mid- to far-infrared range was initially one of the most promising properties for bulk GaSe [83, 92, 93]. Recently, the Hall mobility of six layer γ-InSe was measured to be 12,700cm^{2}V^{-1}s^{-1} and 1,000cm^{2}V^{-1}s^{-1} at 4K and room temperature, respectively, rivalling those found for other 2D semiconductors [94].

1.4.2 Band structure

As with TMDCs, the interesting properties of PTMCs can be appreciated with an understanding of their band structures. The group XIII post-transition

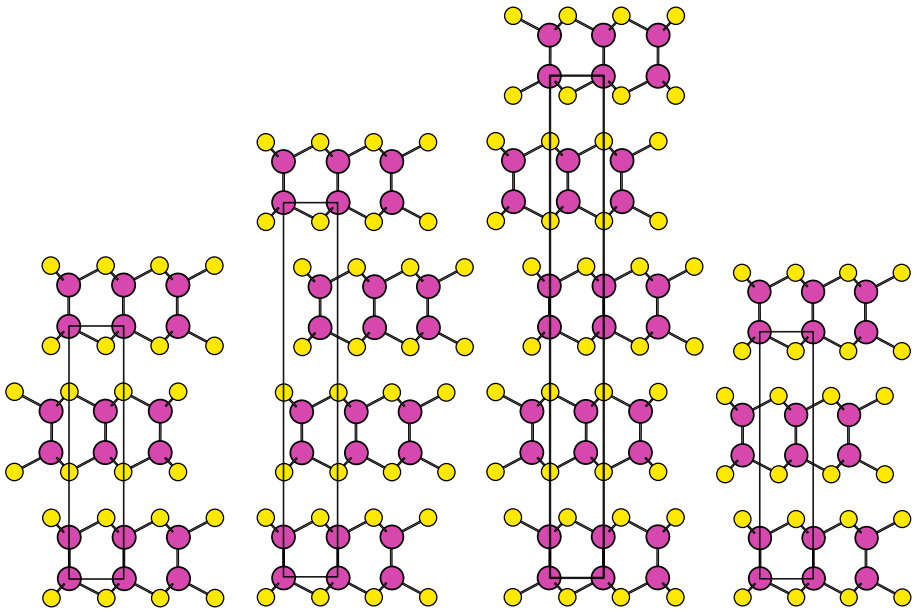

(a) β (b) γ (c) δ (d) ϵ

Figure 1.7: The various polytype configurations viewed from side-on for PTMCs with metal atoms shown as pink and chalcogen atoms as yellow. The unit cell is also given by the rectangle. [75, 84]

metals have electronic configurations with three valence electrons composed of two s-orbitals and one p-orbital [73]. The chalcogenide atoms, as described earlier, have six valence electrons with four p-orbitals [52].

As the electronic configuration for the components of each PTMC are similar, the band structures are also similar and can be summarised as one with only minor differences between the different materials. Naturally, these s- and p-orbitals dominate the band structure of PTMCs [76, 77, 95]. From first principle calculations, it has been shown that the VBM occurs close to the Γ point whilst the CBM occurs at the Γ point for monolayers [77, 95]. This makes monolayer PTMCs indirect semiconductors, in contrast to TMDCs. However, as the energy in the valence band at Γ is close to the energy at the VBM, the gap can be considered "quasi-direct" [96]. In fact, as the number of layers of MX increases, the VBM moves closer to the Γ point, giving a less indirect band gap arrangement; see Fig. 1.8 for the evolution of the band structures of GaSe and InSe as the number of layers is increased. These band structures were calculated from a tight-binding model fitted to scissor-corrected density functional theory (DFT) [88]. This scissor-correction aims to rectify a limitation of DFT whereby predictions

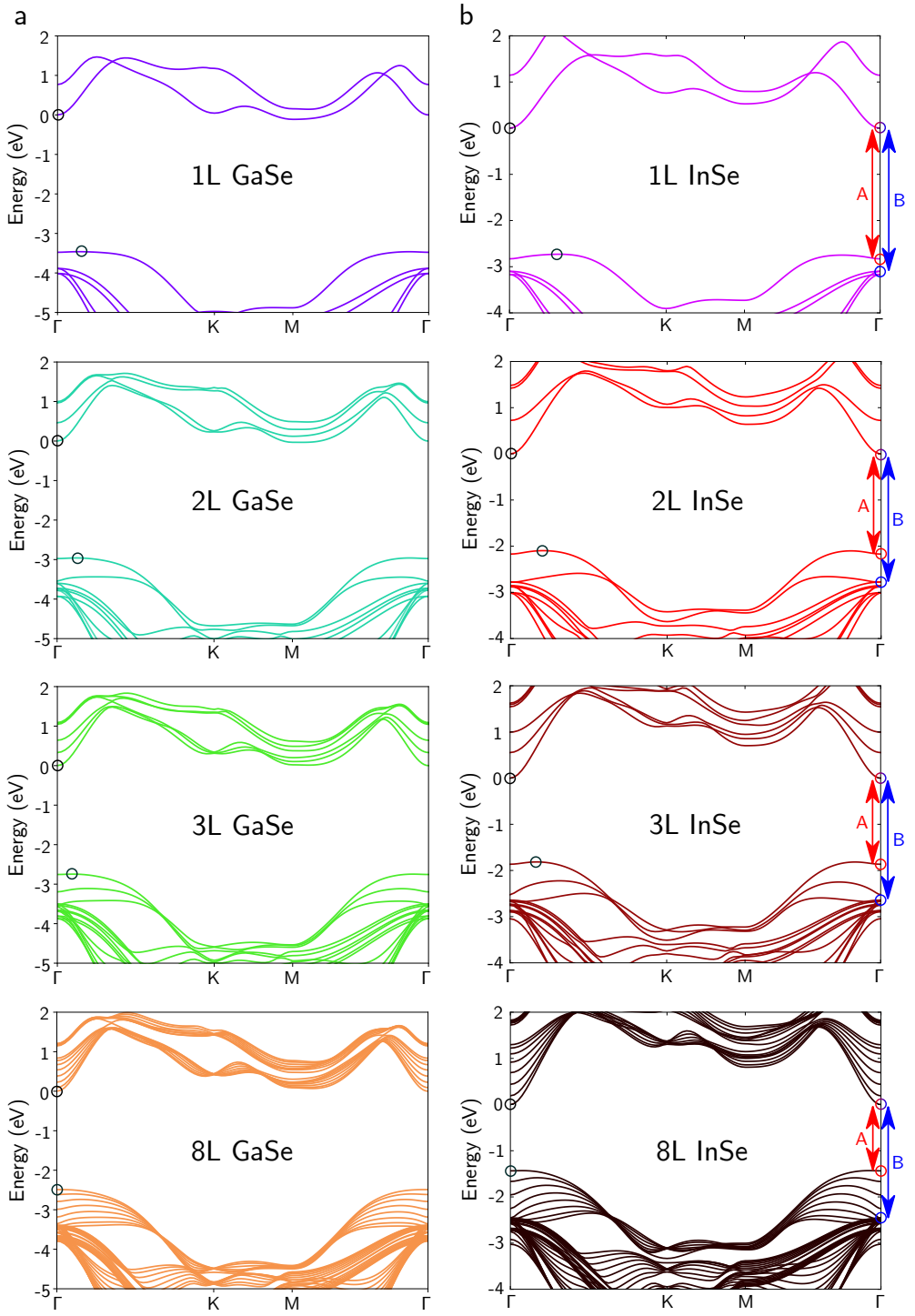

Figure 1.8: Band structures of few-layer (a) GaSe and (b) InSe calculated from a tight-binding model fitted to scissor-corrected DFT (see [88]), coloured according to their optical band gap wavelength. The black circles indicate the CBM and VBM whilst the red and blue circles indicate the A and B transition band points.

of semiconductor band gap values may be significantly underestimated [97]. The scissor-correction matches the bulk theoretical band gap to the experimentally known value; effectively shifting the band gap values for all thicknesses [98].

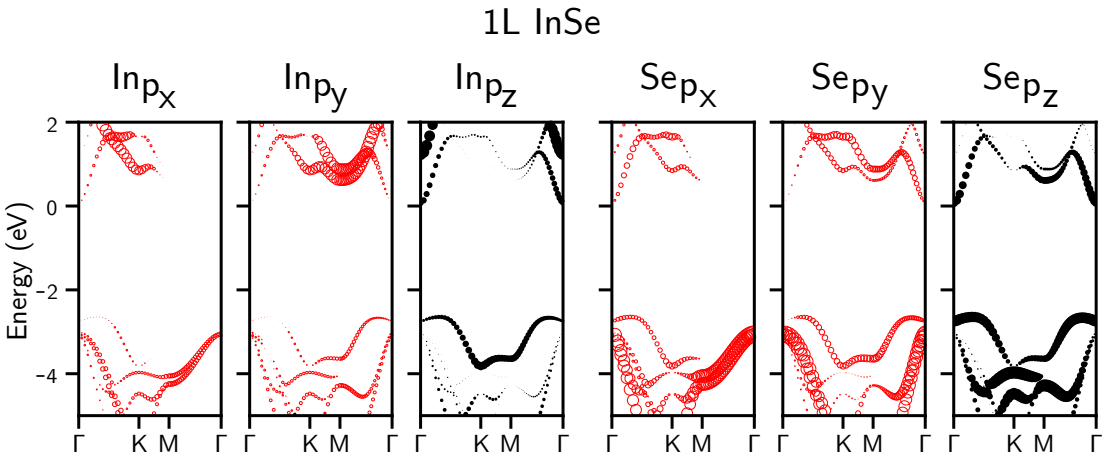

Figure 1.9: Orbital decomposition of the electronic bands for monolayer InSe by the p-orbitals of the indium and selenium atoms, calculated from a tight-binding model fitted to scissor-corrected DFT, adapted from [88]. Marker size indicates the normalised contribution.

As with TMDCs, considering the orbital contributions to the different parts of the band structure aids with understanding the changes in the band structure with the layer number. For PTMCs, the p_z orbitals on the outer X atoms strongly contribute to the bands near the VBM and CBM at the Γ point [88, 95, 99]. In contrast, near the BZ corners (K and K′ points) the X-p_z orbitals contribute much less [88, 95]; see Fig. 1.9. Thus, when adjacent MX layers are brought close, the bands at Γ are affected more so than those at the corners of the BZ as the hopping strength between adjacent X-p_z orbitals increases. As a result, the energies of the VBM and CBM change stronger at the Γ point than at the BZ corners, reducing the band gap and making it more direct [88]. The band gap in GaSe is expected to be larger than InSe due to the shorter M-M bond length which increases the coupling and therefore the band gap [77, 86, 95]

Attempts to understand the band structures of GaSe and InSe began over 50 years ago, with initial experimental evidence suggesting an indirect and direct gap to exist in close proximity to one another [80, 82, 86, 101–103]. At present, the bulk gap is generally accepted to be of a direct nature for both materials due to the VBM being found to occur at the Γ point in angle-resolved photoemission spectroscopy experiments (ARPES) [100, 104–108]. For the monolayer

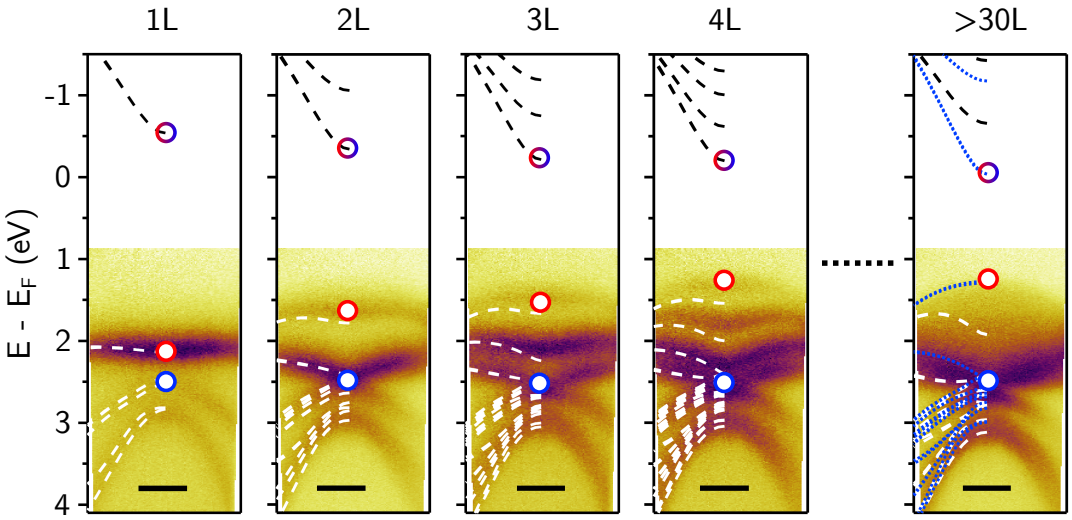

Figure 1.10: Valence band dispersion around the Γ point for various thicknesses of InSe measured with angle-resolved photoemission spectroscopy, as published in [100]. White (black) dashed lines indicate the DFT calculations for the valence (conduction) band. For bulk InSe, blue dashed lines indicate the DFT band calculations for out-of-plane wavevector $k_z = 0.5$. Red and blue circles indicate the A and B transition band edge points. Scale bars 0.2Å^{-1}.

and few-layer arrangements, the two gaps are suggested to be in close proximity with the lower of the two being indirect up to a certain number of layers; both in theoretical calculations [76, 77, 95, 103] and experiments [100, 109, 110]. Figure 1.10 demonstrates the valence band dispersion around the Γ point for encapsulated few-layer InSe crystals obtained from ARPES measurements during these studies. As is observable, the band gap become more direct as the InSe layer thickness increases.

Unlike the more researched TMDCs, experiments to gauge the electronic (single-particle) band gaps of GaSe and InSe are rare and usually restricted to optical measurements which are prone to assess the energetically distinct optical band gap. The optical and electronic band gaps are separated by exciton binding energies which can be large for 2D materials [57]. The difference between these band gaps is discussed in Ch. 3. The band gap of bulk GaSe has primarily been studied through optical experiments thus far with absorption spectroscopy suggesting a band gap of ∼2eV occurs at room temperature [111, 112]. Scanning tunnelling spectroscopy (STS) was recently used to show a significant widening of the electronic band gap from trilayer (∼2.3eV) to monolayer (∼3.5eV) for a molecular beam epitaxy grown GaSe/graphene heterostructure encapsulated in

selenium [109]. Although STS may probe the electronic band gap value, its precision is limited by the difficulty in accurately determining the onset of tunnelling currents as well as it being shown to be strongly influenced by the conducting substrate used in the measurement [57]. The band gap of bulk InSe has also so far mostly been studied through optical experiments with absorption spectroscopy suggesting a band gap of ∼1.2eV occurs at room temperature [86, 101]. More recently, STS on bulk InSe at 4K revealed an electronic band gap of 1.25eV [104]. At the point of writing, studies on the electronic band gap of few-layer InSe are absent from the literature. The values for the band gaps of few-layer and bulk GaSe and InSe are summarised in Table 1.3.

MX	Monolayer (eV)	Bilayer (eV)	Trilayer (eV)	Bulk (eV)
GaSe	3.3-3.5 [109, 113]	3.0 [109]	2.3 [109]	2.0 [111, 112]
InSe	2.8 [94]	1.85 [94]	1.65 [94]	1.20-1.26 [86, 101, 104]

Table 1.3: Comparison of monolayer, bilayer, trilayer and bulk GaSe and InSe band gaps. Values taken from [86, 94, 101, 104, 109, 111–113].

As the metal atoms in PTMCs are lighter than those in TMDCs, the spin-orbit couplings are expected to be weaker. Also, as the band edges are located at the Γ point, time-reversal symmetry dictates that the bands at Γ are spin-degenerate, unlike those at the K and K′ points for TMDCs [110]. The spin-orbit interaction does, however, have an impact on the optical selection rules. As described earlier, the band edges for PTMCs have a major contribution from X-p_z orbitals. These orbitals couple strongly to out-of-plane polarised photons but not to in-plane photons [114]. Without a spin-orbit interaction, it has been shown that the lowest energy transition (labelled as the A transition in Fig. 1.8) would be forbidden for in-plane polarised photons. However, with a spin-orbit interaction the A transition is allowed for in-plane polarised light. Interestingly, the next lowest VBM at Γ has a major contribution from X-p_x, p_y orbitals which couple strongly to in-plane polarised light [110, 114]. For this reason, a second, higher energy transition (labelled as the B transition in Fig. 1.8) is observable in out-of-plane incident optical studies, demonstrated in Ch. 4.

1.5 Summary

The variety of material properties available even within the small group of 2D materials discussed in this chapter is broad, allowing for a multitude of avenues of study and application. This chapter briefly introduced the first 2D material to be isolated, graphene, and its interesting electronic properties. The insulating 2D material, hBN, was then introduced with its usefulness in device quality discussed through its use as an encapsulating material as well as for the formation of moiré superlattices. Afterward, semiconducting TMDCs were introduced with their band structure at the corners of the BZ allowing for a spin-valley coupling that can be exploited through circularly polarised light. Finally, another set of semiconducting 2D materials, PTMCs, were introduced alongside their interesting quasi-direct band gaps at all layer thicknesses. The stacking of these atomically thin semi-metallic, insulating and semiconducting materials into van der Waals heterostructures is discussed in the following chapter.

Chapter 2

Fabrication of van der Waals Heterostructures

The advent of isolating atomically thin graphene layers, which were previously inaccessible, opened up a new avenue of nanofabrication techniques. Perhaps surprisingly, this new field relied upon simple adhesive tape. Perhaps more surprisingly, after more than a decade of research, it still relies upon the use of adhesive tape for the building of high quality devices. This simple feature of the fabrication process is also a powerful one, as it allows for complex combinations of various 2D materials to be formed relatively easily and inexpensively.

In this chapter, the fabrication processes for combining 2D materials into van der Waals heterostructures are detailed. Initially, the methods for the isolation and identification of atomically thin 2D crystals through mechanical exfoliation and optical microscopy, respectively, are discussed. Afterward, the different techniques available for transferring these thin 2D crystals onto one another are given and compared. Following this, the problems of air-sensitive 2D materials are discussed and the methods for handling such materials through the use of a glovebox are given. Then, the importance of annealing and atomic force microscopy for fabrication methods are discussed as well as fabrication procedures that may be required for further heterostructure design. Finally, the methods and exciting possibilities for heterostructure fabrication in an ultra-high vacuum environment are introduced.

2.1 Source Crystals

In order to isolate high quality 2D materials, the highest quality bulk source crystals must first be identified. Figure 2.1 shows five examples of source crystals, which have a typical width of 1cm.

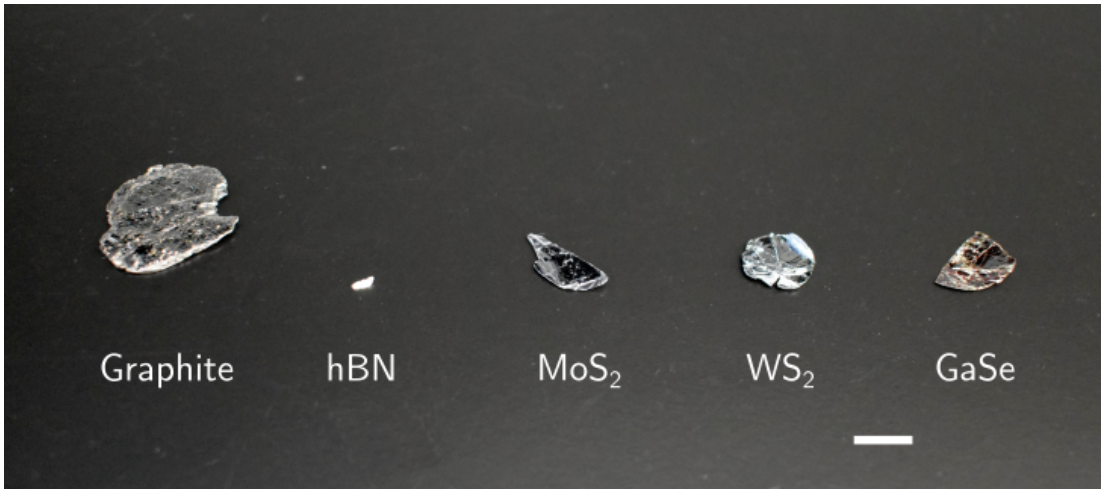

Figure 2.1: Typical bulk source crystals of graphite, hBN, MoS_2, WS_2 and GaSe used for 2D material isolation. Scale bar 1cm.

Over the years, many crystals with various origins have been made available. Some are artificially grown, whilst some are found to be naturally occurring. Here, large naturally occurring graphite crystals are used for their high quality (sourced from NGS Naturgraphit). As stated previously, hBN from the National Institute for Materials Science is used throughout as it has the highest quality of the known sources. These world-renowned hBN crystals are prepared through the use of a hydraulic press which holds a mixture of barium boron nitride ($Ba_3B_2N_4$) solvent and deoxidised hBN at 4.0-5.5GPa and 1500-1750°C under a nitrogen atmosphere for between 20-80 hours [36, 115]. Bulk crystals of TMDCs are sourced from HQ-Graphene, which are synthetically produced. Bulk crystals of InSe were grown by the Bridgman method from a polycrystalline melt of $In_{1.03}Se_{0.97}$, with material purity of indium >99.999% and selenium >99.999%. These crystals were grown and provided by the Institute for Problems of Materials Science, Ukraine. Bulk crystals of GaSe were grown by a modified Bridgman method that used heat field rotation, with source material purity of gallium >99.9997% and selenium >99.99% [116–118]. These crystals were grown and provided by the National Tomsk State Research University, Russia.

2.2 2D Material Exfoliation

With a source crystal selected, thin films may be isolated through exfoliation techniques. For van der Waals heterostructures, this is generally achieved via mechanical exfoliation as thus far it maintains the highest crystal quality whilst being a relatively cheap and easy method [32, 119]. The disadvantage of this exfoliation technique is that crystal thicknesses, lateral sizes and shapes have some unpredictability. Although, in general, crystal thicknesses down to monolayers and lateral sizes up to $\sim$100 µm can be achieved.

Initially, a bulk crystal of the desired 2D material is placed between two pieces of adhesive tape and successive peels of these allow for thinner crystal layers to be revealed. As alluded to earlier, the strong intra-layer covalent bonds and weak inter-layer van der Waals forces inherent in 2D materials allow for the separation of adjacent layers. Generally, it is found that the more homogeneous and laterally large the crystals on the tape, the larger the exfoliated crystals will be in lateral size. It has also been found that certain types of adhesive tape are, generally, more efficient at exfoliating different 2D materials. For graphene and hBN, Nitto Denko's ELP BT-150E-CM tape (also known as 'low-tack', or water-soluble, tape) is found to give the greatest amount of clean, large area thin crystals. While for TMDCs and PTMCs, Nitto Denko's ELP BT-150E-KL (also known as 'high-tack' tape) is found to give the cleanest, largest, thinnest crystals[1]. This tape, alongside other variants, are shown in Fig. 2.2. The Nitto Denko tapes are composed of a base layer of ethylene-vinyl acetate with an adjacent layer of varying strengths of adhesive acrylic (with the exception of ELP BT-50E-FR which has a base layer of polyethylene terephthalate). Ultron tapes may also be used for exfoliation, which consist of a polyvinyl chloride base layer with an adjacent layer of two different strengths of adhesive acrylic and, unlike Nitto Denko's, are not backed by a cover film.

Once a thin layer of the 2D material has been obtained on an adhesive tape, it may be transferred onto a substrate. The choice of substrate will vary for the device being built. In general, there are three substrate types used for exfoliation here. The first is the industry standard Si/SiO_2 wafer which is inexpensive and useful as a dielectric layer for back-gating materials. This type of substrate is typically used for exfoliating crystals which will form the foundation of a van der

[1]Note that these are a part of Nitto Denko corporation's back grinding tape line-up ELEP HOLDER.

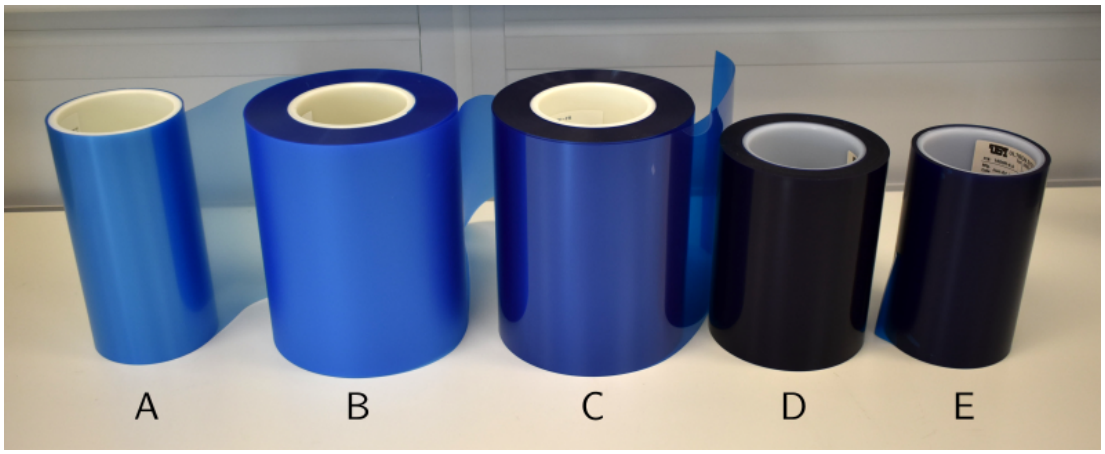

Figure 2.2: Photograph of the varieties of tape available. Nitto tapes (A) ELP BT-130E-SL (B) ELP BT-150E-KL and (C) ELP BT-50E-FR alongside Ultron tapes (D) 1007R-6.0 and (E) 1009R-6.0.

Waals heterostructure (usually hBN). In order to improve the surface adhesion of the SiO_2 to the 2D materials as well as improve the size of exfoliated crystals, it may be soft plasma etched with Ar/O_2 (here as a 4inch wafer for 10minutes at 9W) [120]. The second type of substrate used is a Si wafer with a ∼50nm layer of poly(vinyl alcohol) (PVA) and then a ∼570nm layer of poly(methyl methacrylate) (PMMA) on top. The PVA (10K 3% w/w deionised water) and PMMA (996K 8% w/w anisole) layers are deposited using a spin-coater, to a total thickness of ∼620nm; the reason for this will be discussed in the following section. This type of substrate is generally used for crystals requiring transfer onto other 2D materials; introduced in the following sections. The third type of substrate used is a Si/SiO_2 wafer (SiO_2 thickness 90nm) with a layer of poly(propylene carbonate) (PPC, 300K 5% w/w anisole) spin-coated on top to a thickness of ∼200nm. This type of substrate may be used for exfoliating TMDC and PTMC crystals that are required to be picked up by other 2D crystals.

Once a substrate is selected for exfoliation, it may be heated on a hot plate. The substrates Si/PVA/PMMA and Si/SiO_2/PPC are heated to ∼130°C and ∼70°C, respectively, to increase the surface adhesion. The tape with the 2D material may then be pressed against the selected substrate and left for some time, depending on the crystal. Here, it is suggested that to obtain the largest, thinnest hBN crystals on Si/PVA/PMMA, one should leave the tape on for at least 24 hours. This is suggested to relate to the change in tape adhesion strength over

such timescales. The same method is also suggested to be true for graphene exfoliation onto Si/PVA/PMMA. For exfoliation onto Si/SiO_2, however, the time is minimised as otherwise increased residues may be observable. For Si/SiO_2/PPC, one may still exfoliate large, thin crystals with little to no waiting required. After placing the tape onto the substrate and potentially waiting for some time, the tape may then be peeled off slowly at a shallow angle. This will reveal various sizes and thicknesses of 2D material crystals on the substrate. It is important to note that the 2D materials included here (graphene, hBN, TMDCs and PTMCs) are almost always exfoliated onto a specific substrate type and with this a certain tape type is also recommended. For example, PTMCs are usually exfoliated onto Si/SiO_2/PPC with high-tack tape to give a copious amount of large, thin crystals. One may find greater success using low-tack tape (or another tape) in the case of exfoliation on a different substrate. With this, it is important to try the various tapes on different substrates as this may produce a higher yield of thin 2D crystals.

2.3 2D Crystal Identification

As the process of mechanical exfoliation results in thin crystals of various lateral sizes and thicknesses, a quick process to clearly identify crystals is pivotal in order to build van der Waals heterostructures efficiently. This identification is achieved by maximising the optical contrast of the crystals in a reflected light optical microscope so that monolayers are clearly visible. The optical contrast may be maximised (up to ∼10% for graphene) by choosing a substrate of an appropriate thickness. In the case of Si/SiO_2, a SiO_2 thickness of 90nm or 290nm (giving it a purple-violet colour under white light) provides the highest contrast for graphene, hBN and MoS_2 monolayers at a light wavelength of ∼550nm due to thin film interference [20, 81, 121]. For this reason, polymers are also spun to specific thicknesses. At a wavelength of ∼550nm (equating to green light), the human eye has the greatest sensitivity which also allows for easier perception of thin crystals with slightly different contrasts. Optimising the interference at this wavelength is particularly important for finding monolayers of hBN as they are significantly more transparent than graphene due to their wide band gap, resulting in an optical contrast of ∼1-2% [20]. From this analysis, an optical microscope with narrow bandpass colour filters may be used to select the optimal

wavelength for effective monolayer identification. Figure 2.3 demonstrates that a green filter increases the contrast of a graphene crystal on Si/SiO_2 (290nm) more than red or blue filters. With this, one may also find the incremental increase in optical contrast for successive layer thicknesses in order to gauge how many layers are present to a good approximation. This may be achieved with image processing software such as NIS-Elements.

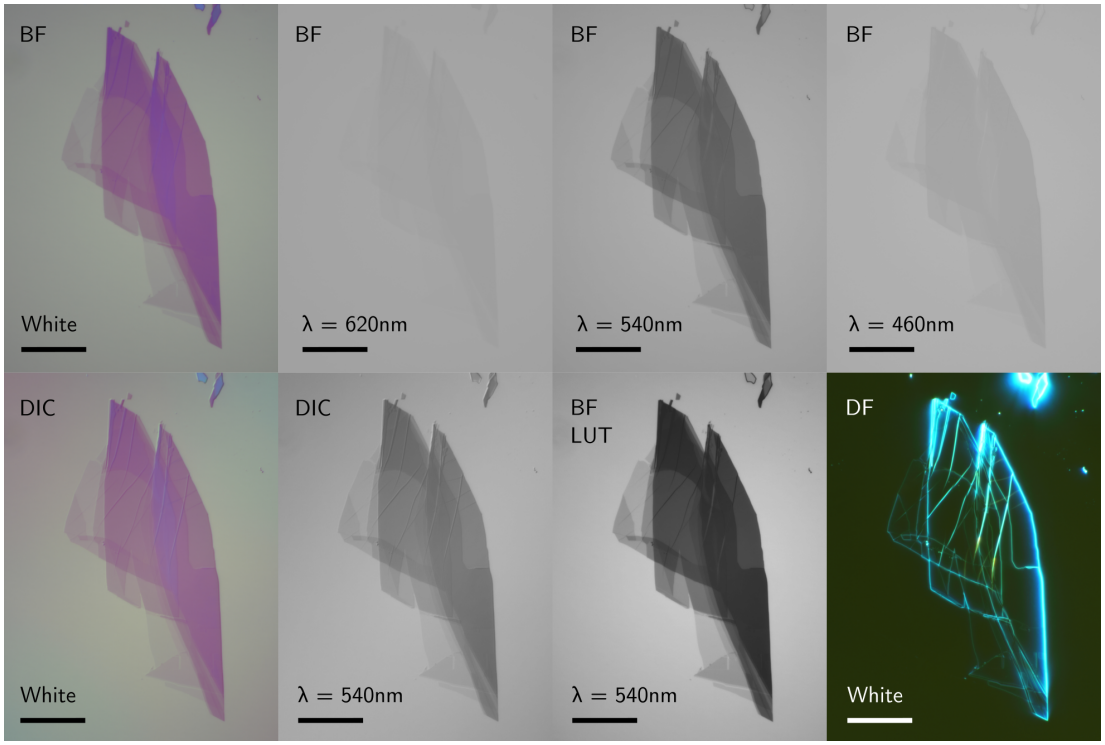

Figure 2.3: A graphene crystal with multiple thicknesses on Si/SiO_2 (290nm). The thinnest parts of the crystal are most visible with the green filter due to the increased optical contrast. Differential interference contrast (DIC) is useful for previewing topographical features of the crystal, with edges and crystal fold lines more clear. The manipulation of look up tables (LUTs) may also enhance the optical contrast. Dark-field (DF) imaging may also reveal topographical details such as crystal edges and fold lines, in this case highlighting them. Scale bar in each image is 20 µm.

Here, a Nikon LV100ND Eclipse microscope is used in reflection mode with a 100x objective lens, numerical aperture 0.9 (TU Plan Fluor BD semi-apochromatic), and a 16.25 megapixel camera (Nikon DS-Ri2). This optical setup allows for high-resolution bright-field (BF), dark-field (DF) and differential interference contrast (DIC) images to be taken. Briefly, BF microscopy produces a standard, reflected white light image of the sample under examination. In DF microscopy,

white light is incident on the sample at an angle. Light scattered by edges or topographical features on the sample are then collected and focussed, forming an image; see Fig. 2.3 for an example of this. This microscopy technique is therefore useful for highlighting edges of crystals and folds or cracks. Importantly, DF may also highlight residue or contamination that is not observable in BF. The most complicated of the three techniques, DIC uses a Nomarski prism (a modified Wollaston prism) to split the incident polarised white light into two perpendicular polarisations that are also slightly displaced from one another once focussed onto the sample. These two polarised rays of light, at slightly displaced positions, may travel down different optical paths in the sample due to changes in thickness or refractive index, giving a phase difference between them. After being reflected, these rays are recombined in the Nomarski prism into one polarisation, with the phase difference between them causing interference which affects the amplitude of the recombined light. As this interference is from optical path differences between adjacent positions on the sample, a 'shadow' is observed with the image appearing three-dimensional. Thus, this technique is useful for previewing topographical features of thin crystals; see Fig. 2.3. Finally, one may also artificially enhance the contrast in the images by manipulating the corresponding look up tables (LUT). These tables map the raw image data into a viewable output image by changing the dynamic range of the digital image. By manipulating the LUT, one can alter the colour mapping and enhance the contrast around a selected light intensity. An example of LUT manipulation used for contrast enhancement of a green filtered BF image of a graphene crystal is shown in Fig. 2.3.

2.4 2D Crystal Transfer

Once thin 2D crystals have been identified and selected, they may be transferred onto other thin crystals or substrates. This may be achieved through two methods, the PMMA membrane 'float and fish' technique or the polydimethylsiloxane (PDMS) stamp technique. The procedures for both methods will be discussed in the following sections for the case of creating a graphene/hBN heterostructure. The current advantages and disadvantages observed in both techniques will also be discussed.

Before transfers are made, the chemically stable crystals may be annealed to 120°C in order to evaporate water off the surfaces. This enhances the van

der Waals attraction between materials as well as reducing the contaminants between layers. In all transfers, it is important that the interface area between the 2D materials be increased as slowly as possible. This sometimes allows for the pushing out of contamination between the materials, leaving larger clean areas.

2.4.1 PMMA Membrane Transfer

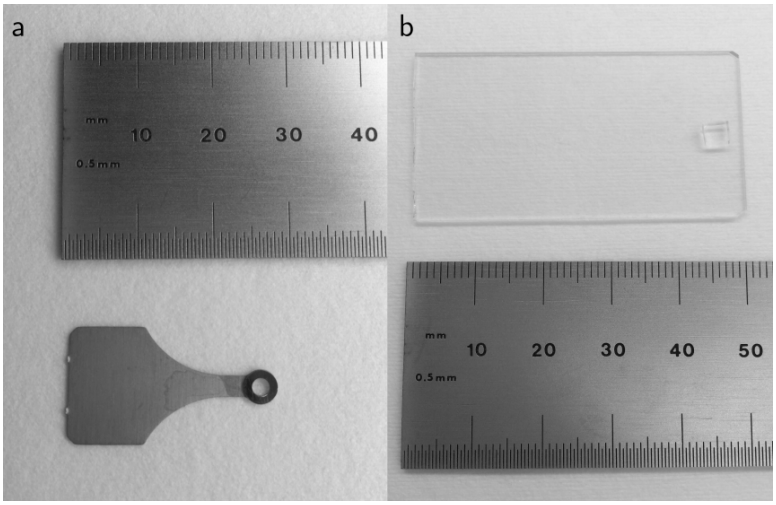

Figure 2.4: Photographs of (a) the stainless steel membrane holder (or plectrum) and (b) a glass slide with the PDMS block alongside rulers for comparison.

In this transfer technique, the thin 2D crystal requiring transfer must first be exfoliated onto Si/PVA/PMMA, as described previously, and then identified. A circle of diameter ∼5mm centred on the chosen crystal is then carved into the PVA/PMMA bilayer with sharp, clean tweezers. This circle must be complete and may be made by following the field of view edge of a 5x lens. Deionised (DI) water may then be carefully applied with tweezers to the circle edges in order to dissolve the underlying PVA layer. Here, it is important to not place water onto the 2D crystal as this would contaminate the surface. It is also important to not to allow the water under the PMMA to dry out. More water may be applied until the PMMA membrane is fully released onto a thin water layer. The substrate holding the membrane may then be dipped into a DI water bath (in a 100ml beaker) at 45° in order to float the membrane on the water's surface.

A stainless steel membrane holder (or plectrum) may also be prepared to 'fish' the membrane out of the DI water bath, see Fig. 2.4a. This membrane holder is first dipped in PMMA (996K 8% w/w anisole) and baked at 150°C for

10minutes to dry. The PMMA is coated onto the holder so that the adhesion to the PMMA membrane is increased, making the 'fishing' easier. Once the holder is prepared, the membrane may be 'fished' out of the water bath carefully so it covers the holder homogeneously and without clear defects. Once the membrane is successfully picked up, the holder may then be placed on the edge of a hotplate at 90°C. This allows the excess water to slowly boil off without damaging the membrane whilst pulling the membrane into tension across the holder. Once dry, the 2D crystal on the membrane is ready for transfer.

The transfer is then achieved through the use of a custom-built micro-mechanical transfer system; see Fig. 2.5. This transfer system consists of a rotatable stage with a vacuum chuck that also has an incorporated heating element. This stage may be manoeuvred in the x and y axes accurately by micro-manipulators. Next to this is an 'arm' in which the membrane is held by a vacuum chuck and positioned by micro-manipulators in the x, y, z axes as well as in two tilt directions. Above these is an optical microscope (modified Nikon Eclipse LV150) in which live viewing either through an eyepiece or a camera is possible.

Initially, the plectrum may be held upside down on the arm by the vacuum chuck so that the membrane is horizontal and above a second 2D material placed on the rotatable stage vacuum chuck. This second 2D material is typically exfoliated onto a Si/SiO_2 or Si/SiO_2/PPC substrate. The stage and arm are then carefully positioned under the 50x objective so that the crystals on the membrane and substrate are aligned as required to a precision of $\sim$1 µm. The heating element in the stage may then be switched on for greater inter-layer adhesion and a softening of the PMMA which allows for better control of the interface between the materials. Typically, the temperature is raised to between 45-65°C. In this range, the PMMA acts smoothly and more predictably, neither being too cold and brittle nor too hot and melting. Once aligned, the arm is lowered carefully until the two crystals are brought together. This may require the poking of the PMMA membrane with a blunt instrument to begin adhesion to the substrate. It is also advisable to bring the materials together slowly, as this allows for greater control and the possibility of contamination reduction. With successful adhesion of the thin crystals, the arm (and thus the membrane holder) is lifted up slowly. This will either leave the 2D materials on the stage substrate or lift them up with the PMMA membrane. Which scenario occurs is usually dependent on the relative size of the 2D materials, with the smaller crystal usually following the

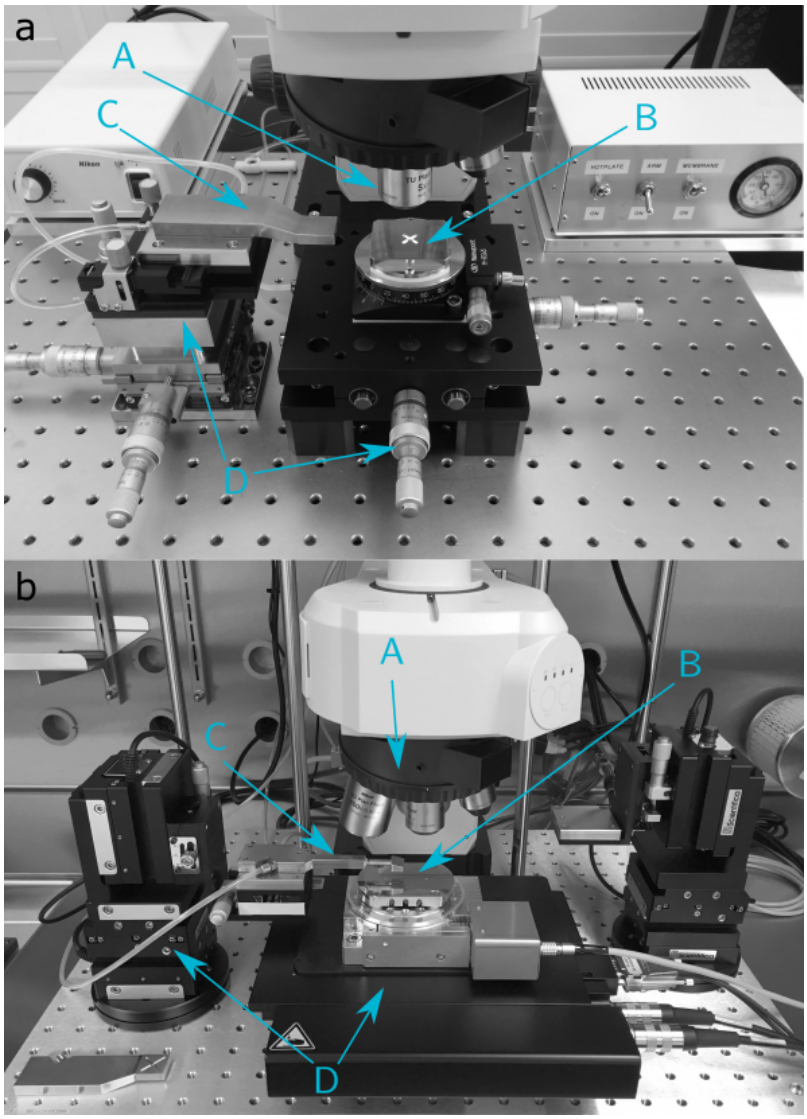

Figure 2.5: Photograph of custom-built transfer systems that are (a) outside and (b) inside a glovebox system. A microscope (A) is positioned above a rotatable stage with a vacuum chuck and incorporated heating element (B). An 'arm' (C) holds the membrane via a vacuum chuck over a stage which may be adjusted through micro-manipulators or motors (D). The transfer system inside the glovebox includes a motorised microscope, stage and arm.

larger crystal's original surface (i.e. if a hBN crystal on PMMA is laterally larger than a graphene crystal on SiO_2, the graphene and hBN will be lifted up with the PMMA). This observation may be used advantageously as one can pre-select crystals with the larger of the two being the 'direction' of the desired transfer. This can also be used advantageously for encapsulation: by selecting a medium area hBN crystal on Si/PVA/PMMA, one may be able to pick up a smaller area

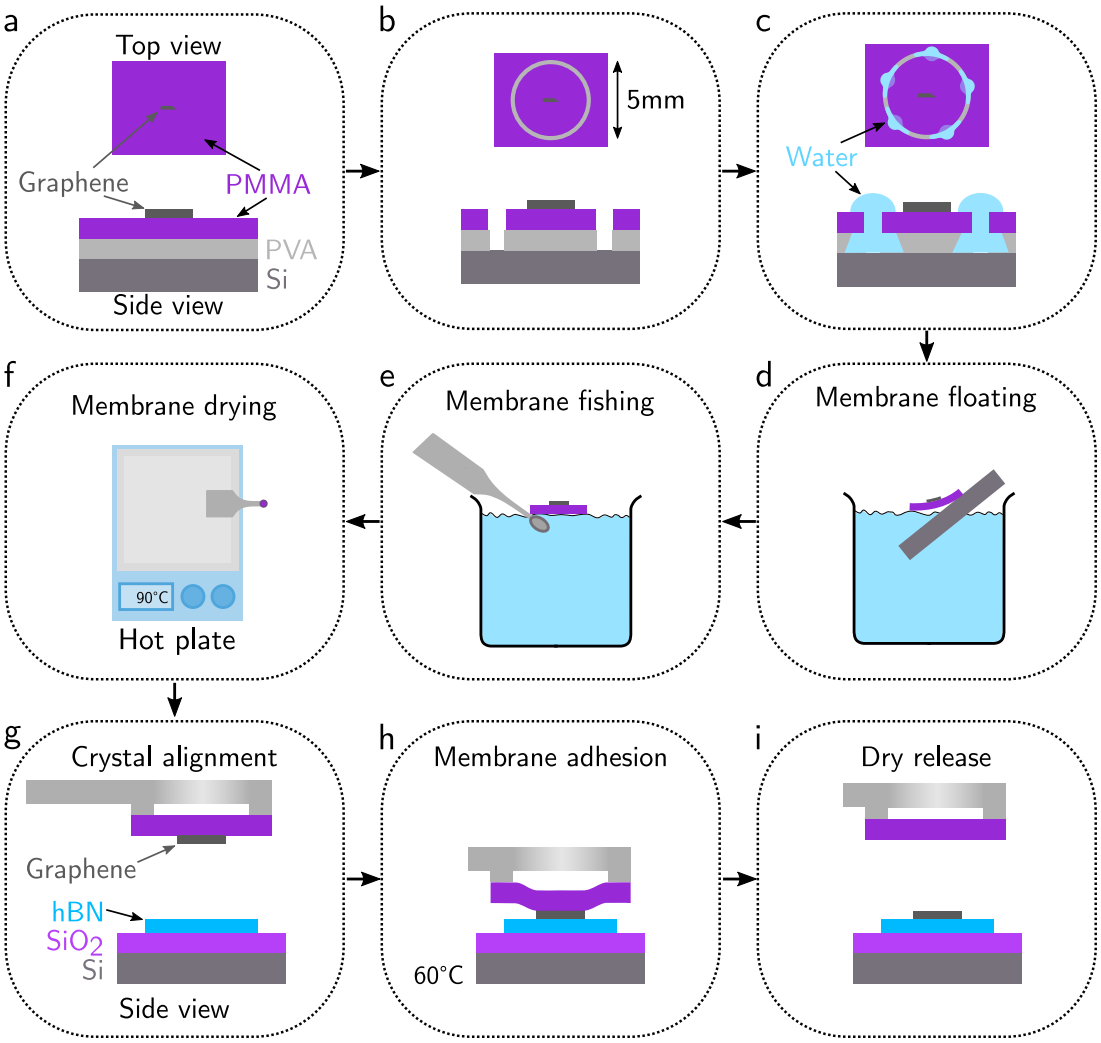

Figure 2.6: Schematic illustration of the PMMA membrane transfer method. (a) a thin crystal is selected and then (b) the surrounding PMMA is cut using tweezers for (c) DI water to be deposited such that the underlying layer is dissolved. The membrane is then (d) floated in a DI water bath and (e) fished out using a membrane holder and (f) subsequently dried. The membrane holder is then (g) positioned such that the crystals are aligned and (h) brought close enough to adhere. Finally, the membrane is (i) peeled to release the crystal.

2D material and then deposit this stack onto a larger area hBN crystal exfoliated onto Si/SiO_2. These transfers are known as dry transfers as no solvents come into direct contact with the 2D crystals. The full process is illustrated in Fig. 2.6.

If the crystals are not dropped down on a substrate as required, an alternative method for removing the PMMA is possible. In this case, one can cut the PMMA membrane off the plectrum using sharp tweezers and then heat the substrate on a

hot plate for 30seconds at 90°C. Afterwards, a thin layer of PMMA may be spun onto the cut membrane. With this extra PMMA layer, the substrate is placed in a bath of acetone for 10minutes. The thin layer of PMMA was spun in order to stop the acetone lifting the membrane up too quickly and ripping the 2D crystals off. After 10minutes, the solvent will have dissolved the PMMA, leaving the thin crystals on the substrate. Immediately after the acetone bath, the substrate is washed in an isopropyl alcohol (IPA) bath for 30seconds and subsequently blowed dry with a nitrogen gun. This type of transfer is known as a wet transfer and typically results in more contamination than dry transfers.

2.4.2 PDMS Stamp Transfer

The PDMS stamp technique first requires the creation of a PDMS/PPC stamp. This is achieved as follows. PDMS is initially prepared from SYLGARD 184 elastomer which is mixed 10:1 base to curing agent in a petri dish. This petri dish is then placed into a vacuum desiccator for ∼10minutes until the bubbles are drawn out. The SYLGARD 184 elastomer mixture is then dripped carefully onto a silicon substrate (∼4inch diameter) and, once settled and flat with a thickness of ∼2mm, baked at 150°C for 10minutes in order to solidify into PDMS. Alternatively, one can use Gel-Pak 4 sheets as a PDMS base layer. Once solid, the PDMS may be plasma cleaned with Ar/O_2 (here for 10minutes at 30W) in order to increase surface adhesion to PPC. Immediately after cleaning, PPC (50K 15% w/w anisole) is spun twice to a total thickness of ∼5 µm. Finally, the PDMS/PPC may be cut into rectangular blocks (∼5mm×2mm) and stuck PDMS side down onto glass slides (∼50mm×25mm) using PVA. Alternatively, one may place the PDMS onto a soft plasma cleaned (with Ar/O_2) glass slide and then place in a vacuum in order to remove bubbles between the PDMS and glass slide, promoting adhesion. Finally, the glass slide and PDMS/PPC block may be heated for 1hour at 130°C to also improve adhesion. A typical PDMS/PPC block on a glass slide is shown in Fig. 2.4b. [122]

For the PDMS stamp technique, the crystals requiring transfer should be exfoliated onto Si/SiO_2. In the case of hBN encapsulation, a hBN crystal must be picked up first, using the same custom-built micro-mechanical transfer system; see Fig. 2.5. Initially, the glass slide with a PDMS/PPC block is held upside down on the arm by a vacuum chuck. The PDMS/PPC is then positioned above the substrate with hBN crystals on a Si/SiO_2 substrate held on the rotatable stage

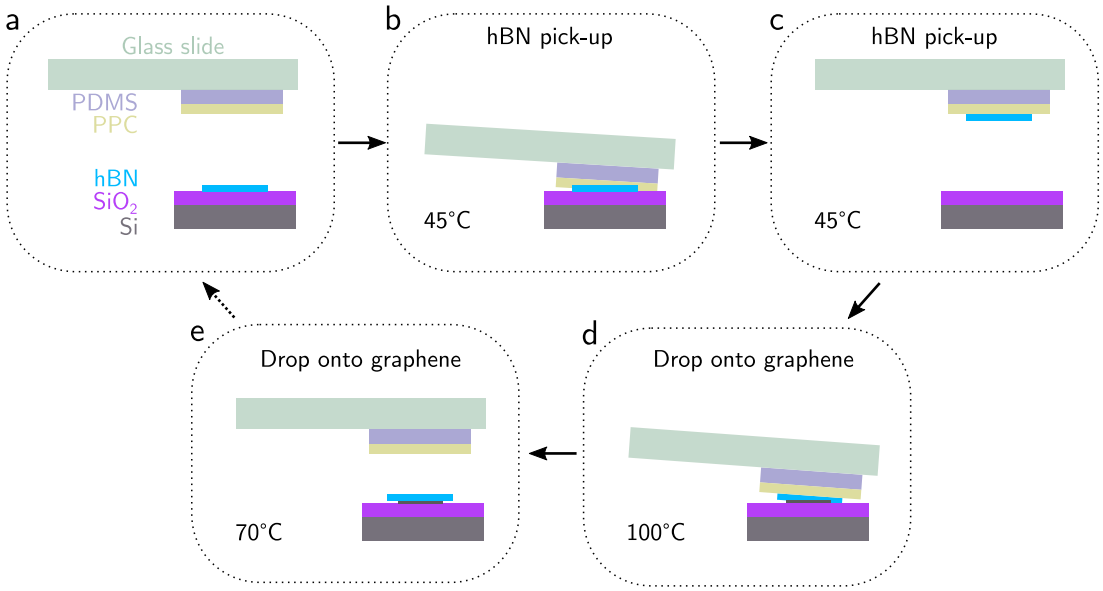

Figure 2.7: Schematic illustration of the PDMS stamp transfer method. (a) A thin crystal is selected and then (b) a PPC/PDMS block is placed down onto it and (c) quickly lifted up at 45°C to pick up the crystal. Then, the crystal may be (d) aligned to and placed onto a second crystal at 100°C to push out contamination. The heterostructure may be (e) released from the PPC/PDMS block by raising it at a temperature of >70°C.

vacuum chuck. The PDMS/PPC block is then slowly lowered until the PPC is brought into contact with the substrate at a temperature of ∼45°C. Once the PPC covers the crystal to be picked up, the glass slide (and PDMS/PPC block) is quickly raised to disengage it from the substrate. The desired crystal should remain attached to the PPC and be picked up. This crystal is then positioned and lowered slowly onto a second 2D material at a temperature of ∼100°C. In this case, the PPC contact frontline should be brought close to the second 2D material but not immediately into contact with it. In order to push out contamination and have a smooth interface between the two 2D materials without bubbles/blisters, one may push the PPC contact frontline towards the second 2D material by increasing the temperature of the stage in 0.1°C increments. This leads to thermal expansion of the PDMS and a slow contact of the interfaces. This should be continued until full contact between the two 2D materials is achieved. Upon full contact, the 2D materials may be dropped down onto the substrate by raising the glass slide upwards at a temperature of ∼70°C. At this temperature, the PPC behaves as a liquid, allowing the crystals to be dropped down. Figure 2.7 illustrates the stages of the PDMS stamp technique. The improved adhesion of the PPC to

the PDMS via the etch cleaning process stops PPC delamination from the stamp [122]. Once dropped down, the 2D materials are baked at ∼150°C for 30minutes (assuming they are chemically stable) to improve their mutual adhesion. After baking, the crystals may be picked up and dropped down onto a third crystal by repeating this process. It is worth noting that transfers using a PDMS/PMMA block are also possible, with different temperatures required for the picking up and dropping down of the 2D materials.

2.4.3 PMMA vs PDMS

The two transfer techniques currently available for stacking thin 2D crystals have distinguishable advantages making them useful for different fabrication scenarios. The advantage of the PDMS stamp technique is that large, contamination free interfaces between crystals are possible due to the better control over the interface frontline. However, this technique suffers from some drawbacks. Picking up an initial crystal with a thickness <5L is difficult. Also, as the stamp consists of multiple layers of different refractive indices, the visibility of the crystals is reduced. This results in an increased difficulty in accurately aligning crystals in comparison to PMMA membrane transfers, which retain a high optical contrast. Moreover, the PMMA membrane technique may be employed when transferring crystals onto delicate substrates such as transmission electron microscopy grids, whereas the PDMS stamp may damage these due to the applied pressure. A disadvantage for the PMMA membrane technique is that it requires significant care when picking up the membrane.

Overall, for heterostructures not requiring a thin top crystal but large, clean interfaces (e.g. hBN encapsulated graphene), the PDMS stamp technique is preferable. However, for heterostructures requiring a thin top layer or placed on delicate substrates (e.g. transmission electron microscopy or optical samples) the PMMA membrane technique is preferable. [123]

2.5 Air-Sensitive Materials and Encapsulation

As 2D materials are atomically thin, they have a large surface to volume ratio. This suggests that the properties of 2D materials are highly sensitive to the state of their surfaces. As such, contaminants that are adsorbed onto the surfaces of 2D materials can have a dramatic effect. When fabricating heterostructures to

improve the understanding of the intrinsic properties of materials, it is imperative that the surfaces or interfaces be as clean as possible. For this reason, exfoliation and the building of heterostructures is preferably performed in a cleanroom environment whereby the air has been purified and filtered to remove various particulates. This, however, does not completely rid the surfaces of molecular contamination.

Beyond the effect of contaminants, oxygen and water may also react with certain 2D material surfaces, degrading their crystal quality. For stable materials such as graphene and hBN, this is suggested to not occur. But for some TMDCs and many other 2D materials, this can be a major limiting factor towards their investigation. Amongst these materials, the rate at which this degradation occurs varies. For some TMDCs, without protection the morphology and optical response is suggested to change and degrade significantly over the course of several months [124, 125]. For black phosphorus, this degradation occurs over much shorter timescales of several hours [34, 125]. Similarly, niobium diselenide has also been found to deteriorate rapidly after exposure to air [34, 125]. More recently, investigations have uncovered ferromagnetism in atomically thin chromium triiodide layers [126]. However, these crystals are perhaps the least stable of those described thus far, with complete degradation in air possible over a few minutes [127]

Post-transition metal chalcogenides have also been found to be susceptible to deterioration in air. A previous report has suggested that bulk GaSe reacts with oxygen to form gallium oxides and selenium oxides in a thin outer film [128]. It has also been suggested that this oxidation destroys ultrathin GaSe as the products completely take up the crystal [129].

The deterioration of GaSe crystals in ambient conditions has also been observed here. After placing a bulk GaSe crystal onto hBN and leaving it in ambient conditions for a number of days, the GaSe crystal was observed to change in appearance dramatically, see Fig. 2.8. Also, a significant peak at a Raman shift of $\sim$250cm^{-1} was found to exist only in the regions of this change in appearance which is generally found to be near the crystal edges; see Fig. 2.8. This reproduces previous observations that suggests a peak at $\sim$250cm^{-1} to be due to amorphous selenium; a by-product of reactions between GaSe and O_2 [129]. This, as well as the lack of characteristic Raman modes for GaSe, clearly indicates the crystal edge to have deteriorated significantly in its chemical composition. The Raman

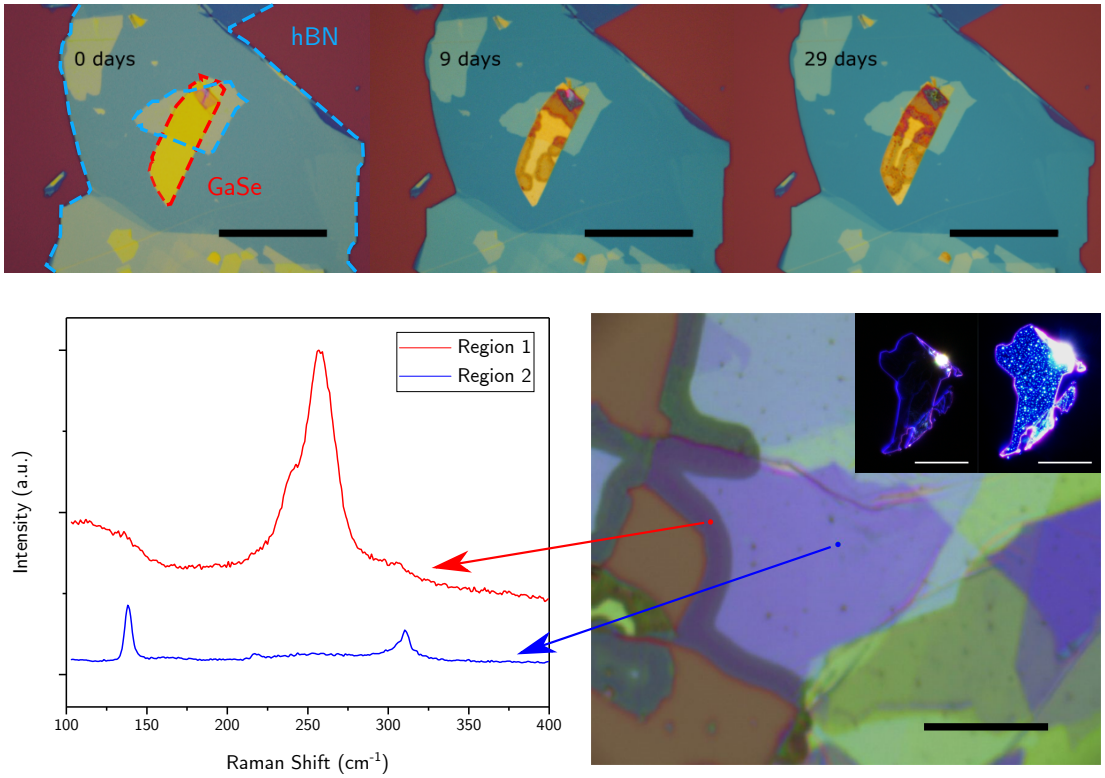

Figure 2.8: Top: Optical images of a GaSe bulk crystal (red dashed outline) on hBN (blue dashed outline) that was left in ambient conditions for around 1 month. During this time, significant degradation is observed to occur over the whole crystal. Bottom: Raman spectra at two regions of an exfoliated bulk GaSe crystal exposed to ambient conditions for 6 weeks. The GaSe shows complete deterioration at region 1, with a different Raman spectrum observable, whilst only some oxidation is found at region 2 as the peaks characteristic of GaSe are retained. Inset: Dark-field images of a GaSe crystal (left) immediately after exfoliation and (right) three days after exposure to ambient conditions. Scale bars in each image are 25 µm .

spectra from the central region also closely matches that of GaSe capped with oxidised GaSe; see [129]. Interestingly, the deterioration front is observed to continue into the crystal over the next few weeks, demonstrating that protecting the edges of GaSe is particularly important for material stability. Moreover, GaSe crystals exposed to air are found to increase in thickness significantly. Figure 2.9 shows a GaSe terraced crystal encapsulated by a thin top layer of hBN. In this thin layer of hBN, there is a crack which leaves a strip of GaSe of different thicknesses exposed to air. These exposed regions are significantly thicker, with monolayer GaSe thickness increasing from ∼0.8nm (encapsulated) to ∼2.5nm.

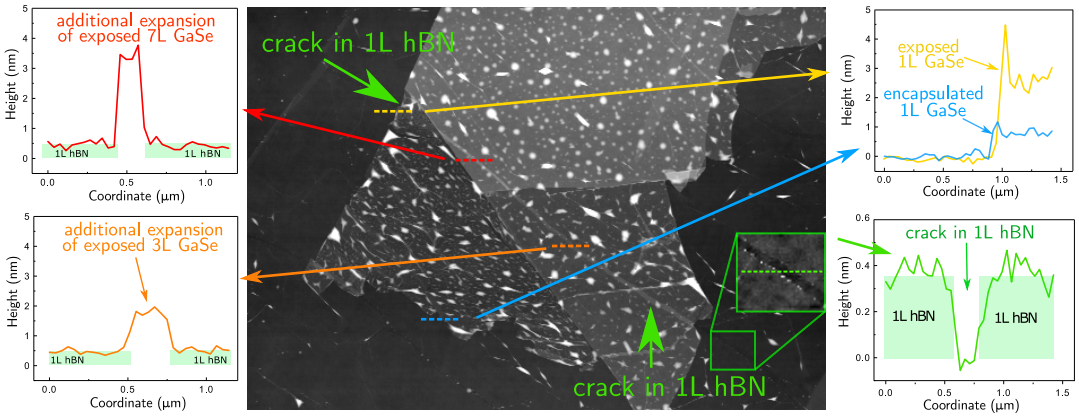

Figure 2.9: Atomic force microscopy height map of a hBN encapsulated GaSe thin terraced crystal. A crack in the top monolayer hBN layer leaves a strip of the GaSe exposed to air. This strip of exposed GaSe shows a significant increase in thickness.

Like GaSe, InSe is also unstable in ambient conditions. As with GaSe, the production of indium oxides and selenium oxides for InSe exposed to air has been reported [130, 131]. However, PL peak intensities at 10K have been observed to degrade at a slower rate than GaSe [74]. The preferred oxidation reactions have been reported to be different for InSe and GaSe, possibly explaining this difference in degradation speed [131]. Interestingly, some reports have suggested InSe to be stable under ambient conditions [82, 132, 133]. Here, InSe has been found to degrade when exposed to air but to a less significant extent than that of GaSe; with no progressive edge deterioration observable.

Although performing exfoliation in a cleanroom is helpful, it doesn't stop degradation of many 2D materials occurring due to their exposure to air. Thus, to reduce this exposure, an argon filled MBRAUN glovebox is used for the mechanical exfoliation of 2D materials and subsequent transfers, with an oxygen and water content at <0.1ppm. Figure 2.10 shows two such gloveboxes. The right box contains a plasma etcher cleaning system, storage space for crystals and devices and hot-plates for exfoliation. The left box contains an integrated deposition chamber and a motorised transfer system. The deposition chamber allows for metallic contacts to be directly placed onto the 2D materials without them having to be exposed to air. This requires pre-patterned stencil masks which may be formed from PMMA and accurately placed on the material using the transfer system. The transfer system in the glovebox is that shown in Fig.

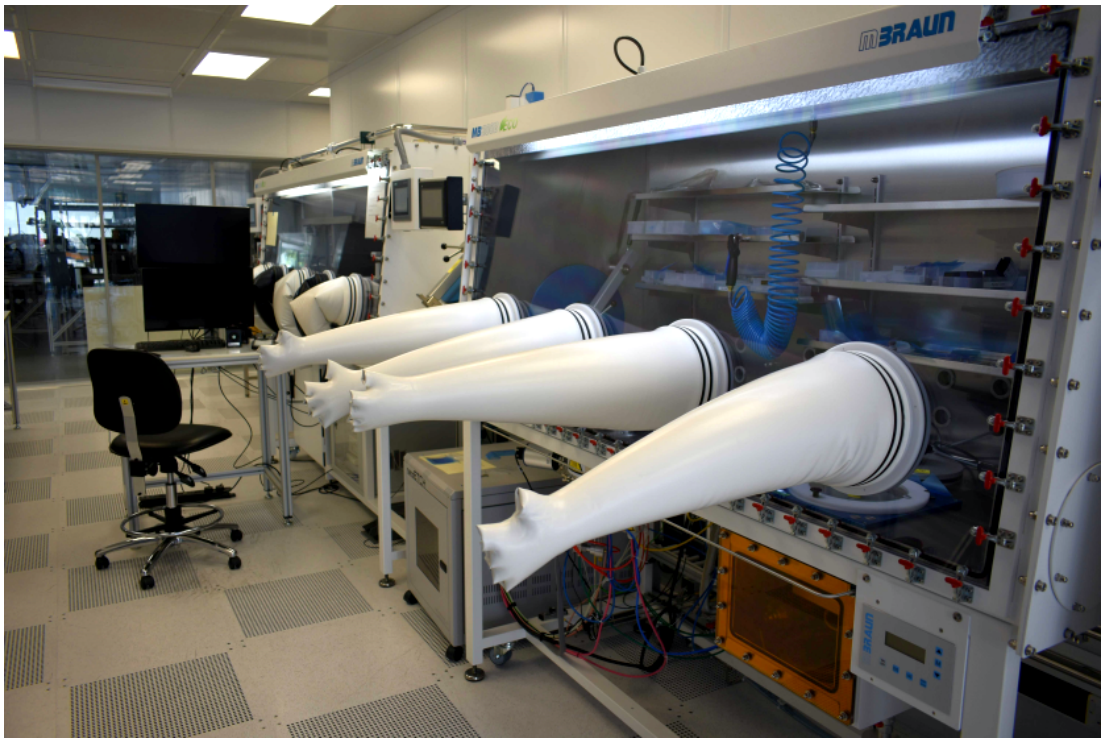

Figure 2.10: A photograph of the argon glovebox in Manchester used for exfoliation and transfer of air-sensitive 2D materials. The left box contains a motorised transfer system and a deposition chamber. The right box contains a plasma cleaning system, a spin-coater and storage space for crystals and devices. Samples may be transferred between boxes through a connecting antechamber. The atmosphere in both boxes is automatically maintained so that the H_2O and O_2 concentrations remain <0.1ppm.

2.5b, with most of the components motorised for ease of use and improved accuracy. These motorised components include the objective lens nosepiece, the microscope z-height, the narrow bandpass filters, the stage x, y and rotation axes and the transfer arm x, y and z axes. These may be manipulated through the use of controllers outside of the glovebox. The motorised components allow for the transfer of crystals to be easier for two reasons. Firstly, they reduce the need to use the gloves for handling the transfer process. These large and thick gloves make delicate procedures more difficult as well as adding undesirable vibrations to the transfer system. Secondly, the motorised stage and transfer arm may be more accurately controlled, allowing for better alignment of crystals. At it is motorised, the transfer system is also programmable, allowing for the implementation of software features that streamline the crystal search and transfer processes.

With this glovebox system available, one may exfoliate 2D materials using the same techniques described earlier but now under an argon atmosphere. These crystals may then be identified and selected using the motorised stage of the transfer system. Once found, they are encapsulated in more stable 2D materials, such as graphene or hBN, and then taken out of the glovebox without being exposed to air. This encapsulation is now a standard technique that is widely advised for van der Waals heterostructure fabrication; not only for improving sample quality but also for retaining crystal integrity [34, 35, 74, 123, 134]. In this thesis, all 2D materials that are investigated are first exfoliated in a glovebox and then encapsulated in either hBN or graphene. For optical studies, hBN encapsulation is used due to its minimal influence on the material's optical properties. For transmission electron microscopy and angle-resolved photoemission spectroscopy studies, graphene is used for charge removal.

2.6 Annealing

As briefly mentioned earlier, contamination may be trapped between 2D crystals during their transfer. This contamination is mostly composed of hydrocarbons that are trapped during the fabrication processes or adsorbed from the atmosphere in which the fabrication was undertaken [135]. This contamination is typically observed to form a thin film between the 2D crystals with some small 'bubbles' observable where the contaminants have begun agglomerating.

Upon annealing a heterostructure at $\sim$100°C or higher, the small bubbles may merge together or grow larger as adjacent contamination agglomerates together. This then eventually leaves behind large, clean interface regions interspersed with islands of larger bubbles; see Fig. 2.11. This is known as the self-cleansing process and is commonly used advantageously in van der Waals heterostructure fabrication for forming clean, uncontaminated regions. The bubble formation, and thus the self-cleansing process, is driven by competition between the van der Waals attraction between the crystals (which squeezes the contamination together) and the elastic energy required to create them [136]. This self-cleansing is observed to be effective for graphene and hBN crystal interfaces, where micron-scale clean interfacial regions between the crystals may be formed [135]. This is due to the similarity of their crystal structures, with their similarly strong in-plane stiffness (Young's modulus) being suggested to be a key factor [136]. Other

crystal interfaces, such as TMDCs and hBN, are suggested to self-cleans less effectively due to the higher density of surface defects inherent to TMDCs as well as them being crystallographically more distinct, resulting in dissimilar in-plane stiffnesses [136].

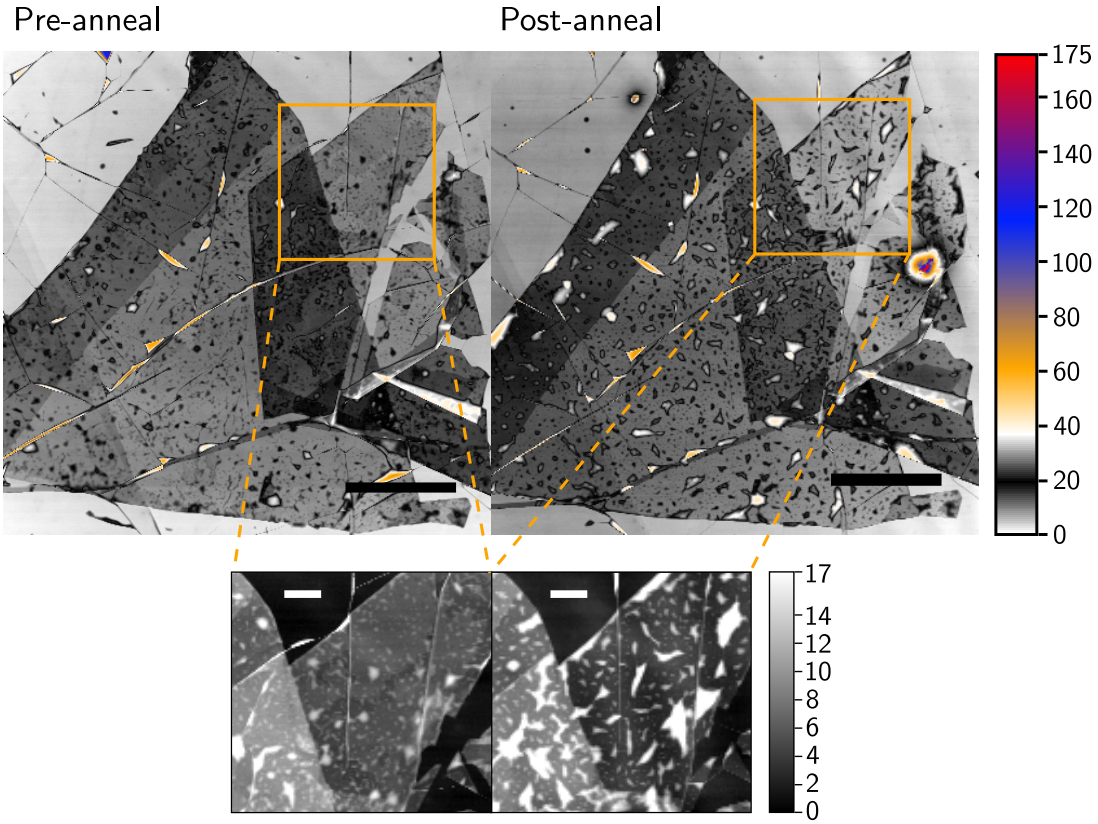

Figure 2.11: Atomic force microscopy height map of a hBN-encapsulated GaSe thin terraced crystal before and after annealing at 150°C for 15minutes. After annealing, contamination between the crystals agglomerates, leaving clean areas between the crystals. Scale bars 5 µm and 1 µm.

An example of a hBN-encapsulated GaSe crystal before and after annealing at 150°C for 15minutes is shown in Fig. 2.11. Here, an atomic force microscope measures the surface height across the heterostructure (this technique is explained in the following section). As is demonstrated, before annealing fewer bubbles are observable. After annealing, the bubbles are greater in size, leaving between them cleaner interfaces in which the GaSe is at a lower height than prior to annealing. Interestingly, annealing at this temperature has little effect on the bubbles formed between the hBN crystals (see the top left position of the images in Fig. 2.11); demonstrating the difference in the self-cleansing strength for other crystals. As

annealing can improve the interfacial cleanliness, here it is employed for almost all of the heterostructures fabricated with the exception of those including monolayer $MoSe_2$ as this is suggested to degrade beyond ∼100°C (even when encapsulated in hBN under an argon atmosphere); see Sec. 6.3. Importantly, it has previously been observed that annealing may also accelerate oxidation and degradation of some 2D crystals such as WS_2 and MoS_2 monolayers [124]. However, encapsulation of these crystals was also found to significantly reduce this effect [124]. Here, all annealing processes are performed at a maximum temperature of 150°C in a glovebox under an inert, argon atmosphere. This technique is employed to reduce any oxidation or degradation. With the exception of monolayer $MoSe_2$, all 2D crystals studied here (when successfully encapsulated in hBN) are suggested to be stable up to this temperature; with no salient deterioration of their optical properties observable immediately after this process.

It is important to note that annealing is not the only technique available for creating cleaner interfaces between 2D materials. One may also try to use PDMS/PPC stamps to 'push' out contamination caught between crystals (as discussed in Sec. 2.4.2), use less or cleaner polymers during the fabrication processes (this is utilised in Ch. 6 and discussed in Sec. 6.3) or even use an atomic force microscope tip to squeeze the contamination out (known as nano-squeegee) [137].

2.7 Atomic Force Microscopy

As demonstrated in the previous sections, atomic force microscopy (AFM) is a useful tool for obtaining a high-resolution image of the surface topography. This microscopy technique is well-known and is a staple for nanofabrication. It is particularly useful for 2D material research as it can accurately measure crystal thicknesses; pivotal for heterostructure building. It is also useful for assessing contamination, cracks, and any abnormality in heterostructure interfaces that may be affecting other measurements. Here, all crystal thicknesses are measured by AFM.

Atomic force microscopy can map the topography of a sample by a few different methods. Here, tapping mode is selected as its less likely to damage the surface. In tapping mode a small tip (scale of nm's) on a resonantly oscillating

cantilever is positioned close to the sample surface. When this oscillation amplitude is altered due to attractive forces from the surface, a feedback loop corrects for this, changing the height of the tip to recover the original amplitude. From the changes in the oscillation amplitude and tip height measured over an area, a surface map may be produced. Here, a Bruker Dimension FastScan is used with ScanAsyst Fluid+ probes that have a nominal tip radius of 2nm.

2.8 Further Fabrication Procedures

Once a van der Waals heterostructure is built, further processing may be required in order to create various devices. Initially, a versatile fabrication process known as electron beam lithography may be used. In this process, an electron-sensitive resist is exposed with an electron beam which either increases or decreases the resist's solubility, known as positive or negative resists respectively. Thus, one may obtain a high resolution pattern (for example in the form of a Hall bar) on a heterostructure by exposing an adjacent resist to a specified electron beam design.

Such patterns are then developed by a solvent, leaving the same pattern exposed directly onto the heterostructure. With this, one may etch or deposit metals onto the selected parts of a heterostructure. These are important processes that allow for a wide variety of devices to be fabricated. In this thesis, all van der Waals heterostructures are investigated for their optical properties and no etching or metallic contacts were required. However, it is of note that during my doctoral studies, I used these techniques to fabricate multiple samples for various investigative efforts.

2.9 Ultra-high Vacuum Fabrication

Great improvements to material quality and to the scope of 2D material research has been achieved by the implementation of glovebox technology. However, despite this, intrinsic 2D material properties and phenomena found in their heterostructures are still hindered by contamination; i.e. bubbles. This contamination is mostly composed of hydrocarbons [135], potentially adsorbed to crystal surfaces at various stages of the fabrication process. To reduce this contamination and significantly improve the heterostructure quality again, a concerted

effort at Manchester has been given towards the creation of an ultra-high vacuum (UHV) fabrication system. The goal of this system is to rid the whole process of the use of polymers, which may leave hydrocarbon residue, and to exfoliate and transfer the crystals in an UHV ($\sim 10^{-10}$mbar). Once these heterostructures are built, further fabrication processes such as etching and deposition will also be available through transfer, also under vacuum, to other dedicated chambers. Figure 2.12 previews this UHV system. Throughout these doctoral studies, I have contributed to the design and testing of this UHV system by building a custom optical spectroscopy setup, further discussed in Ch. 3.

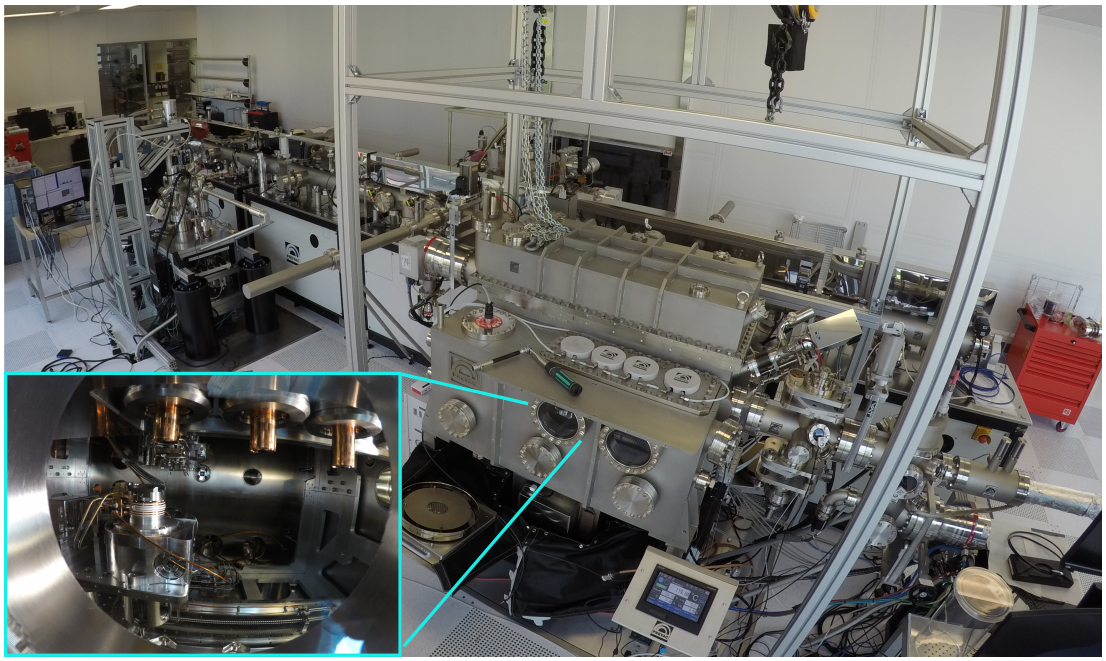

Figure 2.12: Photographs of the ultra-high vacuum system in Manchester. The right hand chamber contains the (inset) transfer arm and stage which are positioned underneath four mounted objective lenses. The central train system allows for samples to be transferred between chambers whilst remaining under a high-vacuum. The chamber on the left is for scanning tunnelling microscopy measurements whilst the central chamber is for deposition.

2.10 Summary

In this chapter, the fabrication methods used for the building of high quality van der Waals heterostructures were described. Initially, high quality bulk source crystals are mechanically exfoliated with adhesive tape and the thin 2D crystals

identified with optical microscopy techniques. These 2D crystals may then be selectively stacked through the use of either a PMMA membrane or PDMS/PPC stamp technique to form van der Waals heterostructures. The problems of air-sensitive 2D materials and their solution via hBN encapsulation in a glovebox were discussed. Then, the usefulness of annealing in forming clean crystal interfaces and their verification via atomic force microscopy are given. Lastly, additional fabrication methods as well as future methods inside an ultra-high vacuum are introduced. The techniques for optically characterising 2D materials are given in the following chapter.

Chapter 3

Optical Characterisation of 2D Materials

Characterising 2D materials and their heterostructures is pivotal for obtaining a greater understanding of their fundamental properties. Optical techniques for such characterisation are particularly useful as they can non-invasively probe various aspects of a material including crystallographic and band structure information. Here, the optical characterisation techniques that are typically used for probing 2D materials are discussed with an introductory summary followed by an overview of their experimental implementation.

3.1 Photoluminescence Spectroscopy

Generally, photoluminescence (PL) is described as the emission of light that occurs after higher energy light is incident on a material. Such a process can occur in many different materials over varying timescales; giving rise to subcategories such as phosphorescence and fluorescence. Here, PL processes in semiconductors are focussed on. In a semiconductor, the Fermi level is positioned in an energy gap between the electronic conduction and valence bands. As such, at low temperatures, the probability of the existence of electrons above this gap (in the CB) are low. However, if photons incident upon a semiconductor have sufficient energy then they may be absorbed, exciting electrons (photo-excitation) to a higher energy above the band gap and into the CB. These electrons may then relax non-radiatively down to the lowest energy state at the CBM through phonon interactions. Simultaneously, as some electrons are removed from the

energy bands below the band gap (VB), vacancies - or electron holes - form in these bands. These holes can be considered as quasiparticles with negative mass and opposite momentum, spin and charge to that of their respective electrons [57, 138]. These holes may also non-radiatively relax to the VBM (the lowest energy state) through similar processes to the electrons. One can also consider this as the electrons in the VB relaxing to lower energies, leaving the vacancies at the VBM. With electrons and holes at the CBM and VBM, respectively, they may recombine to emit photons (radiative recombination) around the band gap energy. The energy of this luminescence is therefore indicative of the semiconductor's band gap energy. The photon emission process has a greater probability for a direct band gap than for an indirect band gap as it does not require an additional phonon scattering event to overcome the momentum mismatch of the CBM and VBM. These processes are demonstrated in Fig. 3.1.

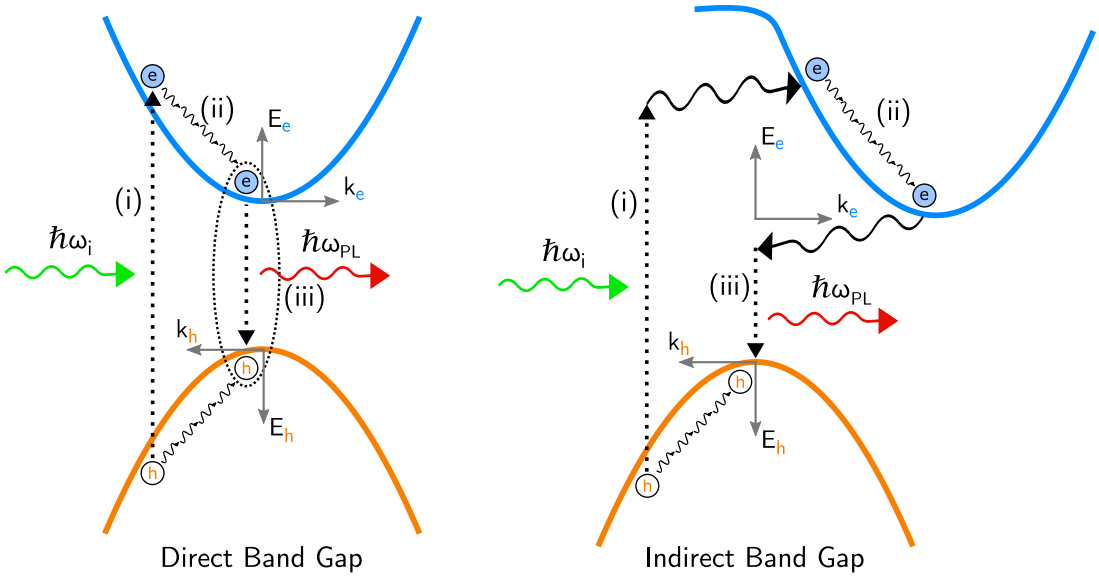

Figure 3.1: Schematic demonstrating the process of photoluminescence in the case of direct and indirect band gaps. Initially, (i) electrons are excited by photons (energy $\hbar\omega_i$) from the valence band (orange) to the conduction band (blue). The charge carriers then (ii) relax via non-radiative processes to the CBM and VBM and finally (iii) recombine to emit photons of energy $\hbar\omega_{PL}$. In the case of an indirect band gap, the recombination process also requires a significant momentum shift that may occur through phonon emission or absorption.

As an electron and hole have opposite charge, they may be attracted through a Coulombic interaction to form a composite quasiparticle known as an exciton. The exciton wavefunction mimics that of atomic hydrogen and thus so does its

energy spectrum, with a ground state ($n = 1$) forming below the free electron band gap. This ground state corresponds to the largest exciton binding energy available. Higher energy exciton states may also form ($n > 1$) with corresponding lower binding energies. When the semiconductor is reduced from three to two-dimensions, the electrons and holes are confined closer to one another. This has the effect of decreasing the exciton Bohr radius as well as increasing the binding energy and the oscillator strength due to the increased overlap of the electron and hole [139]. Note that the oscillator strength gives the probability that a transition between energy levels will occur for electromagnetic radiation-induced oscillating dipoles, thus describing the probability of absorption and emission of light [139]. Due to the reduced dimensions, excitons in 2D semiconducting TMDCs typically have a strong binding energy. Excitons in TMDCs are generally considered to be of the Wannier-Mott type. Wannier-Mott excitons have a Bohr radius that is larger than the lattice spacing (few nm's), corresponding well with the strong binding energies of the order 0.5eV observed for TMDCs monolayers [57]. As the energy of the PL from the excitonic states may be significantly lower than that of the electronic (single-particle) band gap, an 'optical band gap' is defined in accordance with the ground excitonic state, as the lowest energy optical transition; see Fig. 3.2a.

Other luminescence emission routes are also possible. These include free electron and hole (band-to-band) transitions, free-to-bound transitions, donor-acceptor transitions, trion states, higher energy "hot" PL as well as non-radiative relaxation routes from charge traps [140]. These are summarised in Fig. 3.2b. Each emission route may be identification by careful analysis of PL peak characteristics. Trions may be understood as charged excitons (either as an exciton with an additional electron or hole). Typically, binding energies of secondary charges onto excitons are small (a few meV) [141]. However, in 2D systems, as with exciton binding energies, this is enhanced to 10s of meV [53], and therefore observable in PL spectra as a peak shifted to below that of the exciton. So-called hot, or higher energy, PL may also be observed (in exceptional cases) if electron-hole pairs recombine before relaxing to the CBM and VBM [140].

Another useful technique that is closely related to PL is that of photoluminescence excitation spectroscopy (PLE). This technique measures the PL peak intensity of a material as the incident light (excitation) energy is varied. This then indicates the energies at which photons are more strongly absorbed, as this

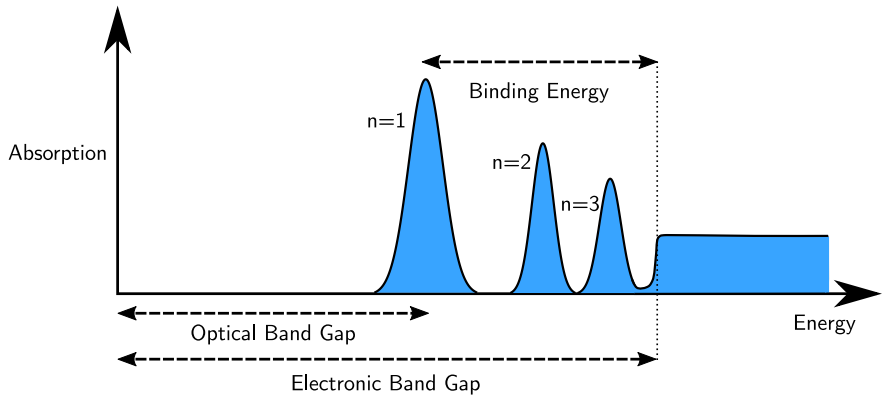

(a)

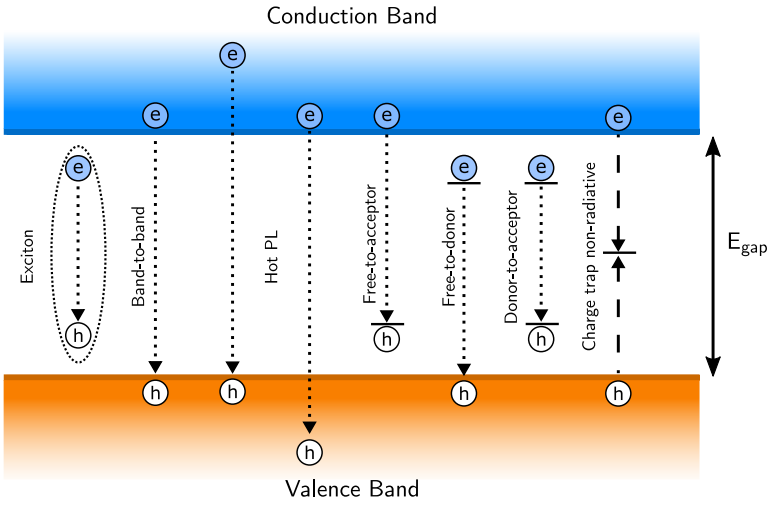

(b)

Figure 3.2: (a) A representative optical absorption spectra for an ideal 2D semiconductor illustrating the exciton states (n), binding energy for the ground state and the difference between optical and electronic band gaps; adapted from [57]. (b) Possible recombination routes for electrons and holes in a semiconducting material. The first four are intrinsic whilst the latter four are due to impurities or defects. Note that the exciton is a two-particle state and thus its energy levels are not formally represented in this one-particle picture. Here, the exciton is illustrated alongside other routes as having an energy transition lower than the band-to-band as is commonly observed.

corresponds to a greater formation of exciton states (or of whichever state is causing the observed PL peak) and PL intensity. Thus, PLE may give an indication of the absorption of a material, often described as pseudo-absorption. [140]

3.1.1 Experimental Implementation

Experimentally, PL spectroscopy may be achieved in many ways. The typical method used here and generally in other 2D material characterisation is demonstrated in Fig. 3.3. This technique works in a reflection mode, with the photoluminescence passing back through the objective lens. Typically, a lens with a magnification of 100x and the highest numerical aperture possible ($\sim$0.9) is used in order to obtain a small excitation spot size (usually $\leq$1 µm) as well as to maximise the collection of PL light. A smaller spot allows for greater accuracy in the probing of the 2D material, which can be sometimes have a small lateral size ($\sim$5 µm), as well as for higher resolution spatial PL maps. The spot size may also be reduced by using a beam expander in the laser beam path. This will expand the laser beam diameter as well as reduce its divergence (or in reverse it may shrink the beam and increase its divergence). The divergence and size of the beam may then be adjusted to match that required by the objective lens for the narrowest focus. Additionally, one may use a pinhole positioned at the focal plane within the beam expander to rid the beam profile of surrounding Airy rings, leaving only a Gaussian beam; a technique known as spatial filtering. Alternatively, one may use optical, single-mode fibres to form cleaner Gaussian beams.

To separate the excitation laser line from the emitted PL, one may use either beamsplitters or dichroic mirrors. Beamsplitters will, generally speaking, split the light into a certain ratio of reflected and transmitted beams. Dichroic mirrors, however, will split the incident light according to its wavelength, with certain wavelengths reflected and others transmitted. The latter allows for a greater percentage of light to be transmitted into the spectrometer, enabling dimmer PL to be captured. The PL sent into the spectrometer is diffracted by a grating into a spectrum of light wavelengths that are then captured by a charge-couple device. The PL setup may also be integrated with a motorised optical microscope for further capability and ease of use. For example, by placing two removable beamsplitters (via motors) in the beam path, one may also be able to shine white light onto the sample and observe it with a camera, which is also useful for laser focussing; see Fig. 3.3. This measurement technique may also be integrated with a closed-cycle or a continuous-flow cryostat for LT ($\sim$4K) PL experiments. These cryostat types have different advantages and limitations that must be taken into consideration for PL measurements.

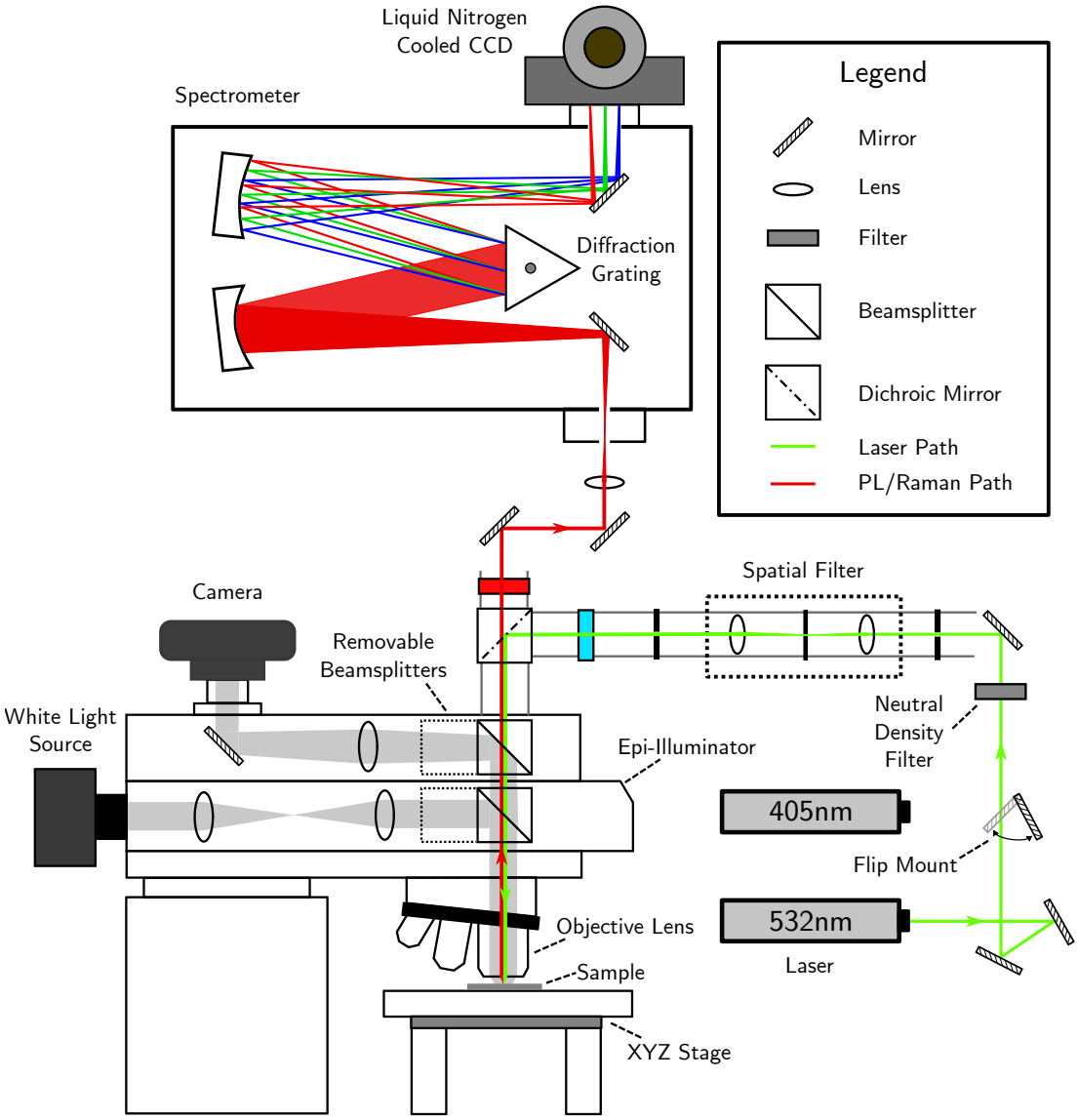

Figure 3.3: Schematic demonstrating the typical experimental setup for PL and Raman spectroscopy measurements.

The techniques used for PLE experiments are largely the same as for PL with some extra requirements. Firstly, in order to vary the wavelength of light incident on the sample, one must use a tunable laser instead of a fixed wavelength laser line. Also, in order to keep the excitation intensity the same over the wide range of wavelengths, a laser power controller is used. This utilises a variable attenuator alongside a feedback mechanism to adjust the intensity accordingly.

3.2 Raman Spectroscopy

Raman spectroscopy is an important optical characterisation technique that utilises the phenomenon of Raman scattering - a process in which incident photons are inelastically scattered by a material due to an interaction with *optical* lattice vibration quasiparticles; usually phonons. Inelastic scattering may also occur due to *acoustic* phonons in a similar process known as Brillouin scattering. Acoustic and optical phonons are lattice vibration quasiparticles in which neighbouring atoms move in- and out-of-phase, respectively. The former of these phonon types generally has a significantly lower energy than the latter in semiconductors. In both inelastic scattering mechanisms, a phonon may be created or annihilated, causing an effective shift in energy of the incident photon. For the creation (annihilation) of a phonon, the scattered photon energy is shifted down (up) in energy; referred to as Stokes (anti-Stokes) shift. The microscopic scattering mechanism involves interactions with intermediary electrons. These allow for a stronger, indirect interaction between the photons and phonons [140]. As Raman scattering is determined by lattice vibrations it is a powerful optical, non-invasive characterisation tool for identifying a crystal lattice and its characteristics.

For a material in which a plane light wave with an oscillating electric field $\underline{E} = \underline{E}_0 \cos(\underline{k}_\gamma \cdot \underline{r} - \omega_\gamma t)$ is incident on it, a polarisation $\underline{P}$ may be induced with an amplitude dependent on its electric susceptibility tensor $\chi_{ij}^{(1)}$ such that [142]

$$P_i = \epsilon_0 \sum_j \chi_{ij}^{(1)} E_j \tag{3.1}$$

By taking a Taylor series expansion of the polarisation about the zero electric field, higher order terms may be obtained [143]

$$\begin{aligned} P_i = P_i|_{E=0} + \sum_j \left.\frac{\partial P_i}{\partial E_j}\right|_{E=0} E_j + \sum_{j,k} \frac{1}{2} \left.\frac{\partial^2 P_i}{\partial E_j \partial E_k}\right|_{E=0} E_j E_k \\ + \sum_{j,k,l} \frac{1}{6} \left.\frac{\partial^3 P_i}{\partial E_j \partial E_k \partial E_l}\right|_{E=0} E_j E_k E_l + ... \end{aligned} \tag{3.2}$$

Which may be otherwise written as [142]

$$P_i = P_{i_0} + \epsilon_0 \Big(\sum_j \chi_{ij}^{(1)} E_j + \sum_{j,k} \chi_{ijk}^{(2)} E_j E_k + \sum_{j,k,l} \chi_{ijkl}^{(3)} E_j E_k E_l + ... \Big) \tag{3.3}$$

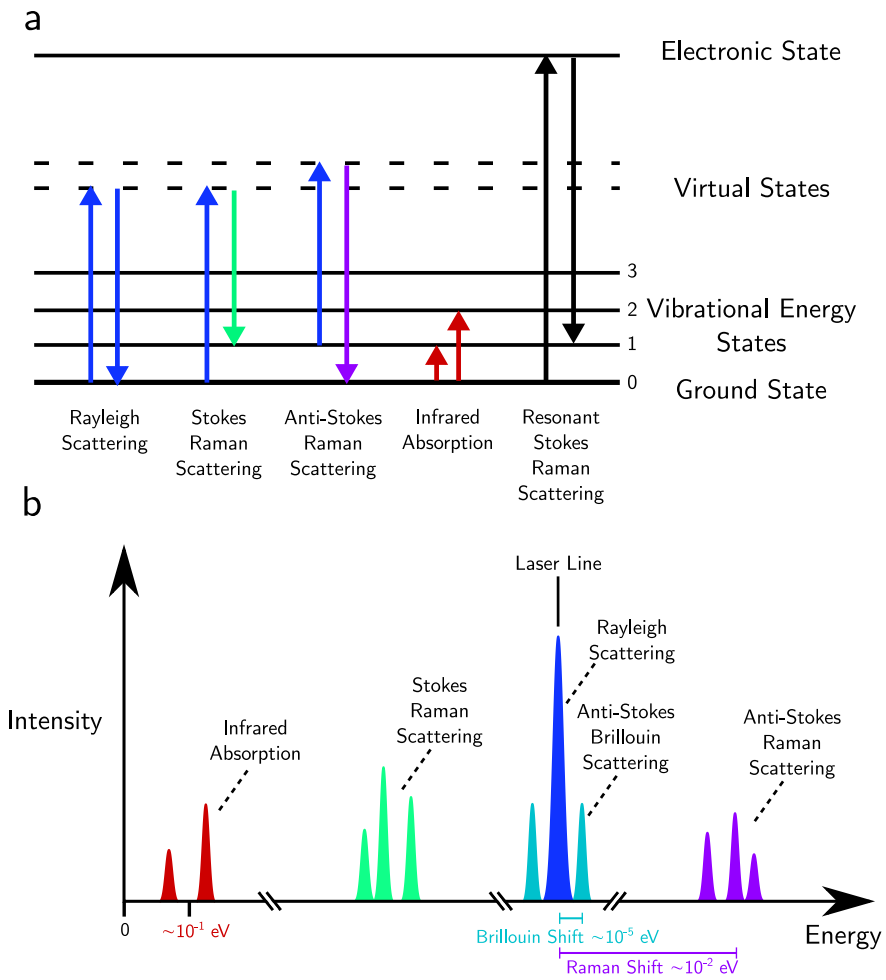

Figure 3.4: Schematic demonstrating (a) the transitions involved in the possible scattering and absorption processes of the vibrational energy states as well as (b) the respective spectra of such transitions that occur at various typical energies.

Here, P_{i_0} comprises the static dipole contribution and $\chi^{(2)}_{ijk}$ and $\chi^{(3)}_{ijkl}$ are the second and third-order susceptibilities defined as third and fourth-rank tensors, respectively. The electric susceptibilities may also be modified by lattice vibrations, or phonons, that displace atomic positions Q as a wave; so that $\underline{Q} = \underline{Q}_0 \cos(\underline{q}\cdot\underline{r} - \omega_q t)$. As these displacements are smaller than the lattice constant, one can express the polarisation as another Taylor series expansion with respect to the displacements such that [140, 144]

$$P_i = P_{i_0}|_{Q=0} + \epsilon_0 \sum_j \chi^{(1)}_{ij} E_j \Big|_{Q=0} + \sum_n \frac{\partial P_{i_0}}{\partial Q_n} Q_n \Big|_{Q=0} + \sum_{j,n} \frac{\partial \chi^{(1)}_{ij}}{\partial Q_n} E_j Q_n \Big|_{Q=0} + \ldots \tag{3.4}$$

Here, the first term indicates the static electric dipole polarisation. The other terms indicate the polarisation variations with the incident light and are written out as follows

$$\begin{aligned} P_i &= \epsilon_0 \sum_j \chi_{ij}^{(1)} E_{j_0} \cos(\underline{k}_\gamma \cdot \underline{r} - \omega_\gamma t) + \sum_n \frac{\partial P_{i_0}}{\partial Q_n} Q_{n_0} \cos(\underline{q}_n \cdot \underline{r} - \omega_{q_n} t) \\ &\quad + \sum_{j,n} \frac{\partial \chi_{ij}^{(1)}}{\partial Q_n} E_{j_0} \cos(\underline{k}_\gamma \cdot \underline{r} - \omega_\gamma t) Q_{n_0} \cos(\underline{q}_n \cdot \underline{r} - \omega_{q_n} t) \\ &= \epsilon_0 \sum_j \chi_{ij}^{(1)} E_{j_0} \cos(\underline{k}_\gamma \cdot \underline{r} - \omega_\gamma t) + \sum_n \frac{\partial P_{i_0}}{\partial Q_n} Q_{n_0} \cos(\underline{q}_n \cdot \underline{r} - \omega_{q_n} t) \\ &\quad + \sum_{j,n} \frac{\partial \chi_{ij}^{(1)}}{\partial Q_n} Q_{n_0} E_{j_0} \Big(\cos\left((\underline{k}_\gamma + \underline{q}_n) \cdot \underline{r} - (\omega_\gamma + \omega_{q_n})t\right) \\ &\qquad\qquad + \cos\left((\underline{k}_\gamma - \underline{q}_n) \cdot \underline{r} - (\omega_\gamma - \omega_{q_n})t\right) \Big) \end{aligned} \tag{3.5}$$

This equation gives four terms. The first demonstrates that the polarisation induced in the material will include a wave with the same wave-vector and frequency as the incident light wave (leading to elastic Rayleigh scattering). The second illustrates an induced polarisation that oscillates with a frequency equal that of a phonon mode. This term describes the infrared active modes as those wherein an incident light frequency is resonant with the phonon mode. The latter two terms include a Stokes shifted wave with wave-vector $\underline{k}_s = (\underline{k}_\gamma - \underline{q}_n)$ and frequency $\omega_s = (\omega_\gamma - \omega_{q_n})$ and an anti-Stokes shifted wave with wave-vector $\underline{k}_a = (\underline{k}_\gamma + \underline{q}_n)$ and frequency $\omega_a = (\omega_\gamma + \omega_{q_n})$. These two terms therefore describe the induced polarisations leading to Raman and Brillouin scattering. The transitions and spectra corresponding to infrared absorption and Raman, Brillouin and Rayleigh scattering processes are demonstrated in Fig. 3.4.

A photon with a wavelength in the visible range (e.g. $\lambda = 532$nm) incident on a crystal with a lattice constant a on the order of nm's will have a wave-vector ($k = \frac{2\pi}{\lambda}$) around 2 orders of magnitude smaller than the BZ edge ($k = \frac{\pi}{a}$). Thus, if the scattered photon has a similar wave-vector, phonons involved in a Stokes or an anti-Stokes shift will also have a relatively small wave-vector near the BZ centre. Hence, single-phonon Raman spectroscopy is commonly suggested to examine Γ point phonons. [140, 144]

The Raman scattered light intensity I_R, of polarisation $\hat{\underline{e}}_R$, is proportional to the induced dipole moment (polarisation) $\underline{P}_{ind}$ created by the incident light with

polarisation $\underline{\hat{e}}_i$ as [140]

$$I_R \propto | \, \underline{\hat{e}}_R \cdot \underline{P}_{ind} \, |^2 \propto | \, \underline{\hat{e}}_R \cdot \frac{\partial \chi}{\partial \underline{Q}}^{(1)} \underline{Q}_0 \cdot \underline{\hat{e}}_i \, |^2 \tag{3.6}$$

Here, the induced dipole moment is taken from the fourth term in Eq. 3.5 with a change in notation as $\underline{P}_{ind} = \underline{\underline{\chi}} \cdot \underline{E} = \frac{\partial \chi}{\partial \underline{Q}}^{(1)} \underline{Q}_0 \cdot \underline{E}$; where $\underline{E} = E\underline{\hat{e}}_i$. Equation 3.6 can be obtained by considering the scattered radiation energy cross section from an electric dipole moment oscillating with the shifted frequency; see Ref. [145] and [146] for further details. From this, a second rank Raman tensor is defined as $\underline{\underline{R}} = \frac{\partial \chi}{\partial \underline{Q}}^{(1)} \underline{Q}_0$. A Raman scattering process is active if the Raman tensor elements for given incident and scattered light polarisations are not equal to zero. As the wave-vectors of phonon modes for Raman scattering are around the BZ centre, the symmetries of the phonons at the Γ point are considered. These symmetries are the same as the point-group of the crystal [140]. By knowing the point-group and, thus, the symmetries (e.g. given by operations S) of a crystal one can simplify the Raman tensors for each of its characteristic phonon modes; i.e. by using $\underline{\underline{R}}' = S\underline{\underline{R}}S^{-1} = \underline{\underline{R}}$. The phonon modes are also given by an 'irreducible representation' of the symmetries attributed to that point-group. By analysing the simplified Raman tensors for different incident $(\underline{k}_i, \underline{\hat{e}}_i)$ and scattered $(\underline{k}_s, \underline{\hat{e}}_s)$ photon configurations (given by the Porto notation $\underline{k}_i(\underline{\hat{e}}_i, \underline{\hat{e}}_s)\underline{k}_s$), one may also obtain Raman selection rules for co-polarised or cross-polarised regimes. For example, in a backscattering setup, such that the incident and scattered photons propagate in opposite directions along the z-axis, it is possible to find that $z(x,x)\bar{z}$ or $z(y,y)\bar{z}$ are active but that $z(x,y)\bar{z}$ or $z(y,x)\bar{z}$ are inactive. [140]

As well as probing a crystal lattice, resonance Raman spectroscopy may also be used for studying interband and excitonic transitions in semiconductors. Upon tuning the incident photon energy to resonate with an interband transition or excitonic state, one may obtain a Raman scattering intensity that is orders of magnitude larger than for the non-resonant condition. This is suggested to be due to the increased probability of interactions with intermediary electrons or excitons [140].

Experimentally, Raman spectroscopy is performed through similar experimental techniques as for PL spectroscopy. In fact, if the conditions are right, it is possible to obtain both in the same measurement. However, small considerations may be helpful. Firstly, the use of a higher grating density in the spectrometer is

beneficial for an increased wavelength resolution. This will, however, decrease the intensity binned per pixel and therefore require either longer exposure times or higher laser powers for a similar Raman intensity. Additionally, the use of filters with edges a few cm^{-1} close to the incident laser line are important as otherwise Raman spectral lines may be blocked. For measurements of low wavenumber Raman modes such as shear or breathing modes, multiple diffraction gratings may be used to disperse the spectra further, with a thin material then accurately positioned to block the laser fundamental in real space instead of a filter.

3.3 Second Harmonic Generation

The observation of nonlinear optical processes is increasingly important in 2D material characterisation. As with Raman spectroscopy, these nonlinear optical processes are sensitive to the symmetries present in the material. However, instead of probing phonon modes, nonlinear optical measurements may be used to investigate the crystal symmetries directly. Moreover, crystallographic orientations as well as doping, strain, surfaces and other parameters that affect symmetry may be probed [147]. Here, a particular nonlinear optical measurement, second harmonic generation, is summarised for the case of obtaining the crystallographic orientation of a 2D material.

Second harmonic generation (SHG) is a nonlinear optical process that describes the condition in which a material may emit light with a frequency double (2ω) that of the light that is incident on it (ω); see Fig. 3.5. This SHG is only observed in materials which are not centrosymmetric (i.e. no point in the unit cell has inversion symmetry) [148].

As the name implies, nonlinear optical processes are those associated with a nonlinear response of the polarisation induced in a material by an electric field. For linear optics, the polarisation induced in a material, with linear susceptibility $\chi^{(1)}$, is linearly dependent on the electric field as given by Eq. 3.1. As demonstrated in the previous section, this may be expanded to include higher order terms; see Eq. 3.3. This series expansion is valid for electric fields significantly smaller than the characteristic atomic electric field strength $E_{at} = e/(4\pi\epsilon_0 a_0^2) \simeq 5 \times 10^{11} \mathrm{Vm}^{-1}$; $E \ll E_{at}$ [143, 148]. The second and third-order nonlinear terms determine physically distinct optical interactions, with the former giving rise to SHG (amongst other phenomena) and the latter to third-harmonic

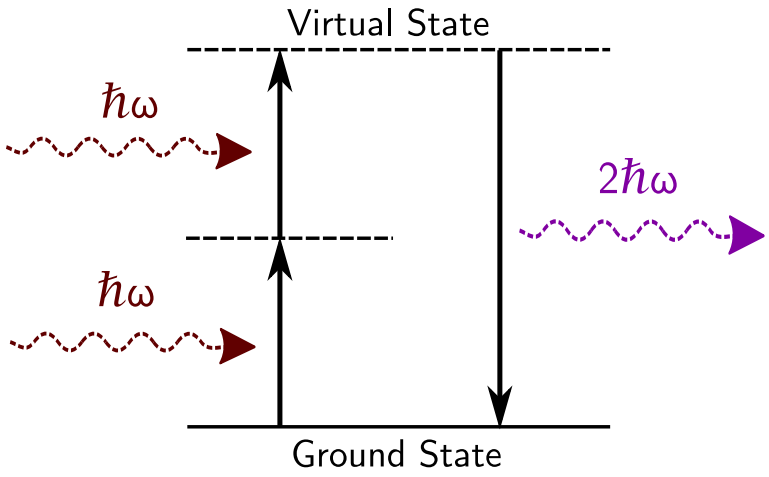

Figure 3.5: Schematic energy level diagram of the SHG process.

generation. The second-order term also demonstrates why SHG only occurs in non-centrosymmetric crystals. If a material has inversion symmetry, these polarisation terms must also be similarly symmetric. If one inverts the polarisation and each electric field component they will each change sign. However, the product of the electric field for the second-order term remains unchanged. Thus, for inversion symmetry to hold, the $\chi^{(2)}_{ijk}$ term must be zero and therefore no SHG occurs. [142]

To begin describing SHG mathematically, the second-order nonlinear term may be given as a function of the angular frequency ω using a Fourier transform. Then it can be shown that two collinear light plane waves of angular frequency ω form a polarisation at 2ω in a given crystal such that [148]

$$P_i(2\omega) = \frac{1}{2}\epsilon_0 \sum_{j,k} \chi^{(2)}_{ijk}(2\omega;\omega,\omega)E_j(\omega)E_k(\omega) \tag{3.7}$$

The second-order susceptibility tensor (of third-rank) may be simplified due to intrinsic permutation symmetry which states that $\chi^{(2)}_{ijk} = \chi^{(2)}_{ikj}$. This is due to that fact that some terms included in the summation must be equal; i.e. $\chi^{(2)}_{ijk}E_j(\omega_n)E_k(\omega_m) = \chi^{(2)}_{ikj}E_k(\omega_m)E_j(\omega_n)$. From this, a new second-order susceptibility tensor may be defined $\chi^{(2)}_{ijk} = 2d_{ijk} = d_{np}$ such that $i = n$ and $jk = p$; see Table 3.1.

(a)

i	x	y	z
n	1	2	3

(b)

jk	xx	yy	zz	yz, zy	xz, zx	xy, yx
p	1	2	3	4	5	6

Table 3.1: Equivalent values for χ_{ijk} and d_{np}

The full expression for the polarisation vector P_i is then given by [148]

$$\begin{pmatrix} P_x \\ P_y \\ P_z \end{pmatrix} = \epsilon_0 \begin{pmatrix} d_{11} & d_{12} & d_{13} & d_{14} & d_{15} & d_{16} \\ d_{21} & d_{22} & d_{23} & d_{24} & d_{25} & d_{26} \\ d_{31} & d_{32} & d_{33} & d_{34} & d_{35} & d_{36} \end{pmatrix} \begin{pmatrix} E_x^2 \\ E_y^2 \\ E_z^2 \\ 2E_yE_z \\ 2E_zE_x \\ 2E_xE_y \end{pmatrix} \tag{3.8}$$

In the experiments conducted in this work, the crystals under investigation are atomically thin semiconductors encapsulated in other insulating crystals (hBN). It is reasonable to model this situation with a thin polarisable sheet at the interface of two dielectric medium; see Fig 3.6. This may also be reasonable for non-encapsulated crystals that are adjacent to dielectric media.

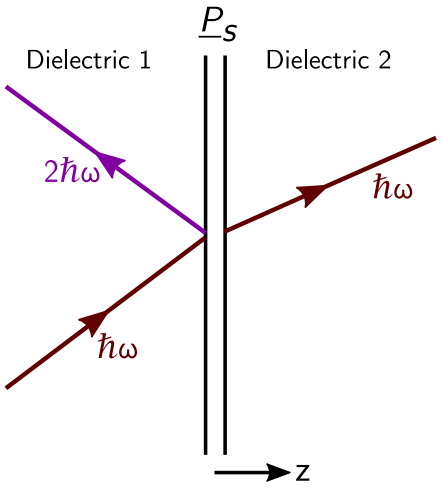

Figure 3.6: Schematic of SHG reflected from a thin polarisable sheet $\underline{P}_s$ between two dielectric medium; adapted from [149].

In this situation, the boundary conditions across the thin polarisable sheet may be derived from Maxwell's equations for a non-magnetic material with some nonlinear polarisation such that (see Ref. [149, 150] for further details)

$$\underline{\nabla} \cdot \underline{D} = -4\pi \underline{\nabla} \cdot \underline{P}_{NL} \tag{3.9a}$$

$$\underline{\nabla} \times \underline{E} = -\frac{1}{c}\frac{\partial \underline{B}}{\partial t} \tag{3.9b}$$

$$\underline{\nabla} \cdot \underline{B} = 0 \tag{3.9c}$$

$$\underline{\nabla} \times \underline{H} = \frac{1}{c}\Big(4\pi \frac{\partial \underline{P}_{NL}}{\partial t} + \frac{\partial \underline{D}}{\partial t}\Big) \tag{3.9d}$$

With this one can find the boundary conditions on a thin polarisable sheet and then obtain the electric field of the second harmonic radiation $\underline{E}_i^{SH}(2\omega)$ induced in medium i by a sheet with polarisation $\underline{P}_s(2\omega)$ [150]

$$\underline{\hat{e}}_i \cdot \underline{E}_i^{SH}(2\omega) = \frac{2\pi i K^2}{q_i}(\underline{\hat{e}}_i \cdot \underline{P}_s(2\omega)) \tag{3.10}$$

Here, $\underline{\hat{e}}_i$, q_i and K are the SHG polarisation vector (such that $\underline{\hat{k}}_i \cdot \underline{\hat{e}}_i = 0$), wave vector z-component and wave vector in free space (such that $K = 2\omega/c$), respectively [150].

At this stage the crystal symmetry of the material is important in providing the angular dependence of the SHG electric field. For 2D materials such as MoS_2 and hBN, the point-group they belong to depends on their thickness. For even numbers of layers, they belong to the centrosymmetric D_{3d} point-group (resulting in no SHG for light incident along the z-axis) whilst in odd numbers of layers they belong to the non-centrosymmetric D_{3h} point-group [151]. Monolayers of InSe and GaSe also belong to the D_{3h} point-group. In their bulk form, they may exist as different polytypes but are usually found as γ- and ϵ- types, respectively; see Ch. 1. The ϵ-polytype retains D_{3h} point-group symmetries [152, 153]. However, the γ-polytype has C_{3v} point-group symmetry [98]. Both of these point-groups form second-order susceptibility tensors with a similar dependence on the electric fields in the x and y axes. Thus, if the light is incident on the crystal along the z-axis, the same resultant polarisation dependencies form [154, 155]. The D_{3h} point-group contains non-zero second-order susceptibility tensor elements $\chi^{(2)}_{xxx} = -\chi^{(2)}_{xyy} = -\chi^{(2)}_{yyx} = -\chi^{(2)}_{yxy}$ or $d_{11} = -d_{12} = -d_{26}$ with the x-axis along the armchair direction (see Fig. 1.4a) for PTMCs and TMDCs [154, 156, 157].

If the laser is incident on the crystal parallel to the z-axis (defined as the normal to the crystal cleavage plane), with an electric field defined as $\underline{E}^i = E_0(\cos\theta, \sin\theta, 0)$, then Eq. 3.8 gives

$$\begin{pmatrix} P_x \\ P_y \\ P_z \end{pmatrix} = \epsilon_0 \begin{pmatrix} d_{11}E_0^2 \cos 2\theta \\ -d_{11}E_0^2 \sin 2\theta \\ 0 \end{pmatrix} \tag{3.11}$$

From this, the components for the SHG electric field ($\underline{E}^{SH}$) in x, y and z are obtained from Eq. 3.10; given straightforwardly as [155]

$$\begin{pmatrix} E_x^{SH} \\ E_y^{SH} \\ E_z^{SH} \end{pmatrix} = A \begin{pmatrix} \cos 2\theta \\ -\sin 2\theta \\ 0 \end{pmatrix} \tag{3.12}$$

Where A is a pre-factor independent of θ. The electric field of the SHG that is projected parallel ($E_\parallel$) to the incident laser electric field ($\underline{E}^i$) is found using standard vector projection of the SHG electric field ($\underline{E}^{SH}$), given by $E_\parallel = \frac{\underline{E}^{SH} \cdot \underline{E}^i}{|\underline{E}^i|^2} \underline{E}^i$. A similar equation may also be used to find the SHG electric field that is projection perpendicular ($E_\perp$) to the incident laser electric field. Together these projections are given as [155]

$$E_\parallel = C \cos 3\theta \tag{3.13a}$$

$$E_\perp = -C \sin 3\theta \tag{3.13b}$$

Where C is a pre-factor independent of θ. The intensity of an electric field is proportional to its square, giving the final result that

$$I_\parallel \propto \cos^2 3\theta \tag{3.14a}$$

$$I_\perp \propto \sin^2 3\theta \tag{3.14b}$$

This SHG intensity dependence on incident laser polarisation angle θ is a crucial result that outlines a crystal's symmetry with, in the case of the parallel arrangement, the maximum intensity occurring when the laser polarisation is parallel to the armchair axis. Interestingly, the total SHG intensity is independent of the incident polarisation and thus probing the resultant SHG polarisation is pivotal. This technique can therefore be used to determine the relative twist angles

between crystals non-invasively.

3.3.1 Experimental Implementation

Second harmonic generation measurements on 2D materials may be achieved using much of the same techniques as described for PL spectroscopy. A typical optical setup for SHG measurements is shown in Fig. 3.7. Pulsed lasers are used for nonlinear optical experiments as they provide the high peak intensities required whilst maintaining lower average powers to reduce sample heating. This is especially important for thin 2D materials that may burn at high laser powers. A workable option has been found to use a 785nm laser with 80fs pulses (repetition rate of 80MHz) at an average power of 1mW/μm^2 . This laser light may also be focussed with a higher magnification and numerical aperture objective lens. The laser light and SHG signal may be split by a short-pass dichroic mirror. Linear polarisers are placed immediately before and after the dichroic mirror in order to achieve either co- or cross-polarised measurement regimes. Between the dichroic mirror and the objective lens, a half-wave plate is positioned. This is pivotal for ensuring that the incident and SHG light are co- or cross-polarised for all polarisation angles. The half-wave plate introduces a π phase shift in linearly polarised light such that it's polarisation flips across the plate's fast axis. This enables variation of the incident polarisation angle (without affecting incident light intensity) by rotation of the wave plate; thus allowing for polarisation-resolved SHG measurements.

3.4 Reflectance Contrast

Obtaining absorption spectra of a material is a standard method for probing its optical properties, providing information on various important aspects. For quantum wells, this can examine exciton states, the band gap and higher energy states due to the unique structure of its density of states [139, 158]. Similar absorption characteristics are expected for atomically thin 2D materials. However, as 2D materials are typically placed on opaque substrates, obtaining absorption spectra through transmission is not possible. As an alternative approach, differential reflection spectroscopy (also known as reflectance contrast) is employed. This technique functions by obtaining the reflectance spectra of a 2D material crystal on a substrate R as well as the reflectance of just the substrate R_0 and

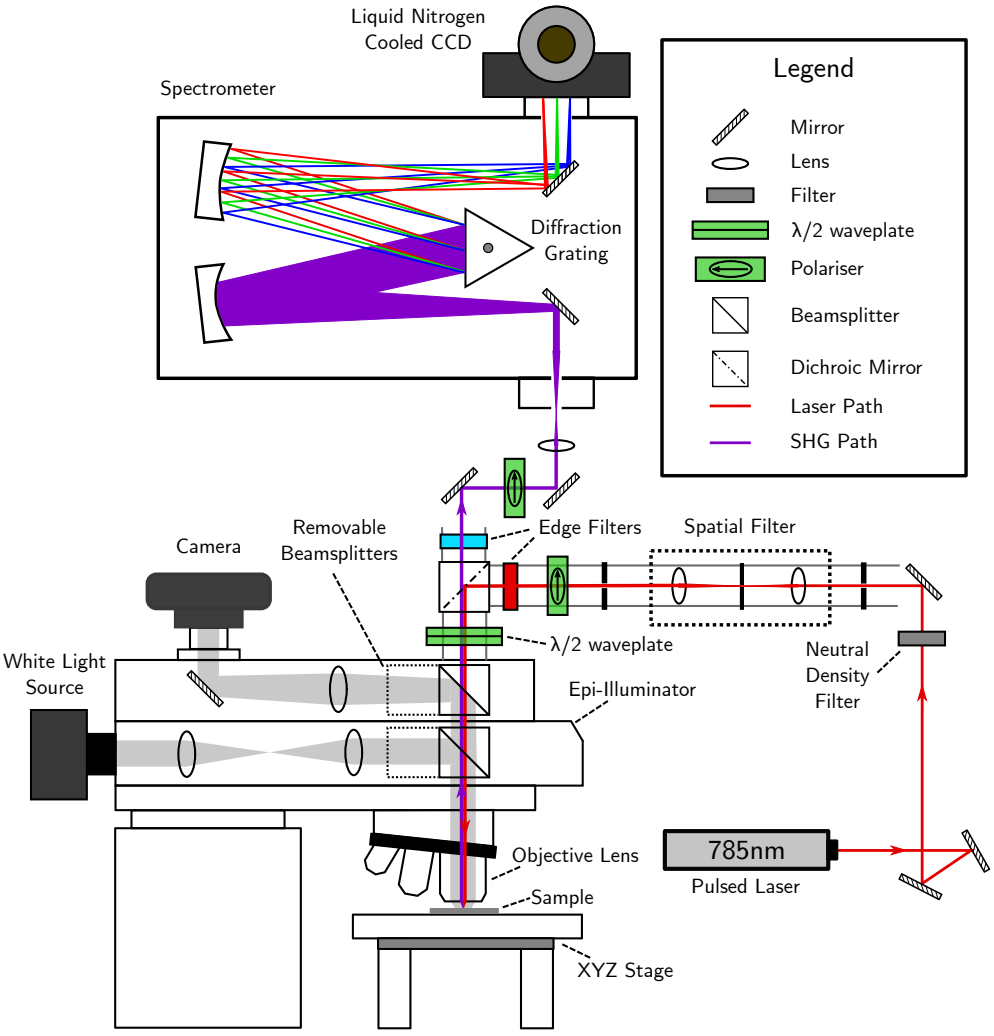

Figure 3.7: Schematic demonstrating the typical experimental setup for SHG spectroscopy measurements.

then obtaining the contrast between the two. This contrast is then proportional to the absorption spectrum of the crystal α as [159, 160]

$$\frac{R - R_0}{R_0} = \frac{4n}{n_0^2 - 1}\alpha \tag{3.15}$$

Here, n and n_0 are the refractive indices of the crystal and substrate, respectively. Experimentally, reflectance may be measured simply by focussing a broadband white light source onto a small area of the crystal and then the substrate. From this, the left side of Eq. 3.15 may be obtained. As this is a differential reflectance, high gradient points in the spectrum infer absorption lines.

3.5 Ultra-high Vacuum Integration

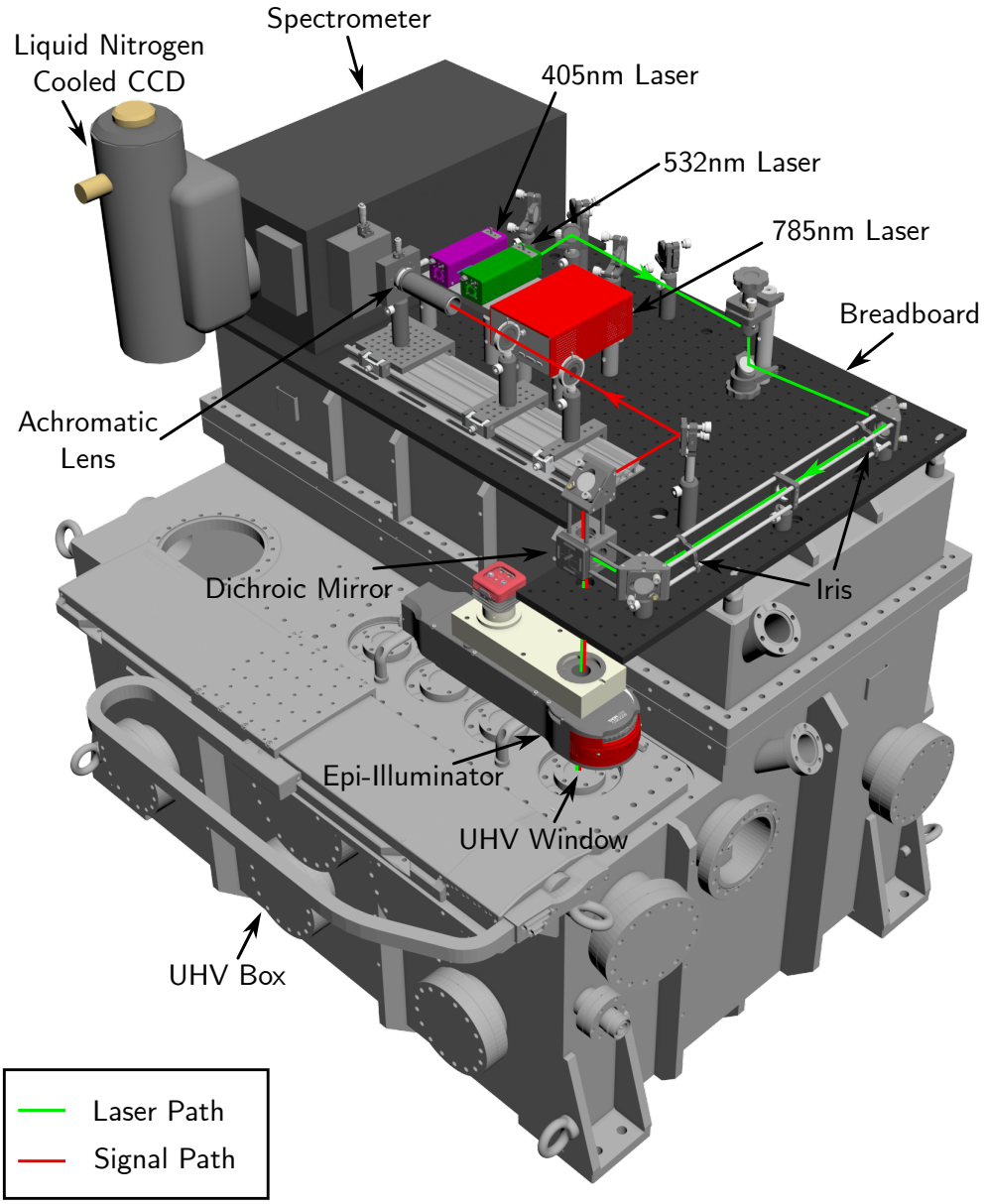

Figure 3.8: Schematic of a custom optical setup integrated into an ultra-high vacuum system.

The optical characterisation of air-sensitive 2D materials may be achieved through hBN encapsulation, as outlined in Ch. 2. However, as part of an effort to study these materials in a cleaner environment, the optical measurements described in the previous sections were also integrated into an ultra-high vacuum (UHV) system. This system is illustrated in Fig. 3.8. Inside the UHV 'box'

is a micromanipulation arm with five degrees of freedom as well as a sample stage, similar to the transfer systems described earlier. Four objective lenses (5x, 10x, 50x and 100x) are adjacent to one another in fixed positions; see Fig. 2.12. Above and below these lenses are deployed an optical train and transfer stage, respectively, which may reposition in sync at a certain objective lens. The optical train includes an epi-illuminator that is standard for optical microscopy, allowing for bright-field imaging. The optical characterisation setup is established for the 100x objective lens only. Above the 'box' a breadboard is positioned that allows for optical components to be fixed upon it. On this breadboard, the configurations for each optical characterisation technique are prepared; see Fig. 3.8. Here, three lasers (532nm and 405nm continuous-wave and a 785nm pulsed) may be selected through the use of flip mounts. Each laser is made collinear through the use of mirrors and fixed irises as targets. The different filters (edge and dichroic mirrors for each experiment) may be selected by simple replacement of a cube fixture; minimising realignment requirements. A motorised rotation stage containing a half-wave plate may also be positioned between the epi-illuminator and objective lens window for high resolution polarisation-resolved SHG measurements. Altogether, this enables straightforward switching between optical experiments, allowing for robust characterisation of 2D materials held within the UHV system.

3.6 Summary

In this chapter, optical techniques used for characterising 2D materials were discussed. Initially, photoluminescence and its usefulness in gauging band gap energies in semiconductors was introduced alongside experimental methods for implementing such measurements. Then, an introduction to Raman spectroscopy was given, demonstrating its utilisation in probing crystal symmetries. Afterwards, a nonlinear optical technique for probing crystallographic axes by second-harmonic generation was presented. The technique of reflectance contrast for studying the absorption properties of crystals on opaque substrates was also examined. Lastly, work undertaken to implement these optical techniques into an UHV system for improved studies on air-sensitive materials was discussed.

Chapter 4

Optical Properties of PTMCs

Post-transition metal chalcogenides have been relatively unexplored in their few-layer form, especially in comparison to the intensely researched TMDCs. As suggested in Ch. 2, PTMCs are more sensitive to ambient conditions, with degradation clearly visible over timescales of a few days. As such, experimental techniques to encapsulate them in inert hBN crystals were discussed. In this chapter, optical experiments to non-invasively study the properties of hBN encapsulated few-layer InSe and GaSe are presented. These experiments are a summary of observations from three separate publications [100, 157, 161] as well as one currently under review [162]. All samples were fabricated by myself with the techniques described in Ch. 2. The optical measurements were performed in collaboration with M. Molas and A. Tyurnina for Raman studies, V. Zólyomi for theoretical calculations, J. Zultak and A. Tyurnina for PL studies, N. Leisgang for SHG studies and D. Hopkinson and S. Haigh for STEM studies.

4.1 InSe

4.1.1 Raman Studies

The phonon modes of monolayer InSe are identified by the irreducible representations that characterise the symmetry properties of its point-group, D_{3h}. A summary of the irreducible representations for monolayer InSe and their Raman activity is given in Fig. 4.1. The phonon dispersion curves for monolayer InSe associated with these irreducible representations are also given in Fig. 4.1. The Raman activity and classification of the phonon modes of monolayer InSe is also

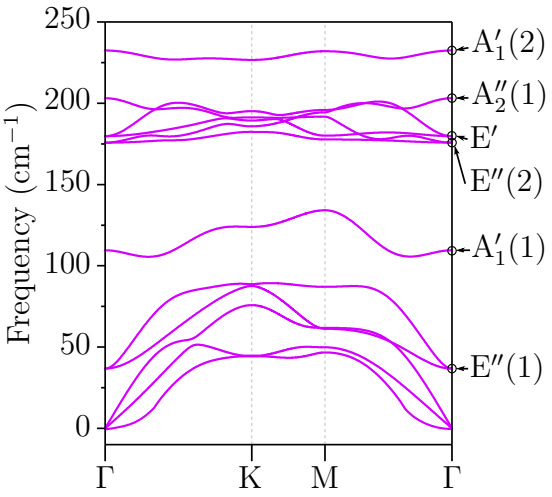

IrrRep	ω^{DFT}	Ratio	ω^{expt}
E″(1)	41.3	1:1	
A$_1'$(1)	110.9	1:0	115
E″(2)	175.0	1:1	178
E′	178.7	1:1	
A$_2''$(1)	206.6	0:0	200
A$_1'$(2)	237.5	1:0	228

Figure 4.1: Phonon dispersion and Raman activity table for monolayer InSe obtained from DFT within the local density approximation (using Quantum Espresso). The flexural acoustic phonon branch (the lowest frequency branch) in the vicinity of the Γ point has numerical issues caused by a small supercell in the calculation and therefore may be ignored. The phonon modes are denoted by the irreducible representations (IrrRep) characteristic of the point-group D_{3h}. The theoretical phonon frequencies ω^{DFT} at the Γ point found using DFT are given alongside the experimentally measured values ω^{expt}. The third column denotes the co-:cross-polarised Raman activity ratio such that 1 means it is active whilst 0 means it is inactive. Adapted from [162], currently under review.

representative of multi-layered InSe crystals as they retain a similar symmetry. For this reason, Raman peaks for all thicknesses are categorised according to these irreducible representations, consistent with previous studies [163, 164].

An example of the Raman spectrum of trilayer InSe encapsulated in hBN is presented in Fig. 4.2. Here, four peaks are observed for the co-polarised, backscattered measurement regime. These peaks represent four phonon modes characteristic of InSe that are similar to those previously observed for bulk InSe [164]. Interestingly, for the cross-polarised measurement regime, the E″(2) remains bright whilst the other peaks associated with out-of-plane vibrations significantly reduce in intensity. This is in line with the selection rules for the different vibrational modes which may be assessed by their respective Raman tensors and the experimental configuration [165]; see Eq. 3.6 and the table in Fig. 4.1. A visual representation of the relative atomic displacements for the four phonon modes are also given in Fig. 4.2. Davydov splitting in the Raman modes was not observable for all measurements taken. Here, all Raman spectra were taken at room temperature with a resolution of ∼2cm^{-1}. This is suggested to

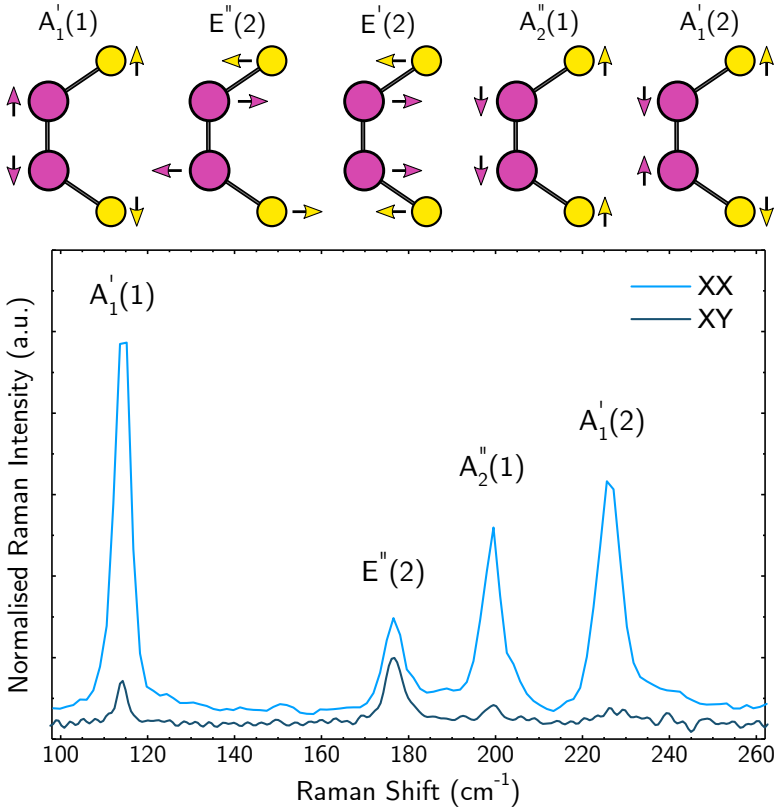

Figure 4.2: Top: Relative displacements of the atoms for the respective phonon modes associated with (bottom) the Raman spectrum for 3L InSe. The co- (XX) and cross-polarised (XY) backscattering measurement regimes, offset for clarity, reveal different spectra for 3L InSe under excitation at 2.54eV. Adapted from [162], currently under review.

leave the Davydov splittings ($\sim$1cm^{-1}) unresolvable, with lower temperatures and higher spectral resolution required to observe them; as was observed previously [166–168].

According to the calculated phonon frequencies, modes representing E″(2) and E′ are predicted to have almost degenerate frequencies and similar activities for monolayer InSe. This is also true for the multi-layered forms. Note that for multi-layered InSe, E′ is denoted as E′(2) as a lower frequency shear mode denoted E′(1) forms. It is therefore difficult to distinguish between E″(2) and E′ (or E′(2)) and here the Raman peak at 178cm^{-1} is tentatively assigned to the E″(2) mode, in accordance with previous studies [163, 169, 170]. The two modes may be better distinguished in an alternative measurement geometry such that the activities of the modes are distinct. Surprisingly the phonon mode $A_2''(1)$ is also clearly observable for thin InSe crystals despite its predicted inactivity.

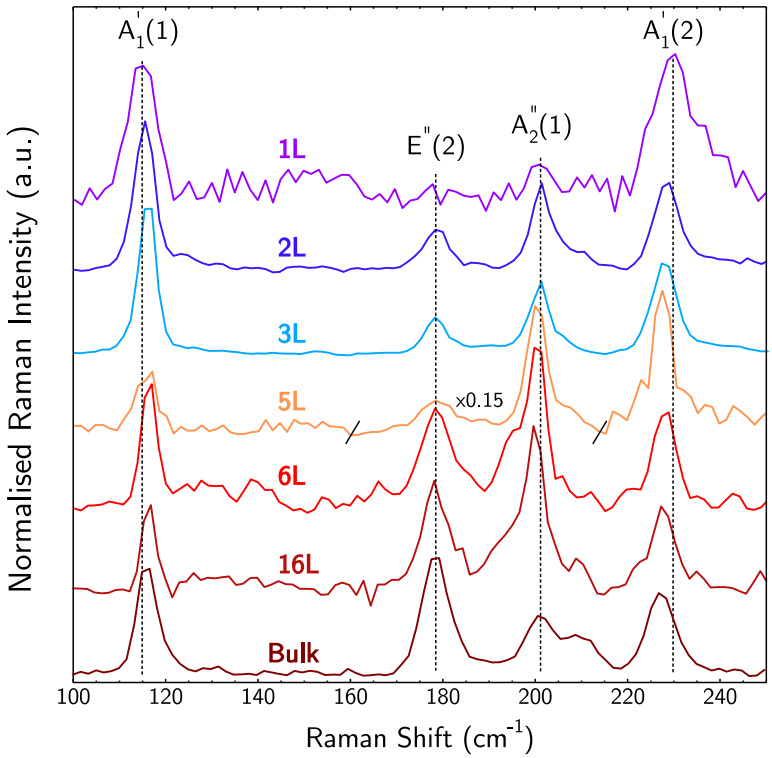

Figure 4.3: Raman spectra for InSe of monolayer to bulk crystal thickness with unpolarised excitation at 2.54eV. The dashed lines denote the peak positions for the monolayer Raman spectrum. The spectra are offset and normalised for clarity. Adapted from [162], currently under review.

Figure 4.3 shows the Raman spectra for various InSe crystal thicknesses from an unpolarised excitation at an energy of 2.54eV (wavelength of 488nm).

Firstly, the Raman spectrum from monolayer and bilayer InSe crystals has been observed. Previous attempts to gauge the Raman spectrum from monolayers and bilayers of InSe have shown low signal-to-noise ratios or only one obvious Raman peak at $\sim$120cm^{-1} [171, 172]. In these studies, no protection was provided for the InSe crystal. Here, the capability to measure the Raman spectra of such crystals is suggested to be due to the improved material quality that protection through hBN encapsulation in an inert environment provides. From Fig. 4.3, it may be observed that the $A_2''(1)$ peak is resonant for intermediate InSe crystal thicknesses. This is suggested to be due to the excitation energy (2.54eV) being in resonance with the higher optical transition (B transition) that is typically observed to be at $\sim$2.4eV for bulk and $\sim$2.9eV for monolayer InSe crystals respectively; see [94] and Fig. 4.6a. The appearance of the $A_2''(1)$ peak was previously only observed in bulk InSe at excitation energies resonant with

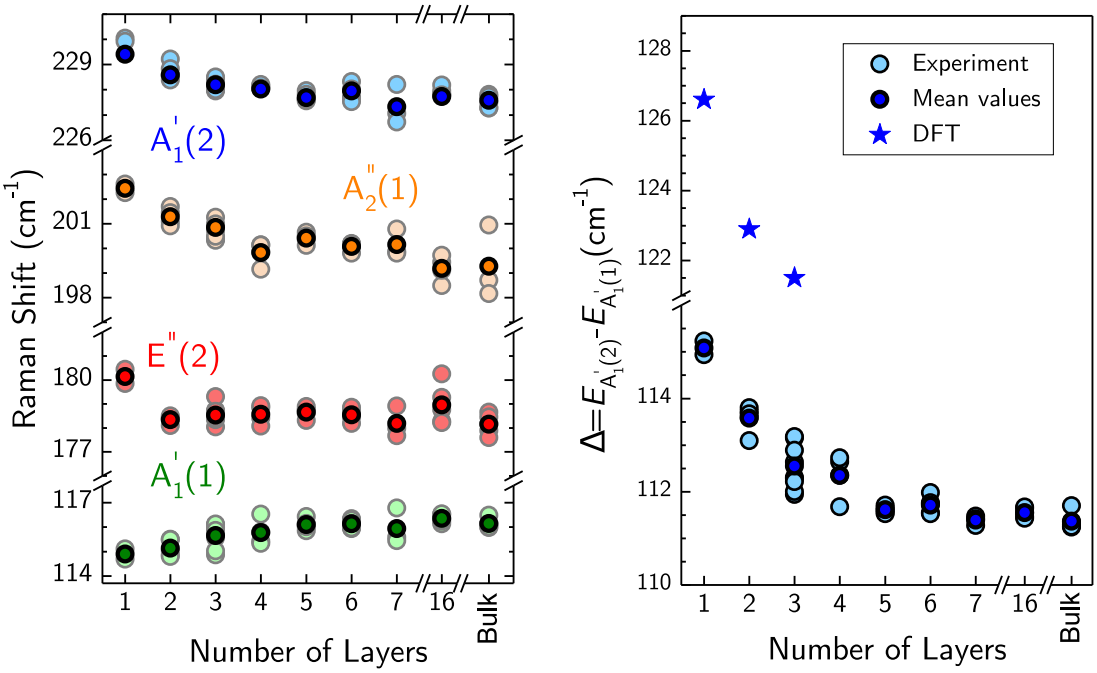

Figure 4.4: Left: A summary of the Raman peak shifts measured for various crystal thicknesses of InSe. Right: The difference of between the A_1 Raman peak shifts (such that $\Delta = A_1'(2) - A_1'(1)$) for the various crystal thicknesses of InSe alongside the DFT predicted differences (star symbols). The darker coloured symbols represent the mean values obtained from the data (lighter coloured symbols); which were measured at excitation energies from 1.96eV to 2.7eV. Adapted from [162], currently under review.

this higher optical transition [164]. A summary of the Raman shifts for various InSe crystal thicknesses is given in Fig. 4.4. As the thickness of InSe is reduced down to monolayer crystals, clear shifts in the Raman spectra are observable. The A_1-type vibrational Raman peaks shift to opposite energies whilst the E-type vibrational peak remains constant. The shifts in the A_1-type peaks are accentuated by the right hand graph of Fig. 4.4 in which the difference Δ between the A_1 peak Raman shifts is given for the various crystal thicknesses, such that $\Delta = A_1'(2) - A_1'(1)$. This quantity demonstrates a similar trend to that predicted from DFT calculations. Also, as the adjustment of Δ is substantial for few-layer crystals, it may be used for few-layer crystal thickness identification.

Lastly, the low frequency Raman modes for thin InSe crystals are investigated. These vibrational modes are associated with the relative displacement of adjacent layers, also known as the shear or breathing modes. Figure 4.5 demonstrates an example of the relative displacements for the shear mode E$'$(1). For

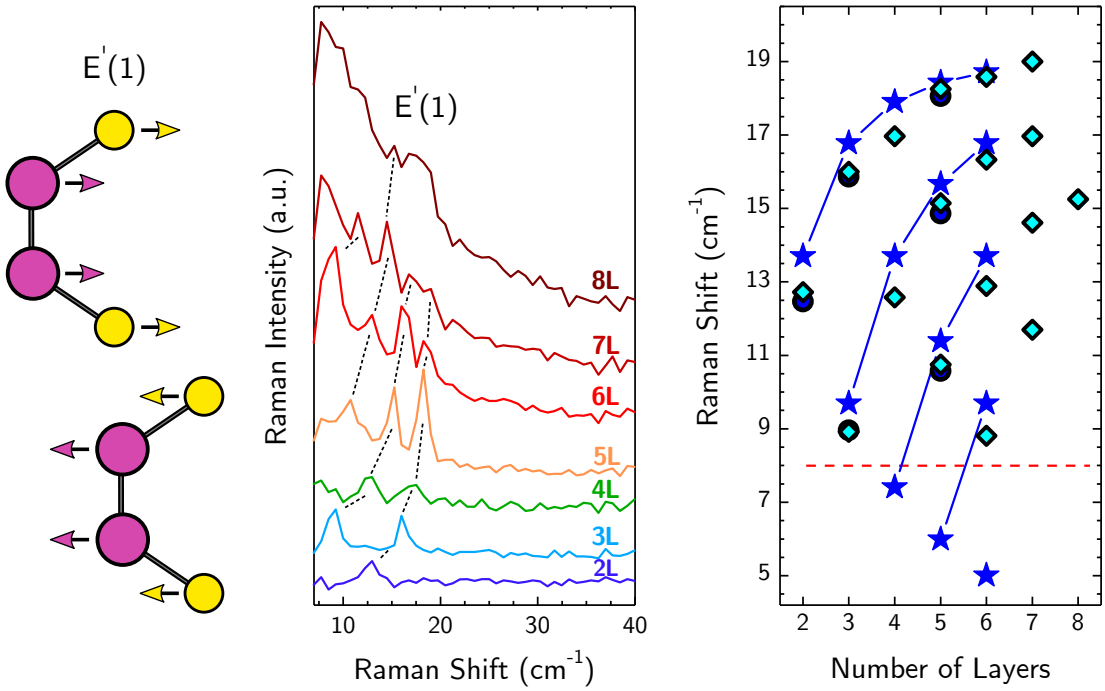

Figure 4.5: Left: Relative displacements of the atoms within a unit cell for the respective phonon shear modes associated with (centre) the low frequency Raman scattering modes for various InSe crystal thicknesses under excitation at 2.41eV. Right: A summary of the measured Raman shear modes (diamond and circle symbols) alongside the predicted values from a linear chain model and DFT calculations (star symbols). The dashed line represents the limit of the measurable spectra. Adapted from [162], currently under review.

these shear modes, adjacent layers vibrate in-plane to one another. For breathing modes, adjacent layer vibrate out-of-plane to one another. These two types of low frequency Raman modes have previously been studied in TMDCs crystals [173]. The number of these interlayer vibrational modes $N-1$ correlates to the number of layers N with monolayers not demonstrating them. As can be seen in Fig. 4.5, the crystal thickness has a systematic effect on the low frequency vibrational modes observable. These are found to closely resemble the expected shear mode frequencies found using a linear chain model and DFT calculations of force constants [174]. Interestingly, the breathing modes, expected at slightly higher frequencies generally (from $\sim$9cm^{-1} to $\sim$33cm^{-1} depending on the thickness), are not observed here. This may be due to their characteristic larger line-width, as previously observed in TMDCs [173].

Overall, the Raman spectra for hBN encapsulated InSe crystals with thicknesses from bulk down to monolayers has been presented. The intralayer and

interlayer vibrational modes for the various crystal thicknesses have been identified alongside theoretical predictions, demonstrating Raman spectroscopy as a technique for the assessment of symmetry and thickness of few-layer crystals.

4.1.2 Photoluminescence Studies

Out-of-plane Incident Excitation

As described in Ch. 3, PL spectroscopy may be used to probe a semiconductor's band gap energy. In the case of 2D materials, the usefulness of this technique is particularly salient. Figure 4.6a illustrates normalised PL spectra for a representative spread of thicknesses of InSe crystals encapsulated in hBN, for incident light directed out of the basal plane. As the thickness of the InSe crystal is decreased from bulk to a monolayer, the PL peak energy is observed to increase from ∼1.3eV to ∼2.9eV. This is similar to previous reports on few-layer InSe [82, 94]. The increase of the PL peak energy is indicative of a widening of the optical band gap of InSe as the number of constituent layers is reduced; in agreement with theoretical predictions [88], as discussed in Ch. 1. Here, Fig. 4.6a demonstrates a collection of normalised PL spectra for InSe of various thicknesses. It is important to note that the absolute intensity of the PL spectra is regularly seen to decrease as the InSe crystal thickness is decreased. This decrease has also been observed previously [82, 94] and is suggested to be due to the increasingly indirect nature of the band minima as the layer number is decreased. This is also discussed in Ch. 1. Interestingly, prior studies of PL in few-layer InSe reported maximum PL peak energies of ∼1.45eV [82, 132, 133]. It is suggested that this was observed because the InSe was not protected through hBN encapsulation, thus the thinnest layers may have remained inaccessible due to degradation; see Ch. 2.

The PL spectra obtained for energies below 2eV were taken using an excitation wavelength of 532nm. The observation of higher energy PL (B-transition) from monolayer and bulk InSe was achieved by excitation from higher energy lasers; 325nm and 457nm respectively. The intensity of these peaks is observed to be reduced in comparison to those of the lower energy peaks (note that here they are normalised due to sample variation). In the case of the monolayer crystal, this continues the trend observed due to the increasingly indirect nature of the band gap. For bulk InSe, this higher energy peak is due to a hot PL process

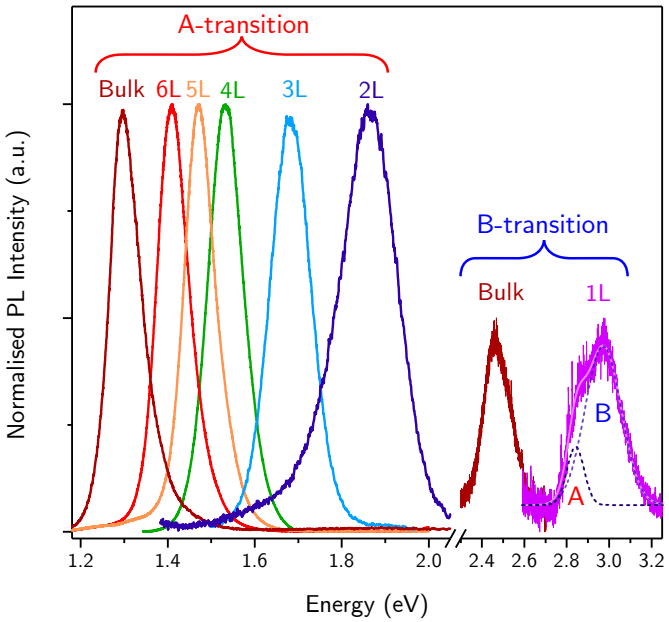

(a)

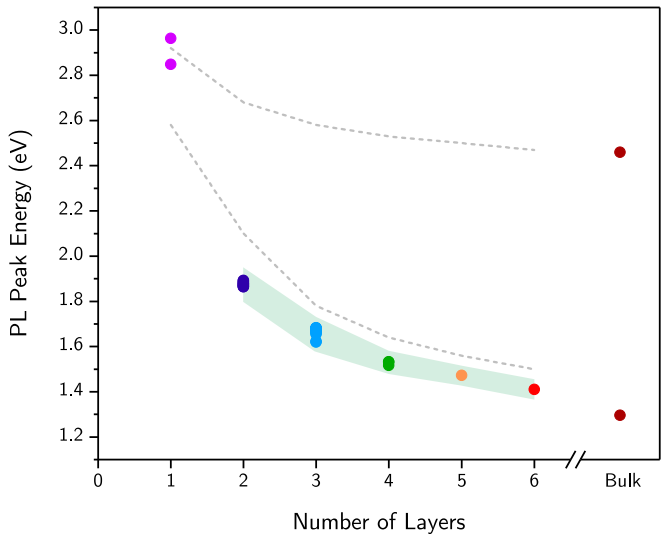

(b)

Figure 4.6: (a) Normalised PL for various InSe thicknesses from out-of-plane directed incident light. The higher energy peaks (hot PL) are normalised to half the value of lower energy peaks to demonstrate the lower general intensity. (b) Summary of PL peak energies for various hBN encapsulated crystals (∼30 total individually identified) with the full-width at half-maximum in the shaded area. The dashed lines are the theoretically expected band gaps obtained from DFT calculations.

in which the electrons recombine with holes deeper in the valence band. This is denoted as the B transition which, as discussed in Ch. 1, couples strongly

to in-plane polarised light and has been observed previously [94]. This hot PL is observed as the charge carriers excited to the higher energy band are more likely to radiatively recombine than non-radiatively relax to the lowest band. This is suggested to occur in InSe crystals because of the significant difference between the symmetries of the wavefunctions at the deeper valence band and the VBM (see Ch. 1.), which suppresses the potential relaxation routes of the holes and allows for the higher energy PL process to occur [94]. The PL peak energies are summarised in Fig. 4.6b alongside the DFT calculations for the A and B transitions of various InSe crystal thicknesses; shown as dashed lines. As is demonstrated, the measured PL peak energies agree well with the DFT calculations. However, from 6 to 2 layers an increasing divergence in the PL peak energy from the DFT calculations is observable. This may be due to an increasing binding energy in the excitonic ground state due to the increasing confinement (which is not incorporated into the DFT calculations), as observed for few-layer TMDCs which show large binding energy increases for reduced thicknesses [175]. A possible route to quantifying this is to perform STS measurements on few-layer InSe crystals.

For monolayer InSe, two transition peaks are expected from DFT calculations. The higher energy B transition is expected to couple more strongly to out-of-plane incident (in-plane polarised) light than the lower energy A transition due to the orbital compositions of the bands, see Ch. 1. Interestingly, the PL spectrum for monolayer may indeed be reasonably fitted with two peaks; see Fig. 4.6a. These two PL peaks may provide initial evidence for the existence of both transitions in monolayer InSe, although, both are close in energy and therefore difficult to distinguish clearly. However, it is suggested that high sample quality has allowed for their identification, which was previously unattainable.

Overall, one can distinguish the few-layer thickness of InSe from its respective PL peak energy. This tunability of the optical band gap with the layer thickness also increases the capabilities and opportunities for van der Waals heterostructures working in the near-infrared to violet regime.

In-plane Incident Excitation

As well as studying the PL from few-layer InSe in an out-of-plane incident excitation regime, the PL intensity of 10-layer InSe in an in-plane regime was measured as a function of its polarisation angle, see Fig. 4.7. In order to probe

InSe using in-plane incident light, a lamella of hBN encapsulated InSe was cut using a focussed ion beam. This was produced as follows. Initially, InSe was encapsulated in thick hBN and placed on a SiO_2/Si substrate as discussed in Ch. 2. Photoluminescence measurements were then taken in the out-of-plane regime as a control. Afterwards, a thin layer of AuPd and amorphous carbon were deposited onto the sample. Then, the sample was loaded into a focussed ion beam (FIB) dual-beam scanning electron microscope (SEM), wherein a thick layer of platinum (∼1 µm) was deposited onto it. With this, a rectangular section was cut through the sample by FIB milling, rotated by 90° and placed on a transmission electron microscopy grid. The edges that were milled (which give the cross-section of the hBN/InSe/hBN) were subsequently FIB polished in order to improve the cleanliness. This creation of the lamella by FIB was performed by A. Garner. A SEM image of the cross-section of the hBN/InSe/hBN heterostructure is given in Fig. 4.7.

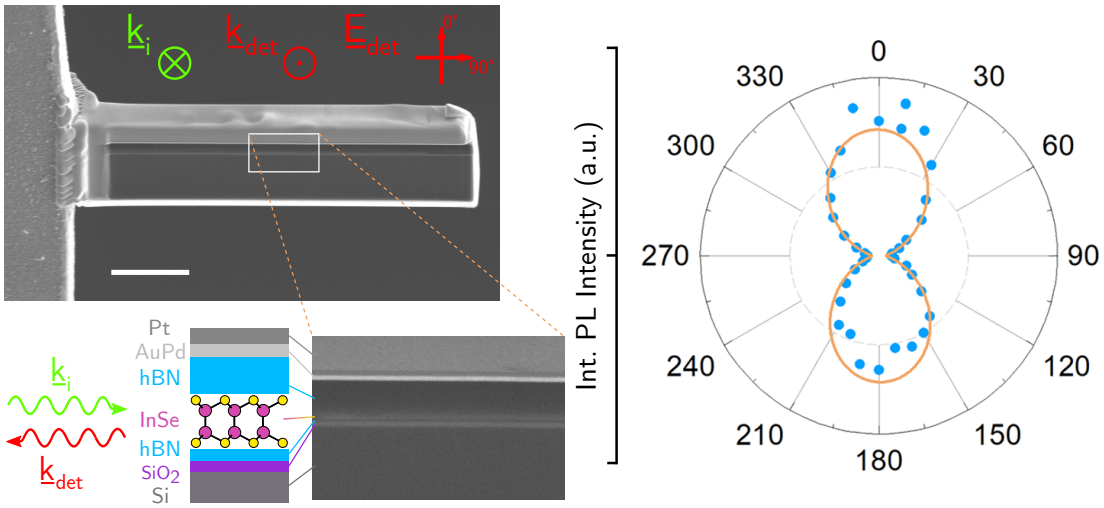

Figure 4.7: Left: A scanning electron microscope image of the cross-section of a hBN/InSe/hBN lamella (scale bar 5 µm), with incident light wave-vector $\underline{k}_i$ and detected PL wave-vector $\underline{k}_{det}$ and polarisation $\underline{E}_{det}$ directions annotated. The magnified image demonstrates the various layers in the lamella, with the 10L InSe visible. Right: Integrated PL intensity for various detection polarisation angles with orientation matching that given in the SEM image. Adapted from image published in [100].

The lamella was then cooled down to ∼4K for LT PL measurements. The incident excitation was unpolarised at a wavelength of 532nm but directed along the plane of the InSe crystal. As is shown on the right-hand side of Fig. 4.7, the integrated, low-energy PL intensity is maximised for polarisations that are

directed out of the plane of the InSe crystal. This polarisation dependence is expected from the wavefunction composition of the band minima in InSe [114]; which couples strongly to out-of-plane polarised photons but not to those in-plane. Overall, this demonstrates a new route towards probing in-plane incident excitation in 2D materials. This is an exciting possible avenue of research that may have implications for optical fibre technologies as 2D crystals such as InSe and GaSe couple strongly to out-of-plane polarised (in-plane incident) light [161]. From this, it is suggested that by implementing such materials into optical waveguides they may be used for example as excitation sources in ring lasers. These 2D crystals may be excited either by optical pumping or, more interestingly, by electric pumping via graphene/hBN based tunnel diodes; allowing for 2D material integrated optical fibre technologies [161].

4.1.3 SHG Studies

As discussed earlier, SHG is a valuable nonlinear optical technique that may probe the crystallographic axes of a thin polarisable film. Amongst the various 2D materials currently available, InSe presents itself as an interesting prospect for SHG measurements as, unlike TMDCs, it remains non-centrosymmetric for all layer thicknesses. In this section, the SHG collected from monolayer and few-layer InSe encapsulated in hBN is presented. As the second order nonlinear response from hBN is orders of magnitude less than that from InSe (also reported previously for MoS_2 [151]), its effect on the measurement of polarisation-resolved SHG is negligible. Prior to this work, only SHG from thicker few-layer InSe layers (minimum thickness of 9nm) had been observed [91].

The SHG signal collected from monolayer, bilayer, 5-layer and 10-layer InSe crystals are shown in Fig. 4.8. As is demonstrated, the SHG intensity increases significantly, up to 2 orders of magnitude, from the monolayer to the 10-layer crystals. The intensity of SHG $I_{2\omega}$ produced in a material may be shown to be proportional to its thickness d as [142, 148]

$$I_{2\omega} \propto l_c^2 I_\omega^2 \sin^2\left(\frac{\pi d}{l_c}\right) \tag{4.1}$$

Whereby the coherence length $l_c = \frac{\lambda_i}{2(n_{2\omega}-n_\omega)}$ is on the order of 10 µm. Thus, for atomically thin crystals of InSe, such that $d \ll l_c$, the intensity of SHG is proportional to the thickness squared. This is in close agreement with the

proportionality observed experimentally.

Importantly, discernible SHG is found to occur for even and odd numbers of layers, as expected for the non-centrosymmetric InSe. As discussed in Ch. 3, the γ-polytype has a non-centrosymmetric point-group that retains the same polarisation dependencies as its monolayer form. Thus, γ-InSe is suggested to be the polytype present in the fabricated crystals, further corroborated by evidence from scanning tunnelling electron microscopy studies based on the same bulk source crystals [176].

The polarisation dependence of the integrated SHG intensity is also clearly observable even for hBN encapsulated monolayer InSe crystals. These measurements were obtained through the use of a similar setup as that drawn in Fig. 3.7. Such a setup may probe the SHG signal that is polarised parallel to the incident light (co-polarised). This allows for the direct comparison of Eq. 3.14 with the acquired data; demonstrating the 6-fold rotational symmetry of the InSe crystal. From this, the crystallographic axis may also be accurately obtained non-invasively, as the maximum intensity for the co-polarised regime indicates the armchair axis (Ch. 3). This is a capability which may prove significantly useful for the design of future van der Waals heterostructures. The SHG intensity observed for thin InSe crystals is suggested to also be comparatively strong versus other 2D materials such as TMDCs. Recently, a study demonstrated that thin ($\sim$20nm) ϵ-InSe also has intense SHG that was 1-2 orders of magnitude greater than that of WS_2 [177]. Overall, few-layer crystals of InSe demonstrate intense SHG signals that are observable for both odd and even numbers of layers, in contrast to the well-studied TMDCs [151]; allowing for the accurate assessment of their crystallographic axes.

4.2 GaSe

4.2.1 Raman Studies

The phonon modes of monolayer GaSe are identified by the irreducible representations that characterise the symmetry properties of its point-group, D_{3h}. A summary of the irreducible representations for monolayer GaSe and their Raman activity and phonon dispersion is given in Fig. 4.9. The Raman activity and classification of the phonon modes of monolayer GaSe represents that of the

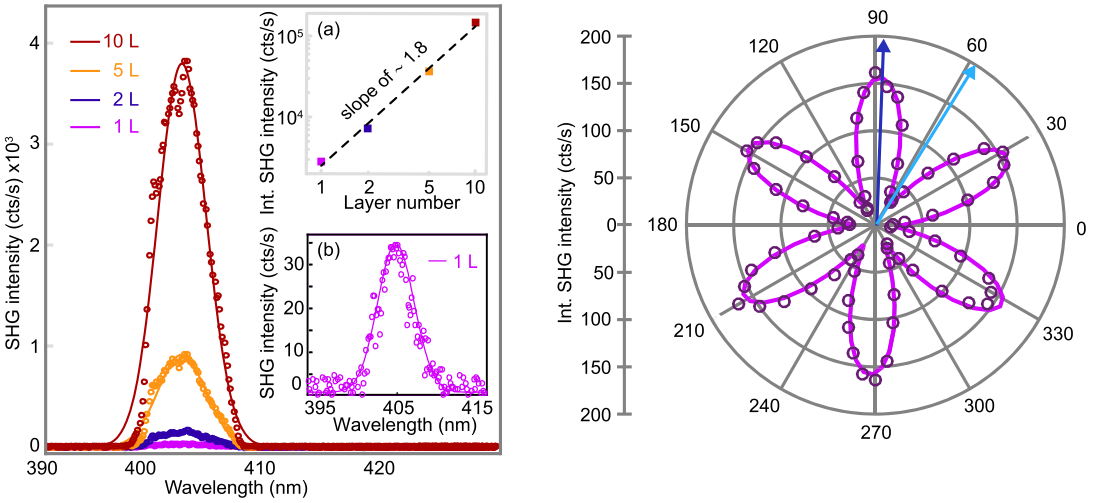

Figure 4.8: Left: SHG spectra for InSe few-layer crystals encapsulated in hBN with inset (a) demonstrating the quadratic increase of the intensity with layer number and (b) the SHG spectrum collected from monolayer InSe. Right: Polar plot of the integrated polarisation-resolved SHG intensity collected for monolayer InSe in the parallel (co-) polarisation configuration with a fitting of $r = A + C(\cos^2(3\theta + \psi))$ given by the solid line. The dark and light blue arrows indicate the armchair and zig-zag axes, respectively. Adapted from image published in [157].

multi-layered crystals (in ϵ-GaSe) as they also retain a similar symmetry. For this reason, Raman peaks for all thicknesses are categorised according to these irreducible representations, consistent with previous studies [152, 167] and with the studies on InSe presented above.

The Raman spectra obtained for monolayer to 6-layer GaSe crystals encapsulated in hBN are presented in Fig. 4.10a. All spectra were acquired in the backscattering regime with both co- and cross-polarised measurements taken. In each spectrum, three peaks are observable for the co-polarised measurements that are similar in frequency (Raman shift) to those expected from DFT calculations. These peaks represent three phonon modes that are characteristic of GaSe, illustrated by the relative atomic displacements presented in Fig. 4.10a. For cross-polarised measurements, only the the central peak, labelled E″(2), is observable whilst the out-of-plane vibrational modes reduce in intensity. As with InSe, this is expected from the selection rules that are dictated by the Raman tensors and experimental configuration; see Eq. 3.6 and [165].

As with InSe, the modes representing E″(2) and E′(2) are expected to have

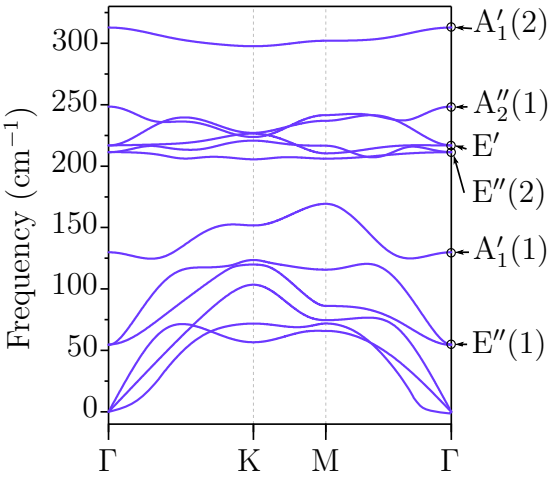

IrrRep	ω^{DFT}	Ratio	ω^{expt}
E″(1)	59.9	1:1	
A$_1'$(1)	130.6	1:0	135.7
E″(2)	211.1	1:1	214.5
E′	216.1	1:1	
A$_2''$(1)	252.0	0:0	
A$_1'$(2)	316.4	1:0	308.8

Figure 4.9: Phonon dispersion and Raman activity for monolayer GaSe obtained from DFT within the local density approximation (using Quantum Espresso). The flexural acoustic phonon branch (the lowest frequency branch) in the vicinity of the Γ point has numerical issues caused by a small supercell in the calculation and therefore may be ignored. The phonon modes are denoted by the irreducible representations (IrrRep) characteristic of the point-group D_{3h}. The theoretical phonon frequencies ω^{DFT} at the Γ point are given alongside the experimentally measured values ω^{expt}. The third column denotes the co-:cross-polarised Raman activity ratio such that 1 means it is active whilst a 0 means it is inactive. Adapted from [162], currently under review.

almost degenerate frequencies and a similar activity. Distinguishing between the two is not possible here and the Raman peak at 215cm^{-1} is tentatively ascribed to the E″(2) mode, as observed in previous studies [152, 167]. The two modes may be better distinguished in an alternative measurement geometry such that the activities of the modes are distinct [167]. Interestingly, for bulk GaSe crystals, a second peak at ∼219cm^{-1} is observable which may be associated with the E′(2) mode; see Fig. 4.11. Also, in contrast to InSe, the phonon mode A$_2''$(1) is not observable for any crystal thickness, as suggested by the selection rules. This mode was previously shown to be observable when the excitation energy was resonant with a higher optical transition [178]. Here, the excitation energy is well below this transition which is suggested to have an energy of ∼3.3eV for bulk GaSe; found from reflection measurements [179]. This assessment is consistent with the observations for thin InSe crystals. Figure 4.10b presents the intensity of the Raman mode at 309cm^{-1} for various excitation energies versus the optical transition energies (see the following section). As is demonstrated, when the excitation energy is resonant with the lowest optical transitions in

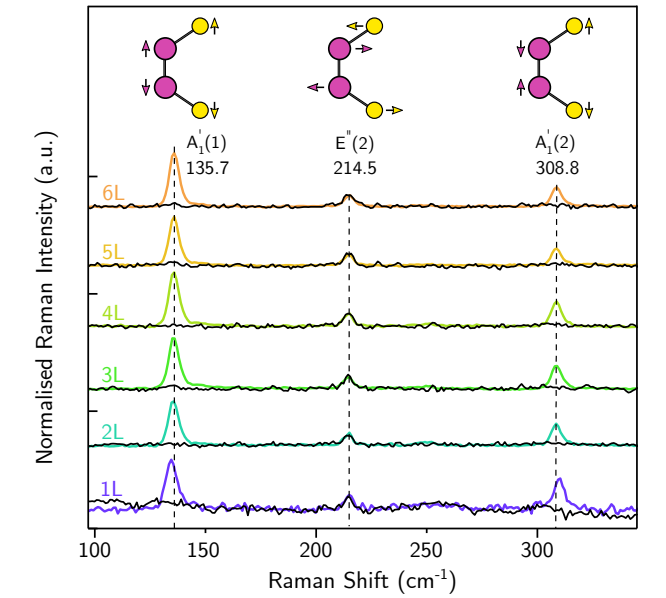

(a)

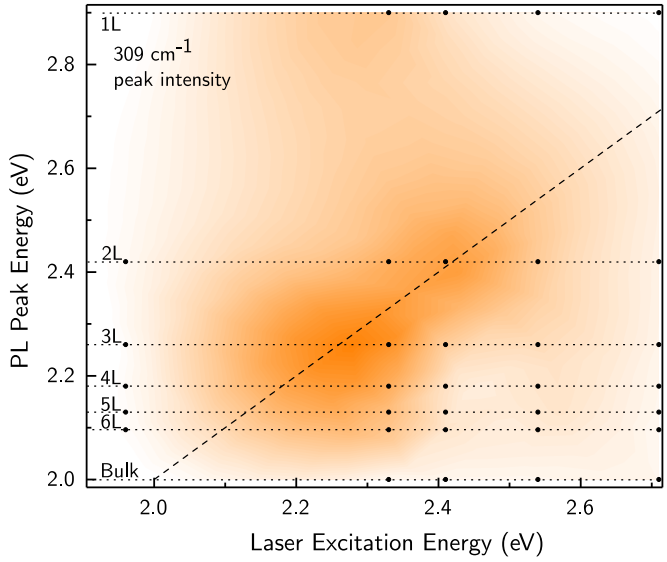

(b)

Figure 4.10: (a) Top: Relative displacements of the atoms for the respective phonon modes associated with (bottom) the Raman modes for few-layer GaSe. The co- (coloured) and cross-polarised (black) backscattering measurement regimes reveal different spectra for the various GaSe thicknesses under excitation at 2.33eV. (b) Intensity of the Raman mode at 309cm^{-1} for various excitation energies plotted against the PL peak positions of each crystal thickness (see Fig. 4.13a). White to orange denotes 0 to 30 counts and the dashed line indicates excitation energy equal to PL peak position. Adapted from image published in [161].

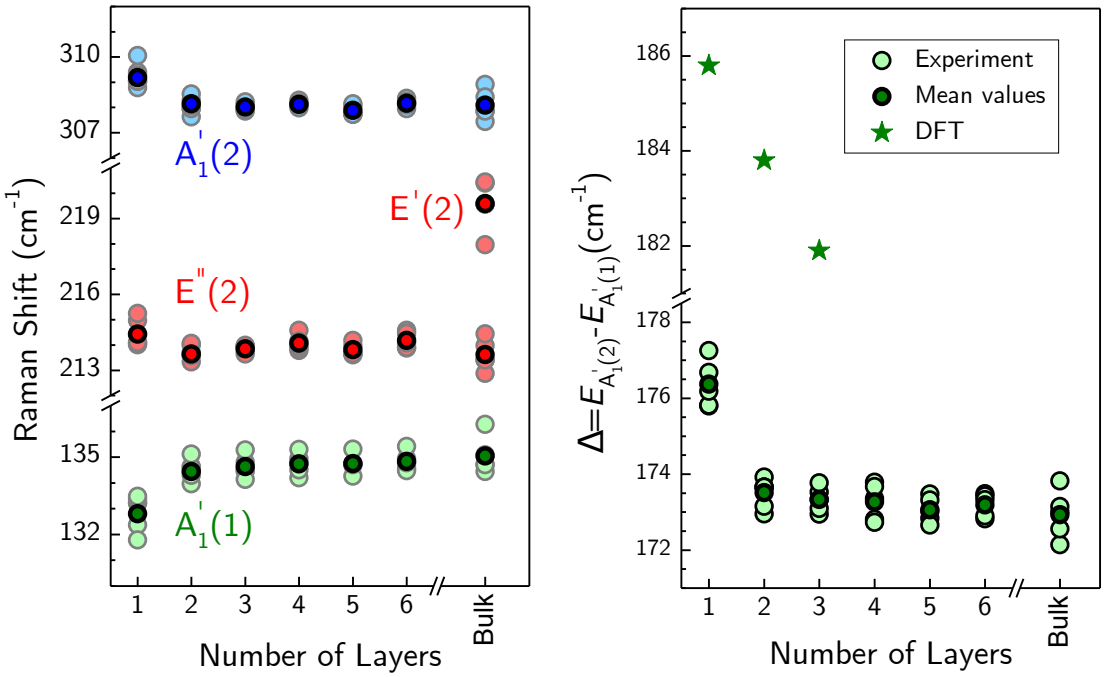

Figure 4.11: Left: A summary of the Raman peak shifts measured for various crystal thicknesses of GaSe. Right: The difference of between the A_1 Raman peak shifts (such that $\Delta = A_1'(2) - A_1'(1)$) for the various crystal thicknesses of GaSe alongside the DFT predicted differences (star symbols). The darker coloured symbols represent the mean values obtained from the data (lighter coloured symbols); which were measured at excitation energies from 1.96eV to 2.7eV. Adapted from [162], currently under review.

GaSe, the intensity of the Raman mode increases significantly. This supports the designation of the optical transition energies in Fig. 4.13a. Note that the intensity of the Raman mode was normalised according to the 214.5cm^{-1} intensity and then the layer number, excitation power and acquisition time.

Previous studies that measured the Raman spectrum of unencapsulated GaSe crystals showed that only one mode, A_1', was observable for the thinnest films [81, 103, 180, 181]. However, as these crystals were unencapsulated, it is suggested that significant degradation was likely (see Fig. 2.8 and Fig. 2.9) and the Raman spectrum was simply that of the underlying silicon; which shows a peak at a similar frequency of ∼300cm^{-1} [81, 180]. As with InSe, the hBN encapsulation in an inert atmosphere allows for the retention of crystal quality for clear Raman spectra.

A summary of the Raman shifts for the various GaSe crystal thicknesses is given in Fig. 4.11. As the thickness of GaSe is reduced down to a monolayer,

clear shifts in the Raman spectra are observable. The A_1-type vibrational Raman peaks shift to opposite energies whilst the E-type vibrational peak remains approximately constant. As with InSe, the right panel shows the difference Δ between the A_1 peak Raman shifts for the various crystal thicknesses. For monolayer GaSe, Δ demonstrates a similar shift to that predicted from DFT calculations and that of InSe. However, the value of Δ is only significantly shifted for monolayer crystals, unlike that observed for InSe crystals. As this remains true despite repeated measurements, it is not suggested to be an outlying result. However, as this is the first reported set of Raman spectra for few-layer GaSe, further investigation is suggested. From the results presented here, the quantity Δ may be used to identify monolayer GaSe.

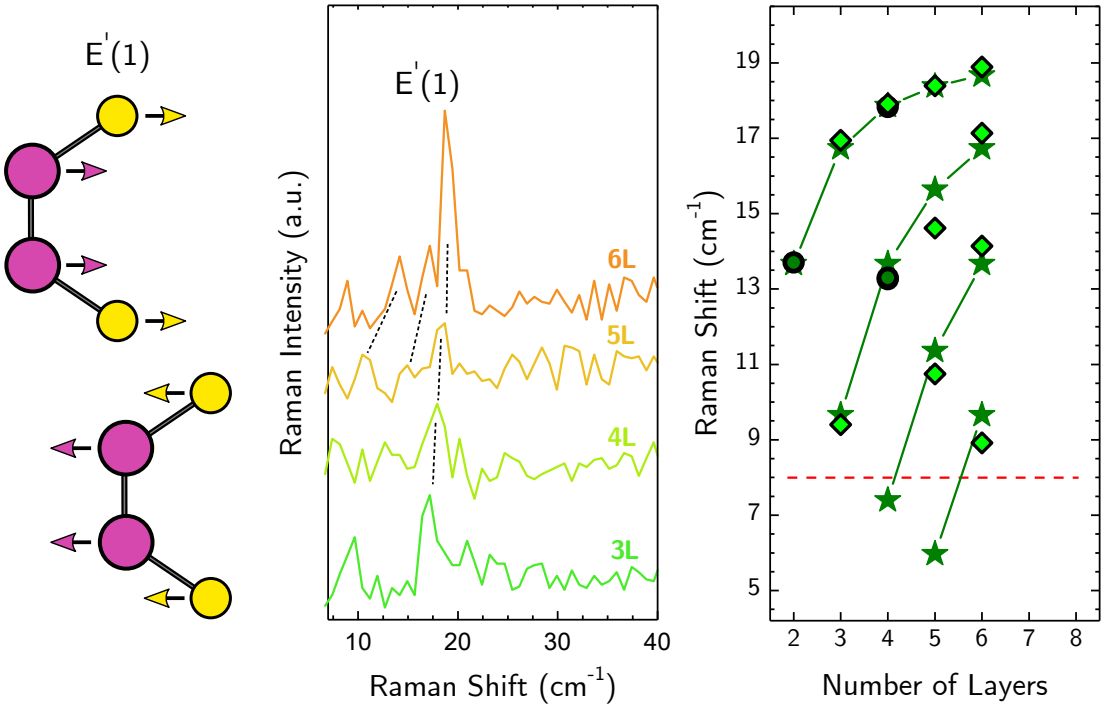

Figure 4.12: Left: Relative displacements of the atoms within a unit cell for the respective phonon shear modes associated with (centre) the low frequency Raman scattering modes for various GaSe crystal thicknesses under excitation at 2.41eV. Right: A summary of the measured Raman shear modes (diamond and circle symbols) alongside the predicted values from a linear chain model and DFT calculations (star symbols). The dashed line represents the limit of the measurable spectra. Adapted from [162], currently under review.

The low frequency Raman modes for thin GaSe crystals are also investigated and presented in Fig. 4.12. As is shown, the crystal thickness has a systematic

effect on the low frequency vibrational modes. These are found to closely resemble the expected shear mode frequencies found using a linear chain model and DFT calculations of the force constants as well as those in [182]. As with InSe, the breathing modes are not observed here.

Overall, the Raman spectra for hBN encapsulated GaSe crystals with thicknesses from bulk down to monolayers has been presented. The intralayer and interlayer vibrational modes for the various crystal thicknesses have been identified alongside theoretical predictions, demonstrating Raman spectroscopy as a technique for studying crystal symmetries and as a tool for the identification of monolayer crystals.

4.2.2 Photoluminescence Studies

The PL spectra for various GaSe crystal thicknesses encapsulated in hBN are presented in Fig. 4.13a. As the thickness of the GaSe crystal is decreased from bulk to bilayer, the PL peak energy is observed to increase from ∼2.0eV to ∼2.4eV. The increase of the PL peak energy suggests that the optical band gap of GaSe significantly widens as the number of layers is reduced to a few layers; in agreement with previous theoretical predictions [76, 95, 103] and those given here. The PL peak energies for the various GaSe crystal thicknesses are summarised in Fig. 4.13b alongside the calculated band gaps from DFT calculations. It is found that the PL peak energies closely follow the calculated band gap values, with an increasing energy difference observed for thinner layers. This may be related to an increasing binding energy of the excitonic ground state due to an increasing confinement, which is not incorporated in the DFT calculations. The systematic increase of the optical band gap with decreasing thickness is accompanied by a decreasing PL intensity. As expected, this is similar to InSe as the band gap at the Γ point is suggested to become increasingly indirect; see Ch. 1.

Prior studies that attempted to observe PL from few-layer GaSe have reported no significant change in the PL peak energy [87, 183–185]. This is summarised in the inset of Fig. 4.13b, alongside the results obtained here which, in contrast, show a significant and systematic change in PL peak energy. This trend is in agreement with previous STS [109] and cathodoluminescence [113] measurements; see Table. 1.3. As with the previous Raman studies, the lack of PL change with layer thickness in the literature is suggested to be due to the lack of encapsulation, which allows for the deterioration of crystals through oxidation

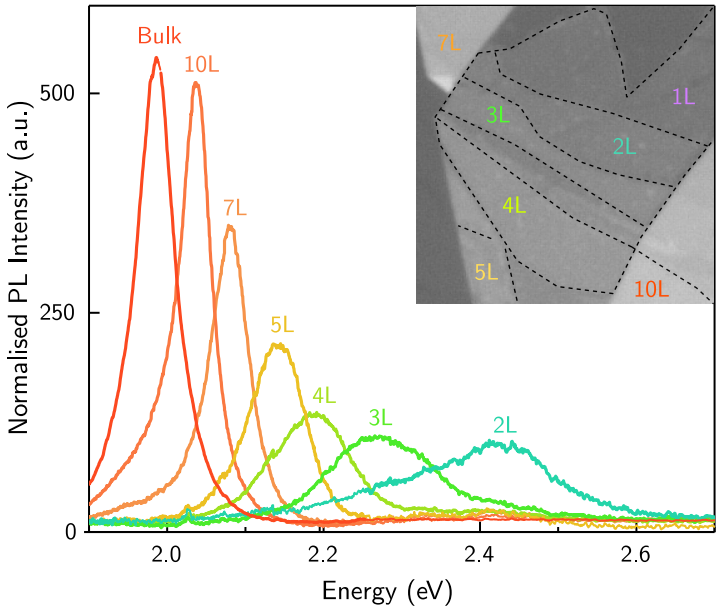

(a)

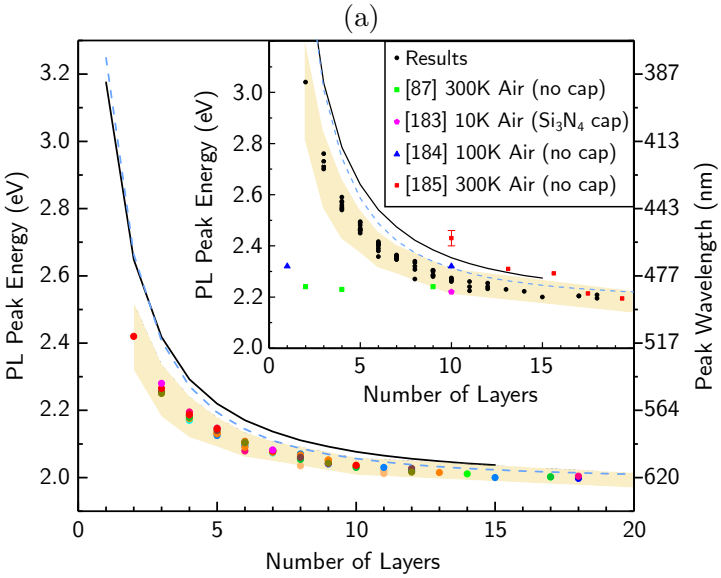

(b)

Figure 4.13: (a) PL spectra for GaSe from a single sample with multiple crystal thicknesses normalised by the layer number found with AFM. Inset is an optical image of the hBN encapsulated GaSe crystal (width 20 µm). (b) Summary of PL peak energies for various hBN encapsulated GaSe crystals (∼70 total individually identified) with the full-width half-maximum in the shaded area. The dashed and solid lines are the band gaps theoretically calculated from a hybrid k.p tight-binding model and scissor-corrected DFT, respectively. Inset shows previously reported GaSe PL variation with layer thickness. As published in [161].

[128, 129, 186–188]; see Fig. 2.8. Overall, 17 samples of hBN encapsulated GaSe were fabricated using the methods described in Ch. 2. This resulted in over 80 individual regions of varying thicknesses (confirmed by AFM) available for study. To measure the PL of the thinnest layers (at an energy >2.2eV), a custom-built optical setup was established, with the integration of a 405nm laser and high efficiency optical components in order to optimise the collection of PL. For bulk GaSe crystals (defined to be >15 layers), a PL peak energy of (1.992±0.006)eV is obtained, in agreement with previous results [87, 185, 189]. For monolayer GaSe crystals, although Raman spectra were clearly observable, no PL was observable up to 3.8eV. As with InSe, the band gap (and therefore the PL peak energy) is expected to shift significantly from bilayer to monolayer crystals as well as becoming more indirect, reducing the PL intensity. The expected PL peak energy of monolayer GaSe is suggested to be between 3.0-3.5eV, based on the trends observed here, theoretical calculations and previous reported band gap values from other experiments [109, 113].

Layers of GaSe can be stacked as four different polytypes (ϵ, γ, β and δ); as introduced in Ch. 1. From theoretical calculations, these are expected to have slightly different band gap energies (∼50meV) [79] and each has been observed in the literature [83]. Thus, to establish which polytype the GaSe crystal used here was, transmission electron microscopy and diffraction studies were performed [161]. In order to achieve this, GaSe crystals were first encapsulated in graphene and transferred onto SiN substrates which had a grid of holes pre-fabricated in them. With this, high angle annular dark field (HAADF) scanning transmission electron microscope (STEM) images were obtained from several few-layer GaSe crystals; see Fig. 4.14. The intensity contrast between the spots is consistent with that of the simulated intensities from the ϵ-polytype and δ-polytypes; see Fig. 4.14c and d which give the simulated intensities for the ϵ-polytype and the experimental image. Further inspection of the intensity ratio of the diffraction spots (Fig. 4.14b) suggests it is inconsistent with the δ-polytype and is therefore identified as ϵ-polytype. The intensity ratio also allows for the identification of the crystal thickness. [161]

Overall, for the first time, a significant shift in the optical band gap of few-layer, hBN encapsulated, ϵ-GaSe has been demonstrated through PL spectroscopy. With this, it has been shown that one can distinguish the thickness of few-layer GaSe by analysing its PL peak energy. Alongside InSe, GaSe crystals

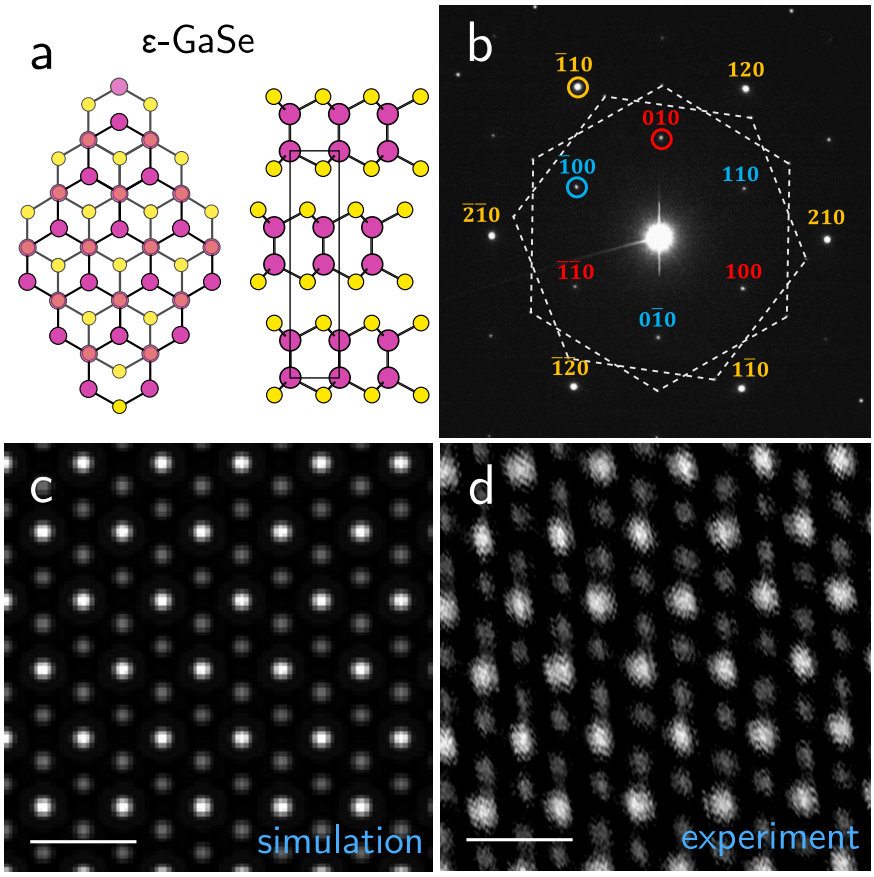

Figure 4.14: (a) The stacking arrangement of ϵ-GaSe from a top and side-view. Purple (yellow) atoms are representative of Ga (Se) atoms with the overlap positions (forming a redder colour) indicating the positions of higher intensity (b) Experimental electron diffraction pattern of few-layer, graphene-encapsulated, GaSe. The circles correspond to the spot indices used to obtain the intensity ratios used for determining thickness and crystal polytype. The spots corresponding to the two encapsulating graphene sheets are connected by dashed white lines. (c) HAADF simulated image for the ϵ-GaSe polytype. (d) Atomic resolution HAADF STEM images of few-layer, graphene-encapsulated, GaSe. Scale bars 0.5nm. As published in [161].

allow for dense coverage of room temperature optical activity from the infrared ($\sim$1.3eV) to the visible ($\sim$2.5eV) spectrum. This opens up the opportunity for a selection of a wide range of optical band gaps for integration into van der Waals heterostructures.

4.2.3 SHG Studies

Crystals of GaSe have, historically, been well researched for their nonlinear properties, demonstrating strong optical conversion in the mid to far-infrared [83, 92, 93]. As a result, GaSe was suggested to be a leading candidate for frequency conversion devices in this range. However, bulk crystals of GaSe were also reported to be mechanically too soft, deforming easily [83]. This aspect of GaSe is of little consequence in the context of crystals combined into van der Waals heterostructures; potentially enabling further optimisation as a frequency converter. As GaSe has a similar crystal structure to InSe, it is also distinctive amongst 2D materials in that it remains non-centrosymmetric for all layer thicknesses. The SHG signal collected from encapsulated monolayer, bilayer, trilayer and 6-layer GaSe crystals are shown in Fig. 4.15. As with InSe, the SHG intensity increases by 2 orders of magnitude as the thickness is increased from a monolayer to a 6-layer crystal.

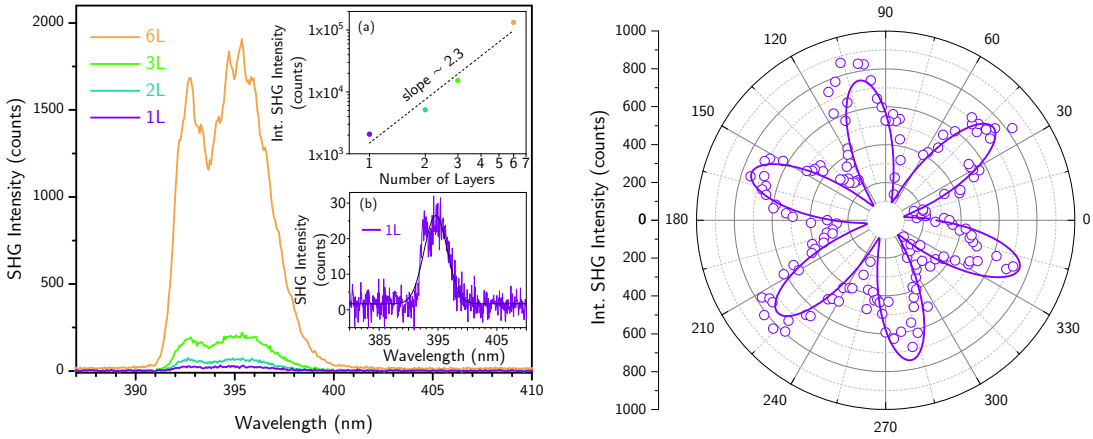

Figure 4.15: Left: SHG spectra for hBN encapsulated GaSe few-layer crystals pumped at wavelength 785nm with inset (a) demonstrating the quadratic increase of the intensity with layer number and (b) the SHG spectrum collected from monolayer GaSe. Right: Polar plot of the integrated polarisation-resolved SHG intensity collected for monolayer GaSe in the parallel polarisation configuration with a fitting of $r = A + C(\cos^2(3\theta + \psi))$ given by the solid line.

The SHG intensity also demonstrates a dependence on crystal thickness that is slightly greater than that observed for InSe crystals and that expected from Eq. 4.1. This is consistent with a previous study that found the second-order susceptibilities for few-layer GaSe crystals (<7L) to decrease with thickness at a greater rate than expected (based on bulk crystal SHG trends) [153]. Note

that these crystals were also under vacuum. The reduction of the second-order susceptibilities was suggested to be due to the significant increase of the band gap of GaSe for few-layer crystals, as previously predicted and also demonstrated here from PL spectroscopy. This band gap increase (and subsequent band energy changes) may reduce the interaction with the fundamental wavelength and therefore the SHG, as suggested from an observation that the GaSe SHG intensity doubles when the fundamental pump energy is resonant with the band gap energy [190].

Despite the expected reduction in intensity, SHG from monolayer GaSe is observable, along with its six-fold rotational symmetry. This allows for the non-invasive determination of its crystallographic edges, as demonstrated for few-layer InSe crystals. The SHG is also observable for odd and even layers, as expected for ϵ-GaSe crystals that retain a non-centrosymmetric point-group at all layer thicknesses.

4.3 Summary

In this chapter, studies regarding the optical properties of two PTMCs, GaSe and InSe, protected by hBN encapsulation were presented. Initially, the Raman spectra for bulk to monolayer InSe crystals were given, showing dependence on thickness that is particularly salient for few-layers. Following this, the PL observed from InSe crystals for incident out-of-plane and in-plane excitation was given, showing systematic changes in PL energy with the number of layers as well as higher energy PL (B-transition) and polarisation angle dependence for PL directed in-plane. Then, SHG from few-layer InSe crystals was observed for odd and even layer numbers, in contrast to TMDCs, demonstrating that the crystallographic axes of these layers may be established. Afterwards, the Raman spectra for bulk to monolayer GaSe crystals were given, showing similarities to InSe that allow for probing of crystal symmetries and thickness. The systematic and significant change in PL peak energy with GaSe crystal thickness was also presented, observed for the first time due to its protection by hBN encapsulation. Lastly, SHG from few-layer GaSe crystals was reported for odd and even layers, also demonstrating that the crystallographic axes of these layers may be established for further device fabrication. In the following chapter, these two PTMCs are brought together to form new excitonic states.

Chapter 5

Γ Point Interlayer Excitons in van der Waals Heterostructures

When two different semiconducting materials are brought together to form heterojunctions, the Fermi level equilibrates with the respective band structure energies aligning in different profiles depending on the band offset and doping. These profiles can be categorised by the type of band offset observed between the CBMs and VBMs of the two materials. Figure 5.1 demonstrates the different types of band alignment.

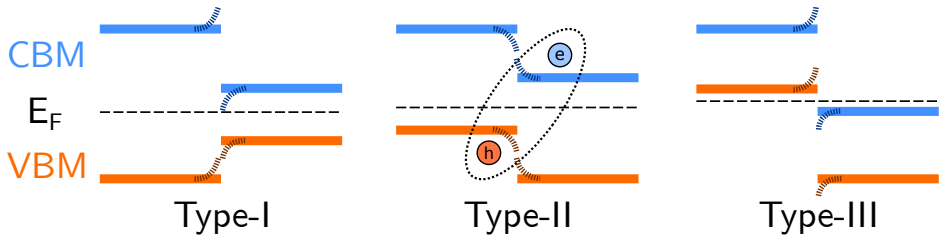

Figure 5.1: Conduction band minima (CBM) and valence band maxima (VBM) alignment types at a heterojunction formed between two semiconducting materials with their equilibrated Fermi level (E_F). Dashed lines illustrate possible band bending scenarios near the interface of bulk semiconductors. The locations of an electron and a hole in opposite bands of adjacent materials (forming an interlayer exciton) is demonstrated for type-II alignment.

Type-I band alignment is observed when the CBM and VBM of one material are at higher and lower energies, respectively, than the other material. Such an alignment is utilised for efficient blue InGaN light-emitting diodes (LEDs) [191]. Type-II band alignment is observed when the CBM and VBM of one material are both at higher energies than the other material whilst in type-III

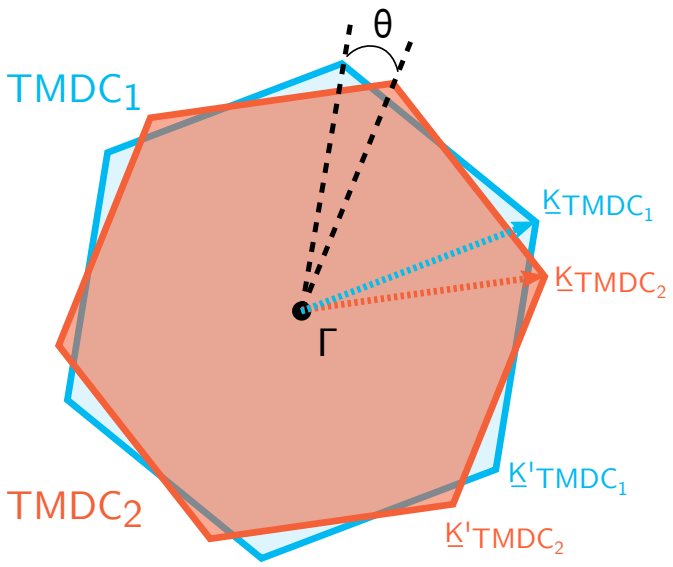

Figure 5.2: Relative BZ alignment for two TMDCs twisted by an angle θ.

alignment the bands in one are high enough that the VBM of one is higher than the CBM in another. Type-II band alignment is utilised in GaInAsSb/GaSb LEDs and photodiodes that operate at a wavelength of $\sim 2\,\mu$m [192, 193] whilst type-III alignment may be used to form a tunnelling barrier, as exhibited in GaSb/InAs devices [194]. Alongside the alignment type, the relative doping of the semiconductors can influence the bands near the heterojunction interface as the majority carriers diffuse into the adjacent materials; causing band bending. This bending direction is dependent on the doping type [138]. In the case of atomically thin 2D crystals, in which the whole material can be considered an interface, this band bending is suggested to be negligible. Previously, band bending in the *basal* plane direction between atomically thin 2D crystals has been suggested to occur over the scale of ∼10-100nm and thus in the direction perpendicular to the basal plane, where the whole heterostructure exists over a few nm's, the bending is considered to be negligible [195, 196].

Typically, when two group-VI TMDC monolayers are brought together (creating a heterobilayer), a type-II band alignment is formed [197, 198]. This band alignment has underlined the study of interlayer excitons (iXs); quasiparticles of interacting electrons and holes that are localised in adjacent semiconducting layers. The electrons inhabit the lower energy CBM whilst the holes the higher energy VBM; see Fig. 5.1. As the charges are spatially separated between crystals, the iX is denoted as being spatially indirect. In TMDC heterobilayers, the

CBM and VBM of the individual monolayers are at their respective BZ corners (the K and K′ points). For lattice mismatched and misaligned TMDC monolayers, these BZ corners are rotated relative to one another around the Γ point; see Fig. 5.2. Therefore, as the charges are also separated in momentum space, the iX is also denoted as being momentum indirect. Thus, iXs are suggested to have a significantly weaker oscillator strength (a lower probability of formation and recombination) than the intralayer excitons of their respective monolayer TMDCs [197]. With this, however, comes longer lifetimes and the capability to electrically tune the exciton energy due to its out-of-plane nature [199]. The momentum-space separation between the gaps of adjacent monolayers may be minimised if the crystal lattices are aligned. From this, the iX becomes more direct in momentum space which increases its oscillator strength. Indeed, an observed increased in the iX PL intensity has been shown for closely aligned $MoSe_2/WSe_2$ [200] and MoS_2/WS_2 [201]. Note that for MoS_2/WSe_2 heterobilayers, no increase in the iX PL intensity was observed for closely aligned monolayers [202]. The iX in this heterobilayer is proposed to relate to a Γ-K transition instead, relaxing the constraints of alignment.

In this chapter, new excitonic states that form between 2D semiconducting materials in van der Waals heterostructures are presented. Initially, evidence for new iX states at a PTMC/PTMC heterojunction is given. These are suggested to form around the BZ centre (instead of the BZ corners) of the materials in a type-II band alignment. Afterwards, the observations of iX states that form in type-II band alignments at the BZ centre of PTMC/TMDC heterojunctions are given, demonstrating bright and wide tunability.

5.1 GaSe/InSe Quasi-Γ Point Interlayer Excitons

5.1.1 Introduction

In this section, heterostructures of hBN encapsulated few-layer GaSe and InSe are discussed; as published in "Terry et al., 2D Materials 2018" [161]. As examined earlier, these two materials have quasi-direct band gaps, with their band edges at or near the Γ point in the BZ. As will be demonstrated, with the creation of few-layer GaSe/InSe heterostructures, new excitonic states are

observed. These are suggested to be iX states that form between the Γ points of the materials due to type-II band alignment formation between n-type doped InSe and nominally undoped GaSe. Note that it has been reported that nominally undoped GaSe is p-type [75].

Previously, type-II heterojunctions of *bulk* GaSe/InSe have been fabricated through molecular-beam epitaxy (otherwise known as van der Waals epitaxy in the case of these materials) demonstrating clean interfaces [203–205] and type-II band alignment according to Anderson's rule [204]. In these heterostructures, thin crystals of GaSe and InSe down to ∼10nm were investigated through photoelectron spectroscopy and scanning tunnelling microscopy. Interestingly, these thin crystals were fabricated and probed prior to the isolation of graphene. However, the optical properties of such heterojunctions were not investigated nor were few-layer heterostructures formed. Other attempts at forming these heterojunctions through mechanical exfoliation demonstrated electroluminescence [206] and photodetection [207]. However, in both of these instances, bulk crystals were used (the thinnest crystal reported was 13nm, equating to ∼16 layers).

Here, mechanical exfoliation is used to isolate high-quality *few-layer* GaSe and InSe crystals in an inert atmosphere, which upon protection with hBN are probed for their luminescent properties. Newly observed luminescent peaks are suggestive of iX states that exist around the central Γ point in reciprocal space, remaining bright due to an almost direct (quasi-direct) momentum-space transition regardless of crystallographic alignment. Also, as the band gaps of the respective PTMCs vary with layer number, the energy of the iX states are energetically tunable. This represents a new set of bright and tunable iX states in few-layer 2D materials, not requiring crystal alignment. All heterostructures were fabricated and measured by myself (with the exception of transmission electron microscopy imaging which was done in collaboration with D. Hopkinson).

5.1.2 Fabrication

In this study, hBN encapsulated GaSe/InSe heterostructures were fabricated using the techniques described earlier in Ch. 2. GaSe and InSe were exfoliated onto PPC inside an argon filled glovebox with transfers performed using the dry peel technique. Transmission electron microscopy (TEM) images and selected area diffraction patterns were obtained on two of these heterostructures. To acquire these, the fully encapsulated stacks were transferred onto SiN substrates

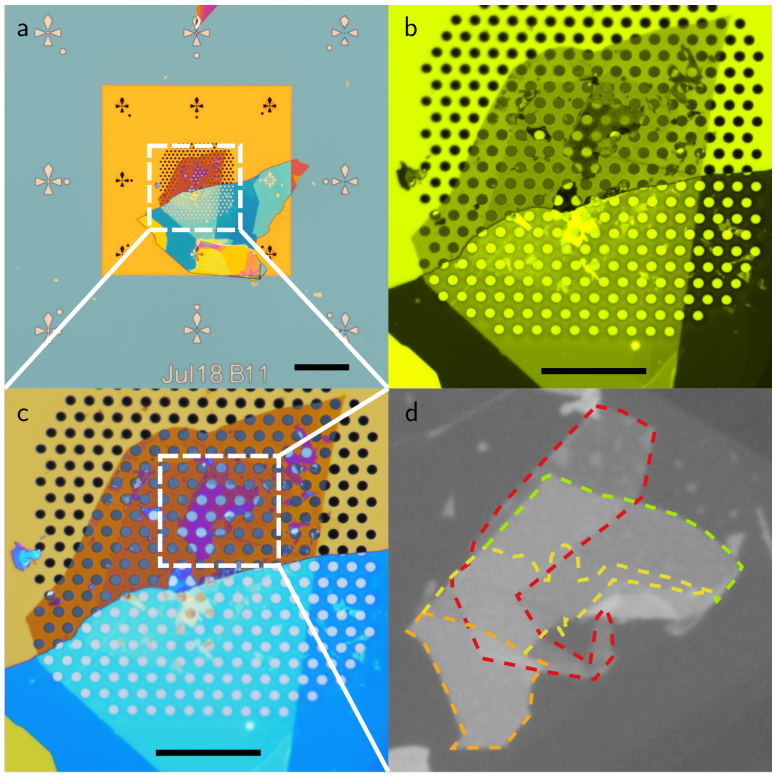

Figure 5.3: Bright-field optical images of an encapsulated GaSe/InSe heterostructure deposited on a TEM grid at (a) lower magnification demonstrating the wider grid structure and at, (b) and (c), higher magnifications showing the heterostructure regions on top of the grid. A yellow filtered optical image (b) gives a higher contrast showing the overlap region more clearly. (d) Optical image of the heterostructure before transfer with the InSe and GaSe outlined in red and orange-yellow, respectively. Scale bars are given as (a) 50 µm, (b) and (c) 25 µm and (d) image width is 25 µm.

with grids of holes pre-fabricated in them to allow for TEM imaging. One such TEM SiN grid with a GaSe/InSe heterostructure deposited onto it is shown in Fig. 5.3.

5.1.3 Results

Room temperature PL spectra from various positions on a heterostructure containing hBN encapsulated 9-layer GaSe that is partially overlapped by 2- and 4-layer InSe is shown in Fig. 5.4a. For the isolated GaSe and InSe crystals, PL peaks are observed at the expected energies (cf. Ch 4). However, for the overlap regions, new PL peaks (denoted as iX^{M-InSe}_{N-GaSe}) are observed with energies offset from their constituent layers. These are suggested to originate from interlayer,

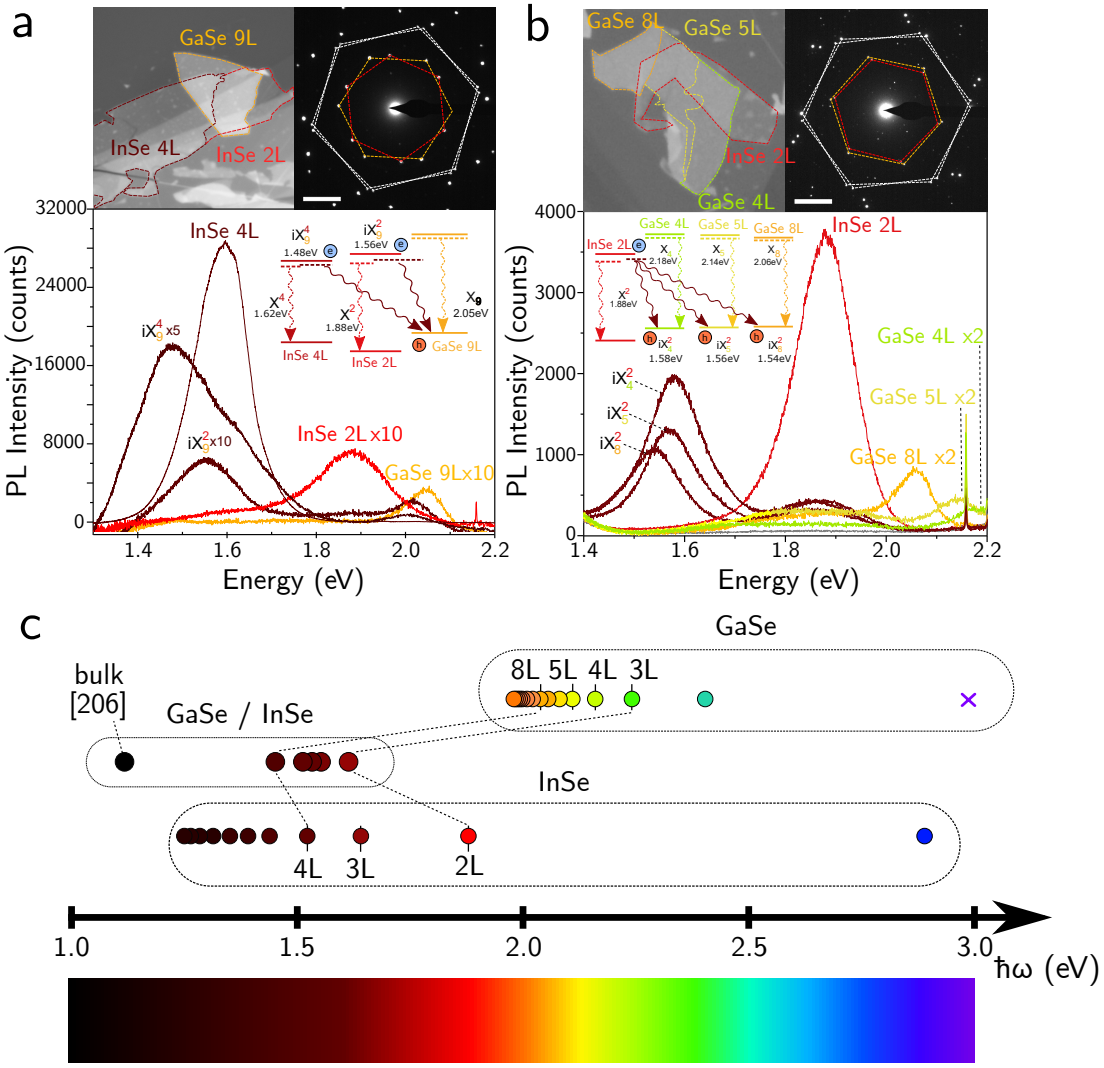

Figure 5.4: (a) and (b) Top: optical images of hBN encapsulated GaSe/InSe heterostructures, with outlined InSe (red) and GaSe (orange-yellow) crystals, image width 30 µm (a) and 25 µm (b), with corresponding selected area electron diffraction patterns demonstrating the twist angles between the PTMCs (InSe red, GaSe orange, hBN white); scale bar 2nm^{-1}. Bottom: RT PL spectra for encapsulated N-layer GaSe and M-layer InSe crystals alongside their corresponding overlapping regions showing iX emission (denoted as $\text{iX}^{M-InSe}_{N-GaSe}$), note that the peak at ∼2.16 eV is due to a hBN Raman mode. Inset: Illustrations show corresponding band alignment of the N-InSe and M-GaSe heterostructure giving the iX energy. Solid lines are band edges, dashed lines are excitonic states. (c) Summary of measured samples with dots representing the PL peak energies. The indirect transition in the heterostructures is blue-shifted from 1.1eV previously observed in a heterojunction of bulk InSe and GaSe [206]. As published in [161].

spatially indirect excitons occurring in a type-II band alignment, as observed in TMDC heterobilayers [197]. For bulk GaSe/InSe heterojunctions, this type-II band alignment has previously been reported [204], with the band edge energies of InSe being lower than those of GaSe. This alignment is further evidenced by the tuning of the luminescence peak energy with the selection of PTMC layer number. As the InSe layer number is increased from 2 to 4, the luminescent peak energy shifts by ∼80meV from iX_9^2 to iX_9^4. Simultaneously, as the GaSe layer number is increased from 4 to 8, the luminescent peak energy in the overlap regions (iX_4^2, iX_5^2, iX_8^2) also gradually shifts; see Fig. 5.4. The PL intensity from these proposed iXs is also found to remain between the brightness of the individual PTMC components.

In order to test the influence of the twist angle on PL, GaSe/InSe heterostructures of similar crystal thicknesses but with different crystallographic twist angles were compared. Selected area electron diffraction (SAED) images obtained on two GaSe/InSe heterostructure overlap regions, iX_8^2 and iX_9^2, demonstrating twist angles of ∼21.7° and ∼2.7°, are shown in Fig. 5.4a and b, respectively. In both cases, the PL peak intensities are of the order of magnitude of the constituent PTMC layers' PL intensity and even slightly more intense than that observed for isolated GaSe layers. This is in stark contrast to the iX room temperature PL intensities typically observed for TMDC heterobilayers, which are orders of magnitude less than the constituent layer's PL intensities and barely observable for misaligned angles ($10° < \theta < 50°$) [200]. The PL peak energies between the aligned and misaligned GaSe/InSe heterostructures have a difference of ∼20meV, which is within the variation observed for individual PTMC components of constant thickness (see Fig. 4.6b and 4.13b).

As the band gaps for both PTMCs exist near the Γ point, the iXs also form at this position in the BZ. Thus, in agreement with our experimental observations the twist angle and lattice mismatch of the two PTMCs is of little consequence to the quasi-direct momentum-space transition, giving bright excitons at room temperature. The new luminescent peaks obtainable through the combination of GaSe and InSe expand the energy range of room temperature optical wavelengths available from these two PTMCs; see Fig. 5.4c. Moreover, the availability of other similar PTMCs such as GaS and InS, as well as the capability to alloy them (for example as $Ga_xIn_{1-x}Se$), can expand the spectral coverage even further, presenting future research opportunities.

Overall, initial evidence has been observed at room temperature for the existence of bright and energetically tunable interlayer excitonic states around the Γ points in few-layer PTMCs. As these excitonic states are located around the Γ point, they remain bright independent of the relative crystal alignment of the component materials, unlike the twist-dependent PL observed previously for TMDC heterobilayers.

5.2 InSe/TMDC Γ Point Interlayer Excitons

5.2.1 Introduction

As introduced in Ch. 1, for bilayer or thicker TMDC crystals, the corresponding band gap is indirect between the Q_c and Γ_v points in the BZ; see Fig. 1.5. As the band gap becomes indirect for multi-layers, the resultant PL intensity is typically reduced by at least an order of magnitude in comparison with monolayers [45, 208]. For multi-layers of TMDCs, the VBM occurs exactly at Γ point but the CBM does not. Oppositely, for PTMCs the CBM occurs exactly at the Γ point but the VBM does not; cf. Fig. 1.5 and 1.8. Thus, one posits that for a type-II band alignment of a TMDC/PTMC heterostructure, the global CBM and VBM could both occur at the Γ point, assuming the bands offset accordingly, see Fig. 5.5 for an illustration. This, similar to GaSe/InSe heterostructures, would then allow for the examination of iX states at Γ, with a difference that the global VBM is exactly at Γ, as opposed to being close to it, and thus stronger interband transitions are expected. Also, the pronounced absorption shown in TMDCs at energies close to their band gap [45, 209] suggests a potential for greater interlayer exciton formation than compared with GaSe/InSe heterojunctions for which strong absorption has not been observed in either PTMC. Lastly, as with PTMCs, the band gaps of TMDCs decrease with increasing layer number. Thus, the interlayer excitonic states formed between the type-II heterojunction are suspected to be widely tunable due to the various TMDC band gaps available.

In this section, the studies of new excitonic states in heterostructures of hBN encapsulated few-layer TMDC/InSe heterojunctions are discussed. The new excitonic states are suggested to be iX states formed between the Γ points of adjacent materials that form a type-II heterojunction. These heterostructures were fabricated through the techniques outlined in Ch. 2, with the results presented here

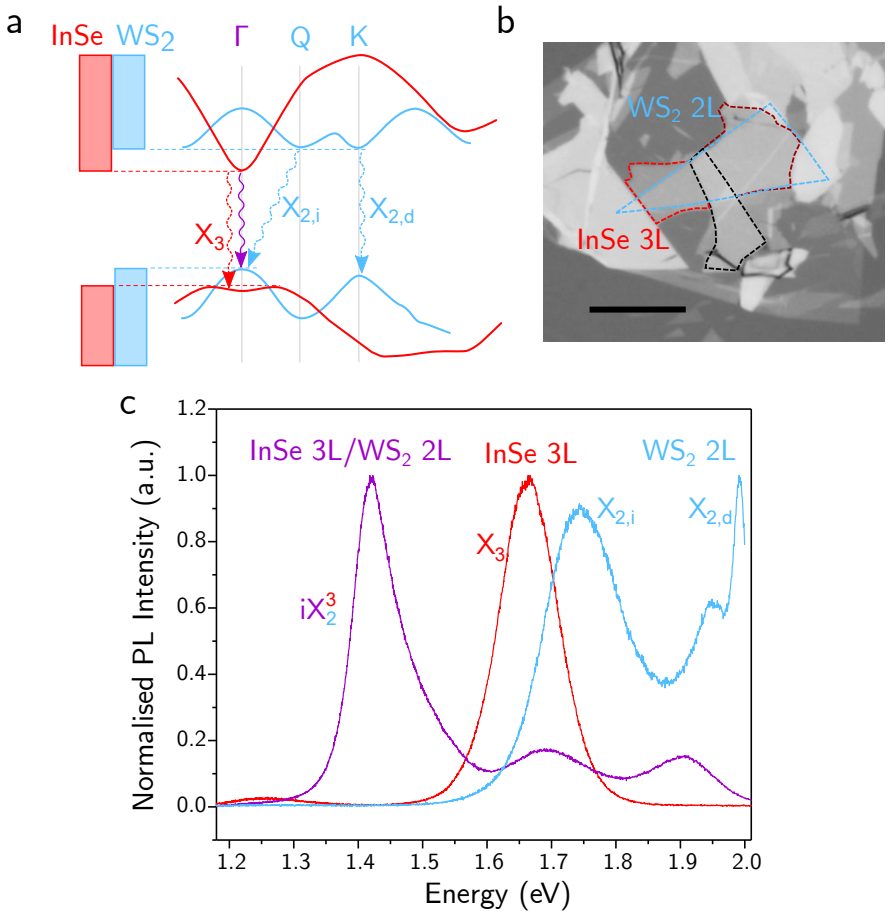

Figure 5.5: (a) Band alignment of trilayer InSe (red) and bilayer WS_2 (blue) demonstrating the band edges and structures around the Γ, Q and K points in the BZ. The band transitions associated with the different excitonic states are also given. (b) An optical image of a hBN encapsulated InSe-3L/WS_2-2L heterostructure with the PTMC and TMDC layers outlined in red and blue, respectively. Scale bar 10 µm. (c) Room temperature photoluminescence of the isolated and overlapping regions in the InSe/WS_2 heterostructure.

currently under review. The heterostructures were fabricated and measured in collaboration with N. Ubrig, E. Ponomarev, J. Howarth and J. Zultak.

5.2.2 Results

Figure 5.5a demonstrates the band structures of InSe-3L and WS_2-2L overlapped with their energies offset from one another. The two materials are suggested to form a type-II band alignment (with the InSe band edges below those of WS_2), in line with those previously reported for InSe/$MoSe_2$, InSe/WSe_2 [211],

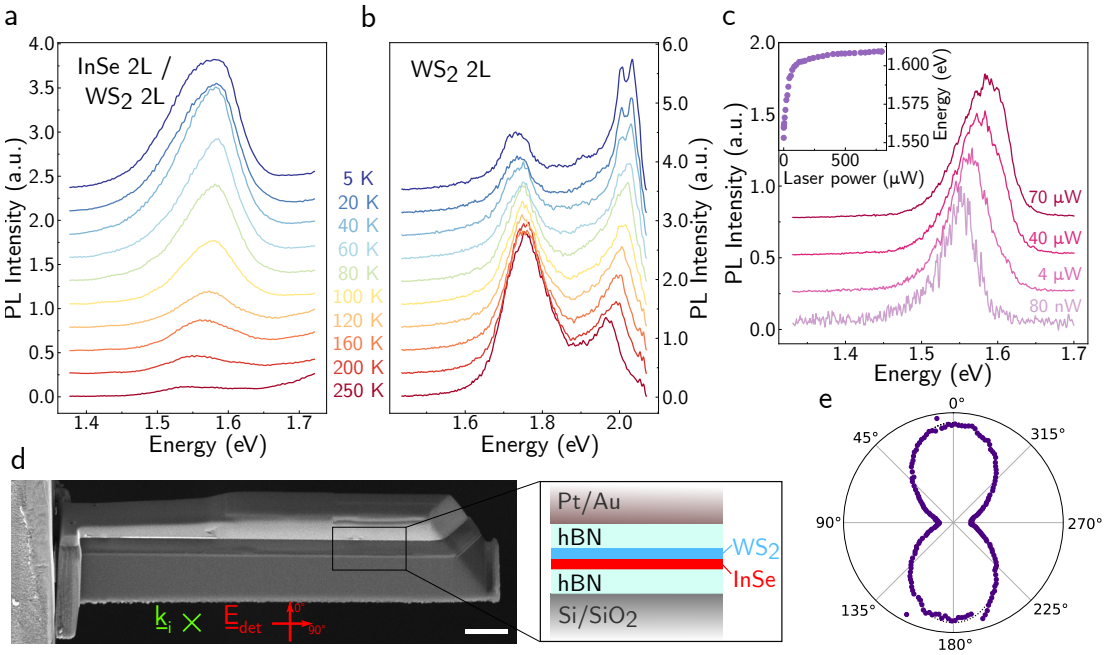

Figure 5.6: Photoluminescence spectra for (a) an InSe-2L/WS_2-2L heterojunction and (b) an isolated WS_2-2L at various temperatures. (c) PL spectra for an InSe-2L/WS_2-2L heterojunction at T=5K for increasing excitation laser powers. (d) Scanning electron microscope image of a cut InSe-6L/WS_2-2L heterojunction from the side-on view with a schematic showing the constituent layers, scale bar 2 µm. (e) Polar plot of the iX PL polarisation from the interface in the cut heterostructure in (d) with 0° corresponding to a polarisation that is perpendicular to the 2D material plane (the dashed line is a sinusoidal fitting of the data). Adapted from [210], currently under review.

InSe/MoS_2 [212] and TMDC/TMDC band offsets [213], each predicted from work function analysis. A corresponding heterostructure of InSe-3L/WS_2-2L encapsulated in hBN is shown in Fig. 5.5b with the individual crystals outlined. The PL obtained from the individual and overlapped crystals are given in Fig. 5.5c. The individual crystals display PL characteristic of their respective thickness [94, 208]. However, the overlapping region displays a strong PL peak at a significantly lower energy, with minor peaks around the energies of the individual crystals. As with the case of GaSe/InSe heterojunctions, this is believed to be due to a type-II band alignment between the InSe and WS_2, allowing for the observation of iXs. This new PL peak energy is then used to reconstruct the approximate alignment of the band structures of InSe and WS_2; see Fig. 5.5a.

Figures 5.6a and b demonstrate the PL temperature dependence of an InSe-2L/WS_2-2L heterojunction and an isolated WS_2-2L region. As the temperature

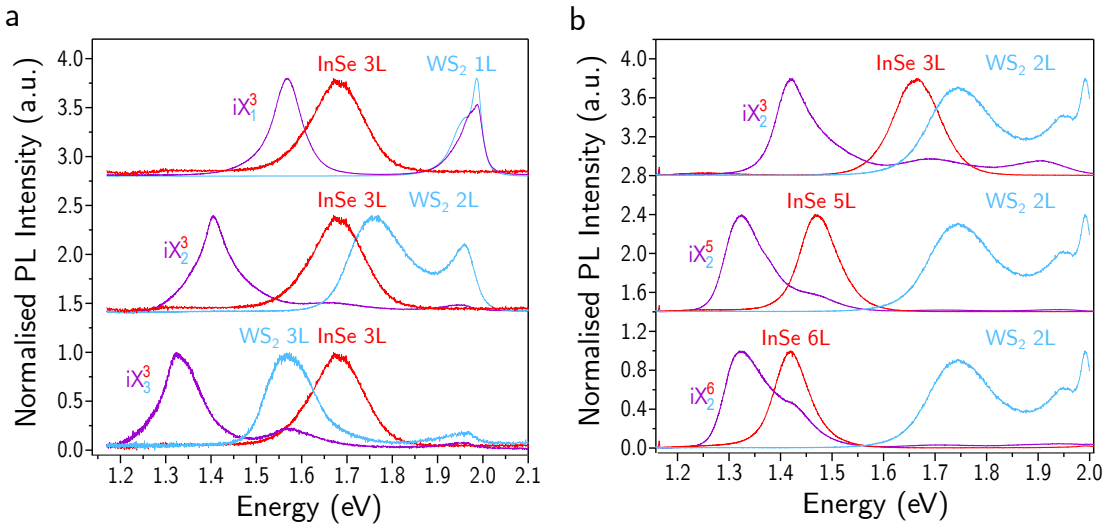

Figure 5.7: Room temperature photoluminescence measured from hBN encapsulated InSe/WS_2 heterostructures of different combinations of crystal thickness with constant (a) InSe thickness and (b) WS_2 thickness. PL for the heterojunction, isolated InSe and WS_2 are in purple, red and blue, respectively.

decreases, the intensity of the PL from the heterojunction is observed to increase, suggesting that the transition is direct in momentum-space. A similar trend is observed for the higher energy (∼2eV) PL peak of the isolated bilayer WS_2; which is associated with a momentum-direct transition at the K point. Oppositely, the lower energy PL peak decreases in intensity with cooling, as is typical for momentum-indirect transitions requiring phonon-mediation. The excitation laser power dependence of the InSe-2L/WS_2-2L interlayer PL is shown in Fig. 5.6c. As the power is increased, the PL peak energy blue-shifts by ∼50meV and then stabilises. This is similar behaviour to that observed previously for iX states between TMDCs [214]. Here, the blue-shift is suggested to result from an increasing dipole-dipole repulsion between interlayer excitons with increasing exciton density [214, 215]. Overall, the peak energy as well as the temperature and power dependencies suggest the new luminescence observed on InSe/WS_2 heterostructures to originate from interlayer excitonic states.

As briefly discussed in Ch. 1 and further investigated in Ch. 4, the X-p_z orbitals in few-layer InSe (which dictate the interband transitions at Γ) couple strongly to out-of-plane polarised photons but not to in-plane photons [114]. This is similar for TMDC orbitals at the Γ point, see Table 1.1. As well as this, for an interlayer exciton the electron-hole dipole exists across the heterojunction, coupling strongly to out-of-plane electric fields such as polarised light. Thus, it

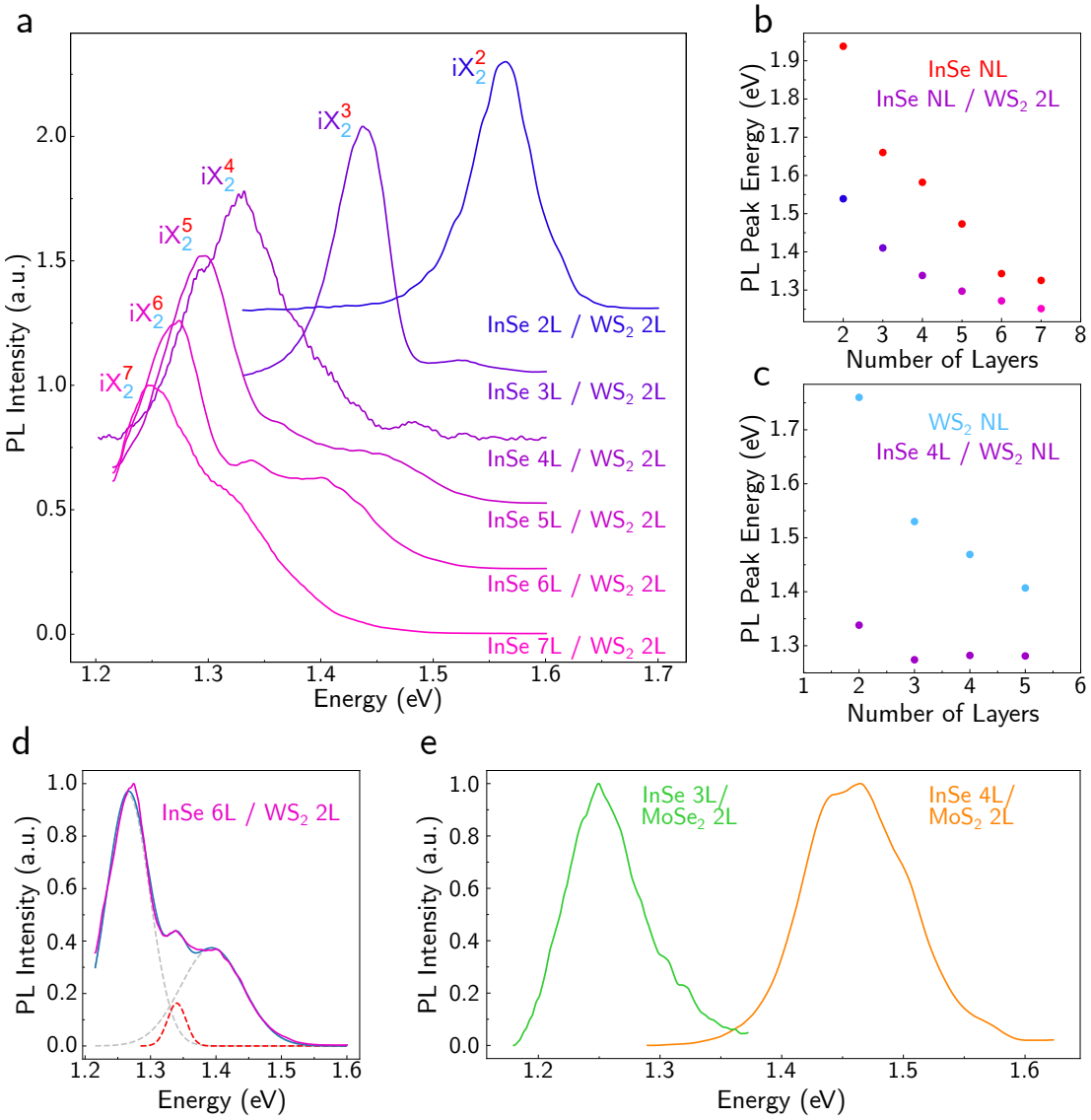

Figure 5.8: (a) Low temperature (T=5K) photoluminescence observed for InSe/WS_2 heterostructures of different InSe crystal thicknesses, summarised in (b) alongside a summary of InSe PL peak energies. (c) Summary of PL peak energies for WS_2 alongside those found for InSe-4L/WS_2-NL. (d) LT PL of a InSe-6L/WS_2-2L with the observation of a secondary new peak at 1.34eV. (e) LT PL measurements demonstrating newly observed excitonic peaks for InSe/$MoSe_2$ and InSe/MoS_2. Adapted from [210], currently under review.

is expected that the PL from the iX is primarily polarised in an out-of-plane direction. To investigate this, an InSe-6L/WS_2-2L heterostructure encapsulated in hBN on a Si/SiO_2 substrate was cut using a focussed ion beam into a bar (of size 2 µm × 20 µm × 0.7 µm) such that one edge revealed the heterojunction; see Fig.

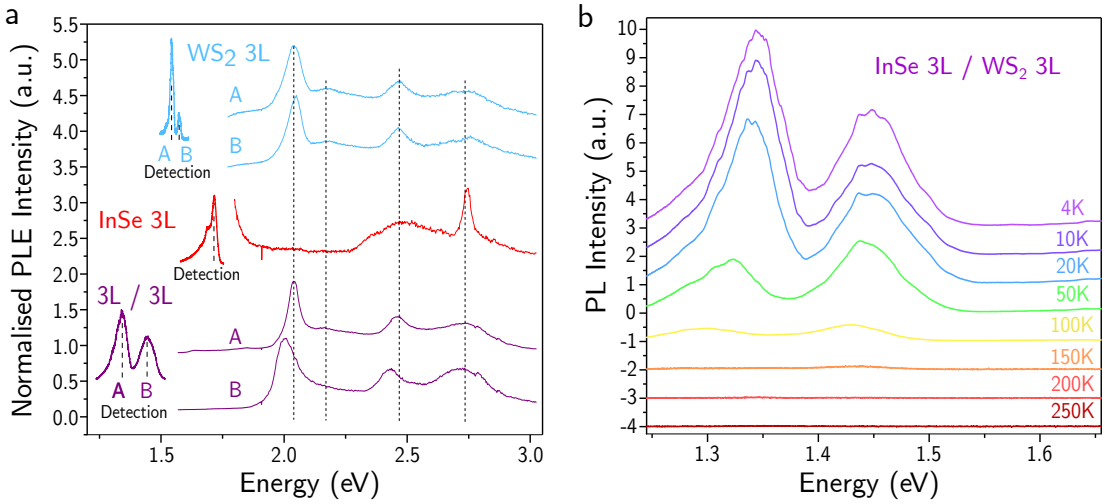

Figure 5.9: (a) Photoluminescence excitation spectra for an InSe-3L/WS_2-3L heterojunction (purple) alongside those for the corresponding isolated WS_2 (blue) and InSe (red) crystals at T=5K. (b) PL for the InSe-3L/WS_2-3L heterojunction at various temperatures.

5.6d. With this, the polarisation dependence of PL (from the iX) propagating along the basal plane of the interface was measured, see Fig. 5.6e, revealing a significant polarisation preference for the out-of-plane direction; further suggesting that the new luminescence peaks originate from interlayer excitonic states.

By selecting a TMDC or InSe layer's thickness, one may also select an intralayer band gap energy and thus the corresponding PL. In constructing an InSe/WS_2 heterostructure, one may tune the interlayer band gap at the Γ point by selecting the thickness of both materials. The systematic tuning of the interlayer band gap, and thus the iX energy, with the selection of different layer thicknesses is shown in Fig. 5.7 and 5.8. Figure 5.7a demonstrates the room temperature PL for trilayer InSe crystals adjacent to monolayer, bilayer and trilayer WS_2. As the WS_2 thickness increases, the intralayer and interlayer PL peak energies decrease. If the WS_2 thickness remains constant, but the InSe thickness increases, the PL peak energies also decrease; see Fig. 5.7b. This therefore demonstrates the availability of an assortment of iX energies by simple crystal thickness selection. Note that for InSe-3L/WS_2-1L, there are two strong PL peaks observed. The higher energy peak is most likely due to the strong intralayer excitons formed at K (direct band gap) in monolayer WS_2, possibly originating from regions in which interlayer contamination prevents direct contact between the crystals. The lower energy PL peak is below the energy of either of the intralayer

peaks but is also of higher intensity than the higher energy PL peak, suggesting the iX states to also recombine strongly. The continuous iX peak energy shift is also observed for the LT PL of various other InSe/WS_2 heterostructures, see Fig. 5.8a, b and c.

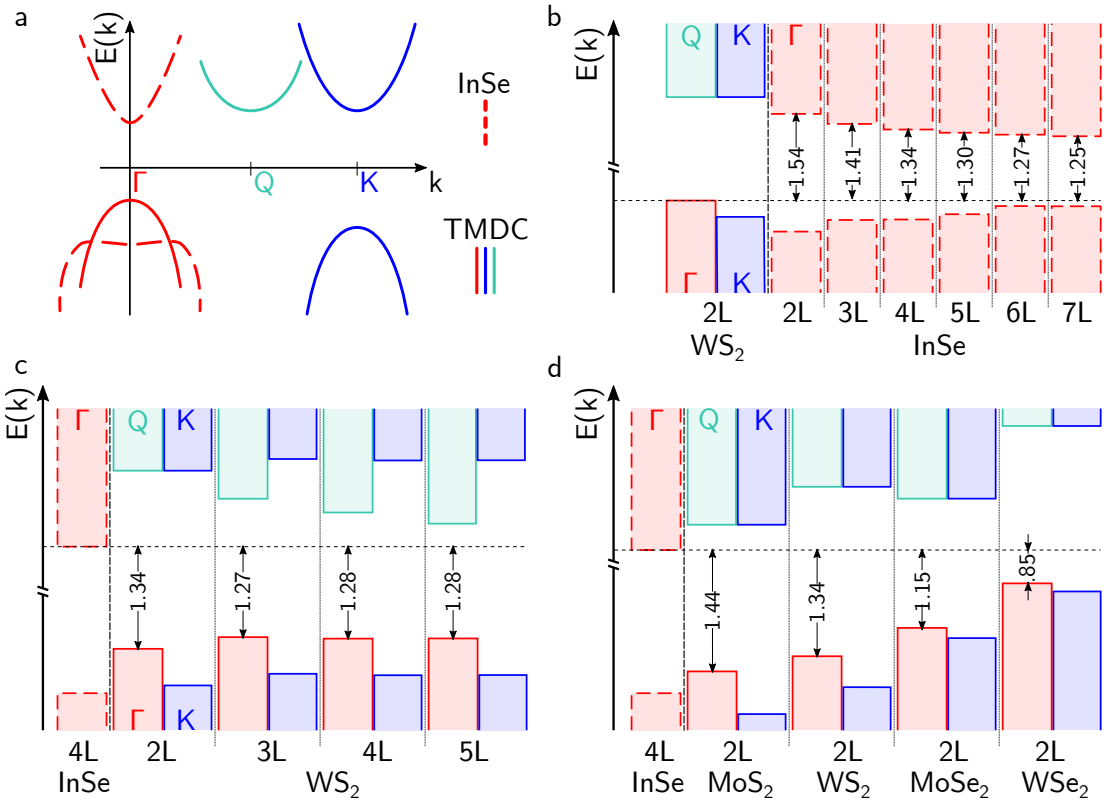

Figure 5.10: (a) Approximate band structures at the band edges of InSe (dashed) and TMDC (solid) at the Γ (red), Q (green) and K (blue) points in the BZ. Band alignments constructed from intralayer and interlayer PL for InSe/WS_2 (b) and (c) and various InSe/TMDC (d) heterostructures showing the iX energies between the Γ points. Adapted from [210], currently under review.

Interestingly, for an InSe-6L/WS_2-2L heterostructure, two new PL peaks are observed alongside a higher energy peak that is associated with the InSe intralayer exciton; see Fig. 5.8d. These two peaks are separated by ∼70meV with the more intense being the lower energy peak. Around the InSe-6L/WS_2-2L thickness combination, it is suggested that the energy at the top of the K_v band in WS_2 is similar to the top of the Γ_v band in InSe; see Fig. 5.10. This is tentatively suggested to have an effect on the interlayer excitonic states, potentially causing a splitting in them at Γ due to their mixing. Furthermore, for

an InSe-3L/WS_2-3L heterostructure, two PL peaks are also observed to be significantly shifted from one another (∼100meV) at LT (T = 5K); see Fig. 5.9a. These two peaks increase in intensity upon cooling (Fig. 5.9b), suggesting them to both be momentum-direct transitions, but have slightly shifted absorption spectra, as demonstrated by photoluminescence excitation (PLE) spectroscopy. For the isolated, encapsulated WS_2 and InSe trilayers, the PL and PLE spectra reveal peaks at energies (including higher energy B-transitions, cf. Fig. 4.6) that closely match those previously reported for these layer thicknesses [94, 208, 216]. However, the InSe-3L/WS_2-3L heterojunction reveals two PL peaks that have similar, but slightly shifted, PLE spectra. These PLE spectra closely match that of the isolated WS_2, suggesting a strong dependence on the direct transition at or near the K point (at ∼2eV) in the WS_2 crystal. These spectra also suggest that the charge carriers can relax from locations at the BZ corners (K and K′) to Γ. The mechanism for this relaxation is unclear, although bands at Q may act as intermediary states (cf. Fig. 1.5). The formation of the two PL peaks in the InSe-3L/WS_2-3L heterostructure is also tentatively attributed to the process proposed for the InSe-6L/WS_2-2L heterostructure in which the energy of a K_v band in WS_2-3L is suggested to be similar to the top of the Γ_v band in InSe-3L, causing splitting at Γ due to mixing.

The combination of InSe with other TMDCs has also been investigated. New LT PL peaks are observed for combinations of few-layer InSe with $MoSe_2$ and MoS_2; see Fig. 5.8. These observations further demonstrate the capability to tune the iX energies between InSe/TMDC heterostructures. These other iX states in InSe/TMDC heterostructures are also assumed to possess momentum-direct transitions due to the similarities in the band structures between TMDC materials. Using the PL measurements obtained from a variety of InSe/TMDC layer combinations, one can begin to construct the band alignments between the materials by analysis of the respective intralayer and interlayer exciton PL energies; see Fig. 5.10. Note that this ignores binding energies and assumes that Γ and K are at a similar energy for bilayer TMDC materials. The error in the alignment is given as ∼100meV, the order of magnitude for exciton binding energies in 2D materials [57]. From the band alignments, it is observed that as the InSe layer number is increased, both band edges shift in energy whilst for WS_2 only the conduction band edge shifts significantly.

Overall, evidence for the formation of Γ point interlayer exciton states between few-layer InSe and various TMDCs has been presented. These iX states are bright at room temperature and observable for a variety of TMDC materials, allowing for the tuning of the iX energy by layer thickness selection. These iX states also preferentially emit light polarised in the out-of-plane direction. Initial observations of two PL peaks originating from InSe/WS_2 heterojunctions are also presented, suggesting the possibility of more complex interlayer excitonic states. These results put forward InSe/TMDC heterostructures as widely tunability emitters that do not require crystal alignment, demonstrating their potential for scale up either through direct growth or wafer-scale transfer whereby twist angle is difficult to control.

5.3 Summary

In this chapter, two distinct cases of type-II band alignment in 2D semiconductors were presented, revealing new excitonic states. Initially, interlayer excitonic states that form in PTMC/PTMC heterojunctions demonstrated strong PL at room temperature, independent of the twist angle of the crystals. This is suggested to be due to the iX formation around the Γ point in the BZ, which does not depend strongly on twist angle for momentum-direct transitions. After this, observations of strong PL in PTMC/TMDC heterojunctions were given, indicative of the formation of iX states forming at a Γ point type-II band alignment. These demonstrated wide tunability with layer thickness selection, allowing for dense spectral coverage over a wide energy range in van der Waals heterostructures.

Chapter 6

Resonantly Hybridised Excitons in Moiré Superlattices in van der Waals Heterostructures

6.1 Introduction

As briefly introduced in Ch. 1, when two similar van der Waals crystal lattices are brought together, a moiré superlattice may form with its period dependent on the relative crystal mismatch and twist angle. Similar to graphene/hBN heterostructures, bilayers of TMDCs may also form moiré superlattices with a period dependent on the selected crystals and their twist angle. If these TMDCs are different, a heterobilayer may form with type-II band alignment; allowing for iXs.

Recently, it's been shown through STS measurements that the interlayer band gap may locally vary over the moiré period (∼8nm) due to long range shifts in the stacking configuration [184, 217]. This interlayer band gap variation is suggested to be large enough (∼0.1eV) for closely aligned TMDCs that excitons may be confined in real space periodically over the moiré superlattice, such that an array of quantum emitters may be formed [218, 219]. Not only this, but due to the rotational symmetry of the different stacking configurations at periodic locations in the moiré superlattice, the confined excitons are also only coupled to one particular circular polarisation direction [219]. These moiré dependent excitons are known as 'moiré excitons'.

Investigations into moiré excitons have already begun, with initial evidence being observed in different aligned TMDC heterobilayers. For an aligned WSe_2/

$MoSe_2$ heterobilayer, multiple peaks in the PL spectra were observed to have alternate dependencies on the incident and emitted circularly polarised light. This was suggested to be due to excitons trapped in moiré potentials which have quantised energy levels and alternating wavefunction symmetries [220]. Another recent work probed an aligned WSe_2/WS_2 heterobilayer. This demonstrated new, separated absorption peaks near the intralayer WSe_2 band gap for an aligned structure only, posited from doping experiments and exciton dispersion calculations to be due to a moiré potential [221]. A third study again considered an aligned $WSe_2/MoSe_2$ heterobilayer. This showed PL with orders of magnitude lower line-widths for aligned structures than for previously reported iXs. These line-widths were on a scale comparable to those seen for quantum emitters in other 2D materials but also demonstrated a circular polarisation dependence; features that are expected for moiré excitons [222]. In all these works, type-II aligned heterostructures were studied with no band proximity, or resonance, between adjacent TMDCs.

The following sections outline work undertaken to probe exciton states in $WS_2/MoSe_2$ heterobilayers that resonantly hybridise at small angles. Initially, the theory for the hybridisation of these excitons is briefly introduced following "Ruiz et al., Phys. Rev. B 2019" [223], followed by the procedures that I used to fabricate such delicate devices and then the results obtained; all published in "Alexeev et al., Nature 2019" [224]. The heterostructures were fabricated in collaboration with M. Hamer, P. K. Nayak and S. Ahn and measured in collaboration with E. Alexeev and M. Molas.

6.2 Theory

As mentioned earlier, when two TMDCs are brought together, a type-II band alignment may occur. This is the case for the $WS_2/MoSe_2$ heterobilayer, with the global CBM and VBM occurring in the WS_2 and $MoSe_2$ layer, respectively; see Fig. 6.1a. Importantly, the CBM energy of both TMDCs have been reported to be closely matched, unlike many other TMDC combinations, with an energy differences $\sim$0.05eV [225–227]. As the CBM's are so close in energy, charge carrier hopping between bands is promoted, in turn encouraging hybridisation of excitonic states. For aligned monolayers ($\theta = 0°$), the momentum-space distance between the BZ corners of the two individual materials are minimised. However, as the two material lattice constants are not identical ($a_{MoSe_2} = 3.288$Å and

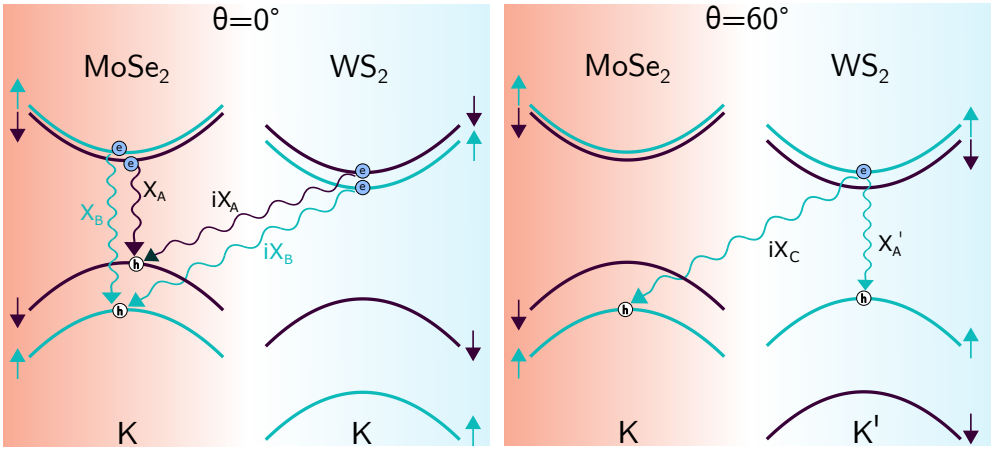

(a)

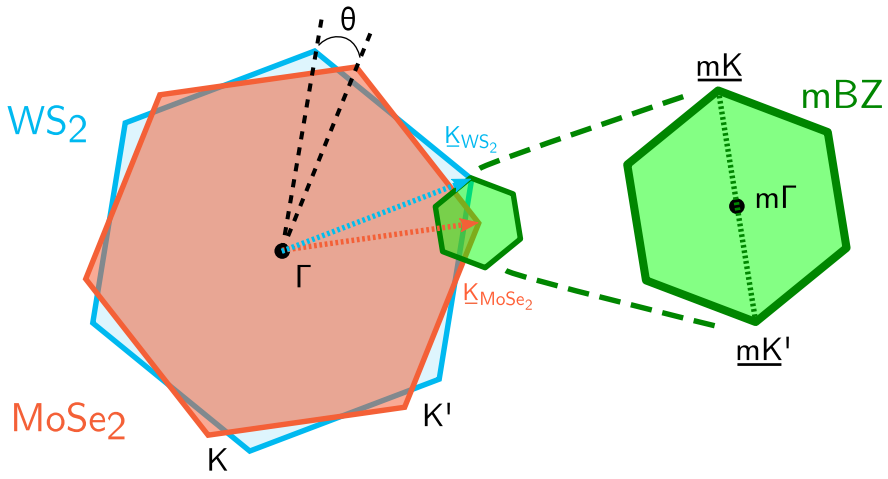

(b)

Figure 6.1: (a) The band alignment between BZ corners in the cases of aligned ($\theta = 0°$) and misaligned ($\theta = 60°$) heterobilayers of the WS_2 and $MoSe_2$ monolayers demonstrating the spin states and allowed transitions for intralayer (X) and interlayer (iX) excitons. and (b) the reciprocal space BZ alignment for twisted WS_2 and $MoSe_2$ monolayers creating a moiré BZ (mBZ) centred on the mΓ point with corners mK and mK′.

a_{WS_2} = 3.154Å [228]), the BZ's remain mismatched. As $MoSe_2$ has a larger lattice constant than WS_2, it's BZ occupies a smaller reciprocal space; see Fig. 6.1b. Hence, even when perfectly aligned, the valleys (K_{MoSe_2} and K_{WS_2}) are slightly offset from one another. As the lattice constants have a small mismatch, a moiré superlattice forms in real space with a corresponding moiré BZ (mBZ); at all twist angles. As the moiré superlattice period is dependent on the twist angle and lattice mismatch, so is the size of the mBZ. The mBZ, represented in

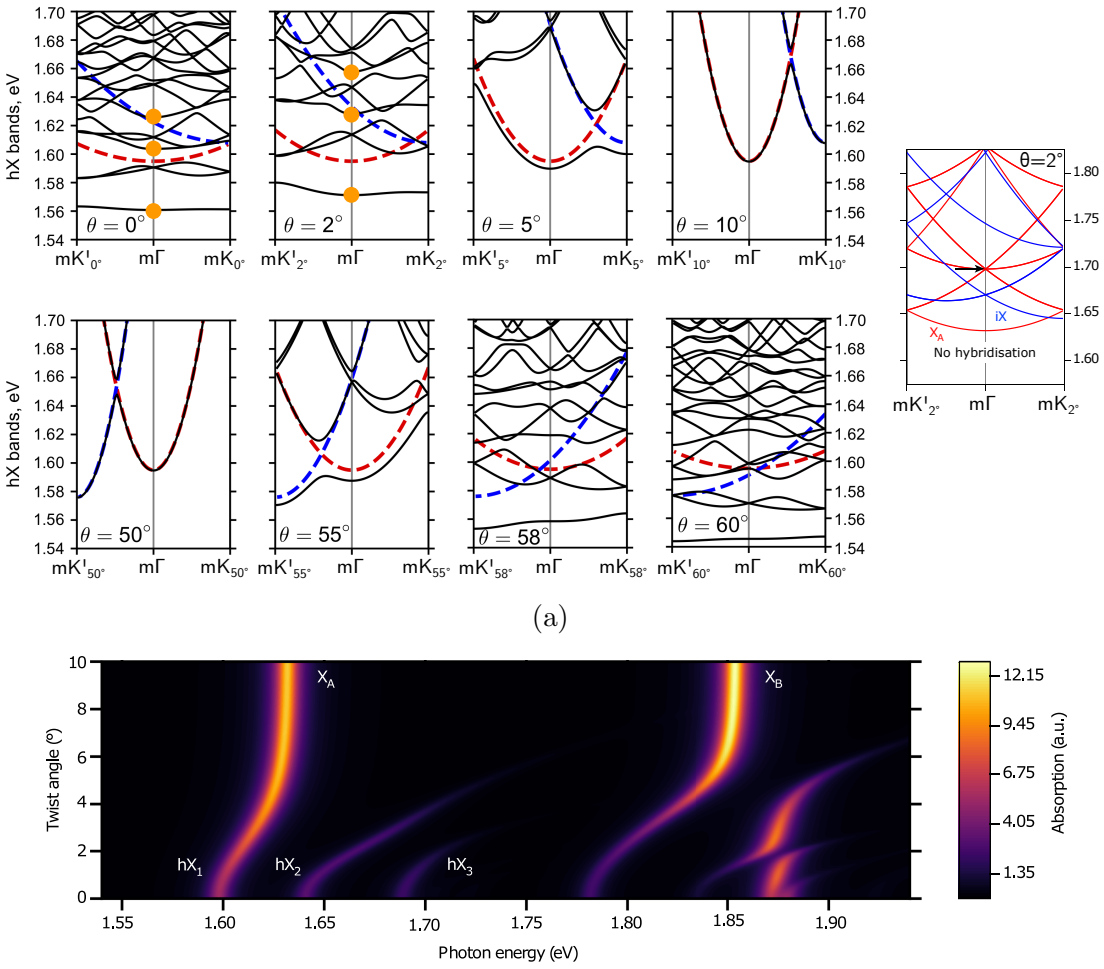

(a)

(b)

Figure 6.2: (a) Hybridised exciton bands along the mBZ for different twist angles close to alignment and anti-alignment. The intralayer (X) and interlayer (iX) exciton bands without tunnelling are given by the dashed red and blue lines, respectively, with optically active hybridised exciton states given by the orange markers. The right hand figure demonstrates the folding of the X_A bands in the mBZ without hybridisation. (b) Absorption spectra of the hybridised excitons for twist angles between 0° and 10°. At twist angles larger than ∼6°, the effect of hybridisation is negligible, leaving the X_A and X_B bands unaffected. For small angles, three bright hybridised excitons appear for the X_A and X_B bands, labelled as $hX_{1,2,3}$ for the X_A band. Adapted from image published in [224].

Fig. 6.1b, is centred (mΓ) on the $MoSe_2$ BZ K point with its edges ($\underline{mK}$ and $\underline{mK'} = -\underline{mK}$) denoted by the TMDC K-valley offset ($\underline{mK} = \underline{K}_{MoSe_2} - \underline{K}_{WS_2}$).

As with transitions in isolated TMDCs, heterobilayer interlayer transitions occur between states of the same spin; see Fig. 6.1a. Thus, the lowest energy

interlayer excitonic state (iX_A) is formed between spin down states in the CB and VB of WS_2 and $MoSe_2$, respectively. The next lowest energy state (iX_B) is formed between spin up states in the CB and VB of WS_2 and $MoSe_2$, respectively. The intralayer excitonic states in $MoSe_2$ (X_A and X_B) share conduction band energies similar to that of the interlayer states (iX_A and iX_B). The iXs have a lower binding energy than their intralayer counterparts (due to the increased out-of-plane separation), further boosting the resonance of the states. As a resonance is formed, electrons may hop between the excitonic states of the same spin, (i.e. between iX_A and X_A or iX_B and X_B), forming mixed, or hybridised, exciton states (hX_A and hX_B). This condition is similar for the anti-aligned case ($\theta = 60°$). Here, the valleys of one of the TMDCs are inverted, and with it the spin splitting of the bands. In this case, the lowest hybridised excitons states are suggested to be the same mixture of iX and X states as for the aligned case. However, it is suggested that another hybridised exciton (hX_C) may be formed between spin up WS_2 intralayer X'_A excitons and interlayer iX_C excitons (formed between spin up states in the K′-CB and K-VB of WS_2 and $MoSe_2$, respectively); see Fig. 6.1a.

The theoretical predictions of the exciton bands and absorption spectra for various twist angles are shown in Fig. 6.2. These calculations are described in full in [223, 224]. Briefly, as the twist angle decreases, the size of the mBZ also decreases with the X_A and iX_A bands (shown as the red and blue dashed lines respectively in Fig. 6.2a) crossing at lower energies closer to the mΓ point, progressively tuning toward the resonance. With this, the family of new resonantly hybridised excitonic states emerge, with the energy of the optically active hX's decreasing with twist angle. A similar process also occurs for the hX_B excitons. At larger angles, the bands cross at higher energies further from the mΓ point, resulting in a weaker interaction between the exciton states which leaves X_A unaffected. Interestingly, the third hybridised exciton state (denoted hX_3) is the result of hybridisation of the X_A band with the first folded X_A band into the mBZ. The folding of the X_A band into the mBZ is shown on the right hand side of Fig. 6.2a where the tunnelling between exciton states is disregarded and the arrow indicates the bands crossing at mΓ. This hybridised exciton, then, gives direct evidence of the crystallographic alignment on the excitonic states. [223]

Additionally, these hybridised exciton states are, by definition, composed of the interlayer and intralayer exciton states, and inherit properties from both of

these states. It has been suggested that the optical spectra of the hX's are dominated by the strong intralayer exciton properties; facilitating a strong oscillator strength and optical selection rules similar to that of the individual monolayers [223]. This is in contrast to the rules suggested to be imposed on moiré excitons by their stacking configurations [219, 220]. For moiré excitons, only interlayer or intralayer excitons are examined as neither the CBM's nor the VBM's between monolayers are considered to be resonant [218, 219]. The hybridised exciton states also contain an interlayer component. As such, they inherit an out-of-plane dipole moment due to the spatial separation of electrons and holes in the adjacent layers. This dipole moment may then couple to an out-of-plane electric field and shift in energy (Stark effect). Thus, in such a regime, the interlayer and intralayer excitonic states may be decoupled from the hybridised state, giving a possible route towards further proof of the existence of hybridised exciton states in $WS_2/MoSe_2$ heterobilayers. [223]

6.3 Fabrication

In this study, heterobilayers of monolayer $WS_2/MoSe_2$ were constructed through two methods. The first used chemical vapour deposition (CVD) growth of monolayers of $MoSe_2$ and WS_2 onto sapphire and SiO_2/Si substrates, respectively. The monolayers of $MoSe_2$ on sapphire were then transferred onto $WS_2/SiO_2/Si$ by the use of a PMMA membrane. This method of fabrication was not employed by myself, and more details of this technique are given in [224]. The second method for constructing heterobilayers used many of the techniques described earlier (Ch. 2) but with some key additional procedures.

As with other devices made for optical experiments, the heterobilayers were encapsulated in thin hBN ($\lesssim$ 5nm). Here, the hBN is pre-selected on a PMMA membrane as outlined in Ch. 2. A key difference in the fabrication of these heterostructures is that it's pivotal for them to not experience high temperatures (>100°C), to reduce thermal degradation of the $MoSe_2$ monolayer. With this guideline in place, annealing of the heterobilayer has not been employed, also hindering the formation of clean regions and the agglomeration of contamination into bubbles.

In an attempt to obtain a clean heterobilayer region without annealing, monolayers were exfoliated onto PMMA substrates. This is for two reasons. Firstly,

PMMA is suggested to leave less contamination on crystals than PPC. And secondly, large monolayer crystals may be more easily obtained on PMMA than, say, SiO_2/Si substrates. Large area monolayers ($\sim$100 µm^2) are required in order to obtain clear optical measurements from each region. Bulk WS_2 and $MoSe_2$ crystals were mechanically exfoliated with 'low-tack' tape onto a 90nm layer of PMMA spin-coated onto a Si substrate at 48°C. This exfoliation was performed in an argon filled glovebox. Monolayers were identified through bright-field and dark-field optical microscopy. Monolayer crystals with adjacent straight edges at 0°, 60° or 120° to one another, indicative of one of the crystallographic axes, were then chosen for transfer [40]. Figures 6.3a and 6.3b show optical images of WS_2 and $MoSe_2$ with dashed lines indicating crystal edges at 60° to one another. The

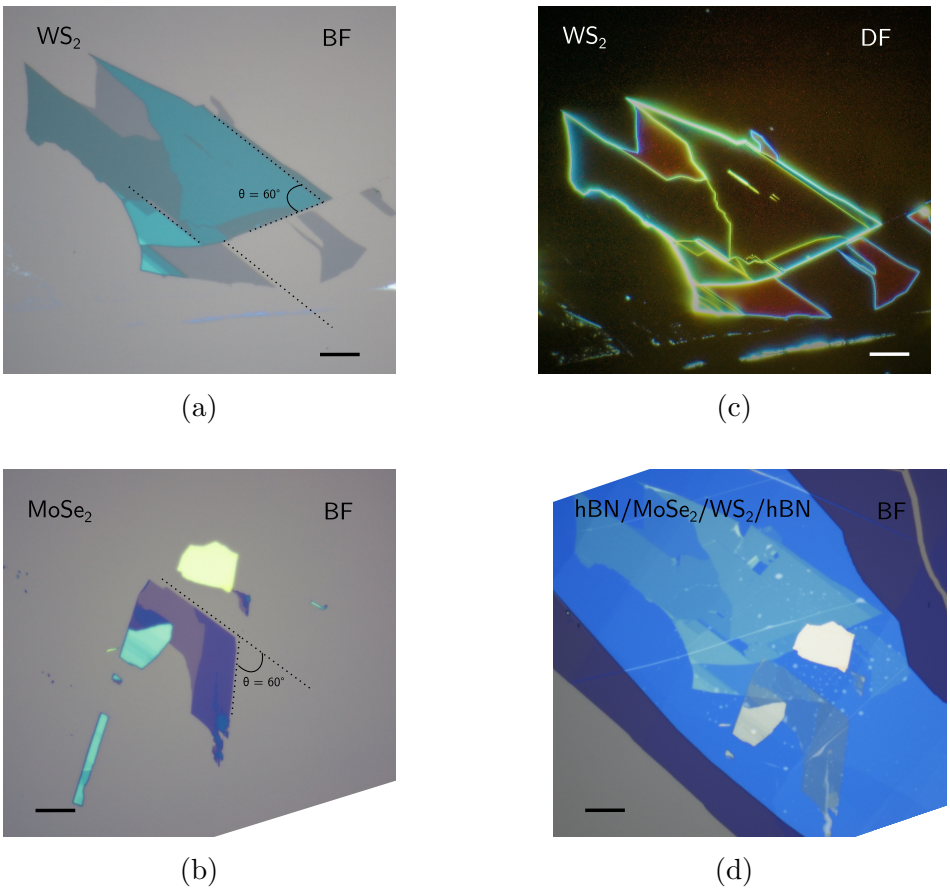

(a) (c)

(b) (d)

Figure 6.3: Optical images of the (a) WS_2 and (b) $MoSe_2$ terraced crystal with crystal edges at 60° to one another marked out with dashed lines, (c) a dark-field image of the same WS_2 crystal with monolayer regions demonstrating clear photoluminescence and (d) the encapsulated $WS_2/MoSe_2$ heterobilayer. Scale bar in all images is 10 µm.

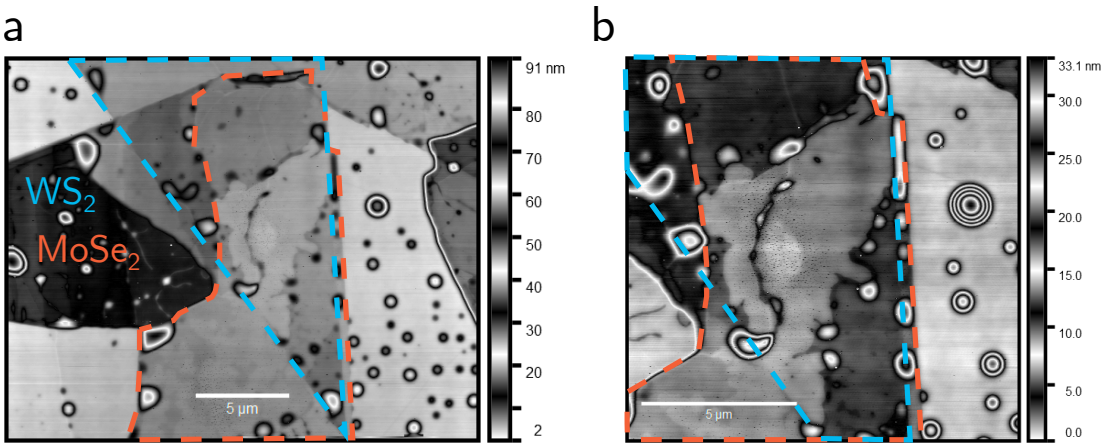

Figure 6.4: (a) and (b) Atomic force microscopy height maps of the hBN encapsulated $WS_2/MoSe_2$ heterobilayer region with monolayers of WS_2 and $MoSe_2$ outlined in dashed blue and orange lines, respectively.

monolayer edges alongside the dashed lines were those chosen to be aligned in one of the heterobilayer samples. Figure 6.3c shows a dark-field optical image of the same WS_2 crystal with monolayer regions displaying red PL. The monolayers were then picked up with hBN with their crystal edges aligned to an accuracy of $\sim 2°$. The hBN/$MoSe_2$/WS_2 was then finally placed down, using the dry-peel technique, onto another thin hBN crystal pre-exfoliated onto a SiO_2 (70nm)/Si substrate; resulting in a hBN/$MoSe_2$/WS_2/hBN encapsulated heterobilayer, see Fig. 6.3d. The use of thin hBN and a thin SiO_2 layer as substrate materials was to reduce the background interference signal in the reflectance contrast spectra, enhancing the clarity of the observable features.

Atomic force microscopy images of the encapsulated heterobilayer region are presented in Fig. 6.4. These demonstrate the formation of bubbles between hBN layers as well as the development of a largely flat, clean area in the central heterobilayer overlap region despite the lack of an annealing step.

6.4 SHG Characterisation of Heterobilayer Alignment

Initially, the alignment of the monolayers in the heterobilayers was probed through the use of polarisation-resolved SHG spectroscopy. As demonstrated earlier, this provides a non-invasive method for extracting the crystallographic

orientation of non-centrosymmetric crystals such as monolayer TMDCs. Figure 6.5 presents the polarisation-resolved SHG measurements for closely aligned and misaligned encapsulated heterobilayers. For the closely aligned heterobilayer, Fig. 6.5a, areas of each individual monolayer were selectable for measurement due to their sufficiently large lateral distance from their overlap region (see Fig. 6.3d), allowing for unambiguous probing using a laser spot size of ∼2 µm. Thus, the difference in polarisation angle between the two monolayers provides an adequately accurate indication of the twist angle; here (1.8±0.1)°. However, producing such laterally large heterobilayers with individual monolayer areas also available for probing, within the given fabrication constraints, is a technical challenge. Thus, most heterobilayer samples fabricated had only one individual monolayer region available for analysis; alongside the heterobilayer region. In this situation, one can still obtain the twist angle between the monolayers by assuming that the heterobilayer region inherits a superposition of the SHG signals from the monolayers. This has previously been demonstrated to be true for twisted bilayers of TMDCs [229]. From this, the difference in polarisation angle between a monolayer and a heterobilayer is doubled to give the twist angle. For the misaligned heterobilayer, the twist angle was found to be (12.2±0.2)°.

Interestingly, a spatial map of the total SHG intensity for the closely aligned

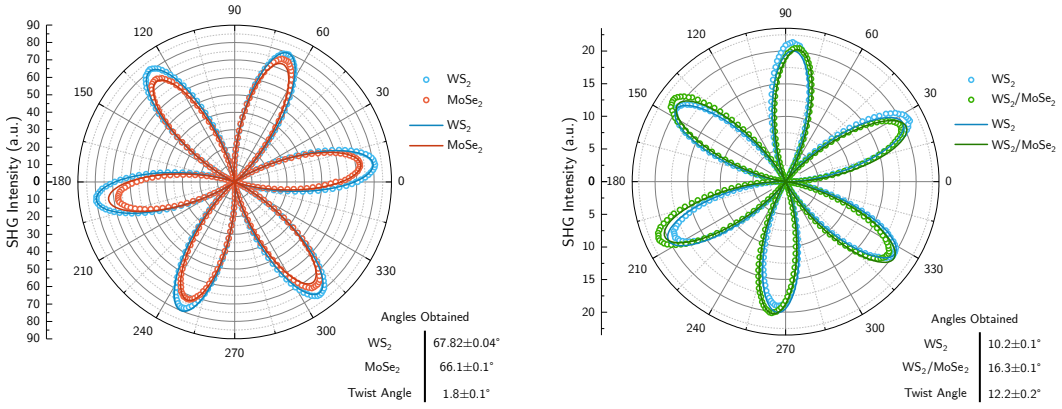

(a) (b)

Figure 6.5: Polar plots of polarisation-resolved SHG (in the parallel configuration) of (a) closely aligned and (b) misaligned mechanically exfoliated $WS_2/MoSe_2$ heterobilayer samples. The data is represented by hollow circles with a fitting of $r = A + C(\sin(3\theta + \psi))^2$ given by solid lines. A summary of the angles obtained is given in the bottom right of each figure. As published in [224].

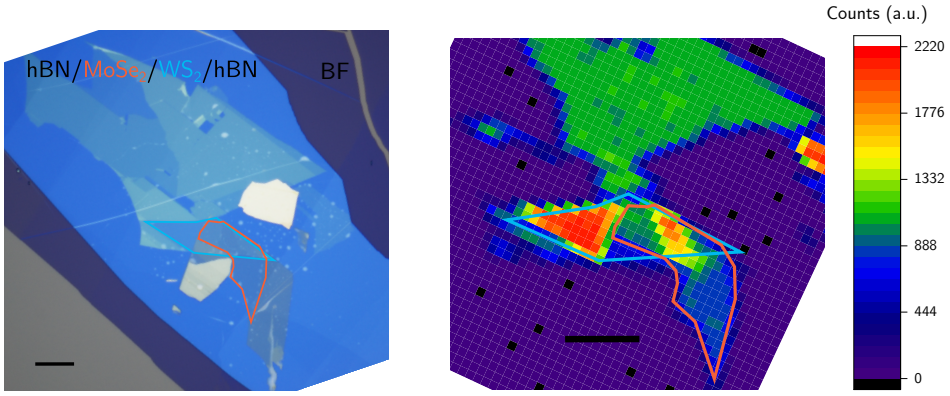

(a) (b)

Figure 6.6: (a) Optical image and (b) SHG intensity map of the $WS_2/MoSe_2$ heterobilayer. Regions of WS_2 and $MoSe_2$ monolayers are outlined in blue and orange lines, respectively. Scale bar in both images is 10 µm.

heterobilayer, presented in Fig. 6.6b, reveals the dependence of SHG on the crystal thickness; compare with Fig. 6.6a and Fig. 6.4. Thick TMDC crystals show negligible SHG signal with certain thinner crystals showing some intensity depending on their thickness. This is expected as even layers of TMDCs have been shown to have a negligible SHG signal, with odd layers progressively losing their intensity as they become thicker [151]. In the heterobilayer region, the SHG is most intense for the central, clean area, for reasons that are uncertain. However, the cleanliness of the interface clearly affects the SHG intensity of the heterobilayer. Additionally, while the SHG intensity is higher for the clean heterobilayer region, the PL intensity is significantly weaker; see Fig. 6.7. In this case, in the clean area, the monolayers are coupled more strongly, allowing for stronger recombination of the lower energy hybridised excitonic states which are beyond the filter edge for the image; appearing dark. The contaminated regions, however, have partially decoupled monolayers, allowing for the partial observation of higher energy $MoSe_2$ intralayer excitonic emission but reducing that from the WS_2 as the electrons in this layer are able to tunnel to form hybridised excitonic states.

6.5 PL and RC Studies

Initially, the PL and reflectance contrast (RC) measurements on the heterobilayers with various twist angles made from CVD grown monolayers, presented

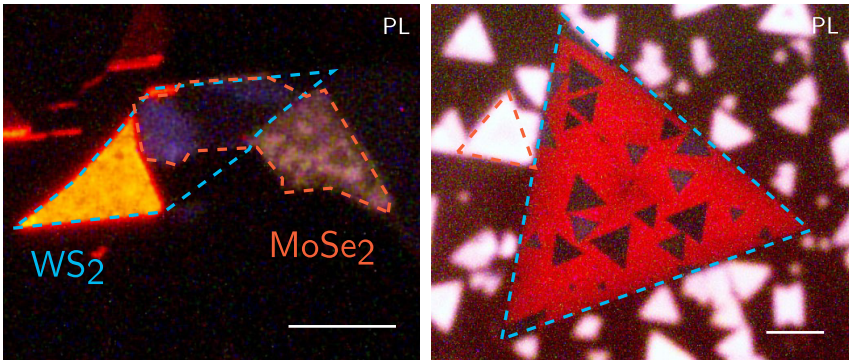

Figure 6.7: Photoluminescence images of heterobilayers fabricated by (a) mechanical exfoliation and dry transfer and (b) CVD growth and transfer. The photoluminescence is visible for both isolated monolayers but in the heterobilayer regions, it is quenched. Scale bar in both images is 10 µm. As published in [224].

in Fig. 6.8, are focussed on. Figure 6.8a displays the room temperature PL from CVD grown monolayers alongside that taken from a mechanically fabricated heterobilayer with a twist angle of $\theta = 2°$. The heterobilayer PL shows two peaks, labelled P1 and P2. The former is red-shifted by 57meV with respect to the $MoSe_2$ X_A exciton PL peak whilst the latter is at the same energy as the WS_2 X_A exciton PL peak. Figure 6.8b displays the RT P1 peak variation with twist angle for CVD fabricated heterobilayers. Interestingly, this peak demonstrates a strong dependence on the twist angle, decreasing for angles closer to alignment or anti-alignment, a summary is shown in Fig. 6.8c. This variation of the P1 peak energy with twist angle, with a particularly strong decrease close to the alignment and anti-alignment regimes, is suggested to be due to the formation of hybridised exciton states. As described earlier, these hybridised exciton states manifest close to alignment and anti-alignment, shifting the energy of the optically active exciton states. Figure 6.8d shows the LT RC spectra near the P1 peak energy of CVD fabricated heterobilayers at various angles. The lower temperature reduces spectral line-widths, aiding the identification of spectral features. Similar to the PL, a red-shift in the maximum derivative of the RC is observed for twist angles approaching alignment and anti-alignment. Also, at twist angles close to alignment or anti-alignment, faint new spectral features emerge. These new features are tentatively attributed to absorption from the hybridised exciton states (cf. Fig. 6.2b).

The LT PL and RC spectra for aligned and misaligned hBN encapsulated

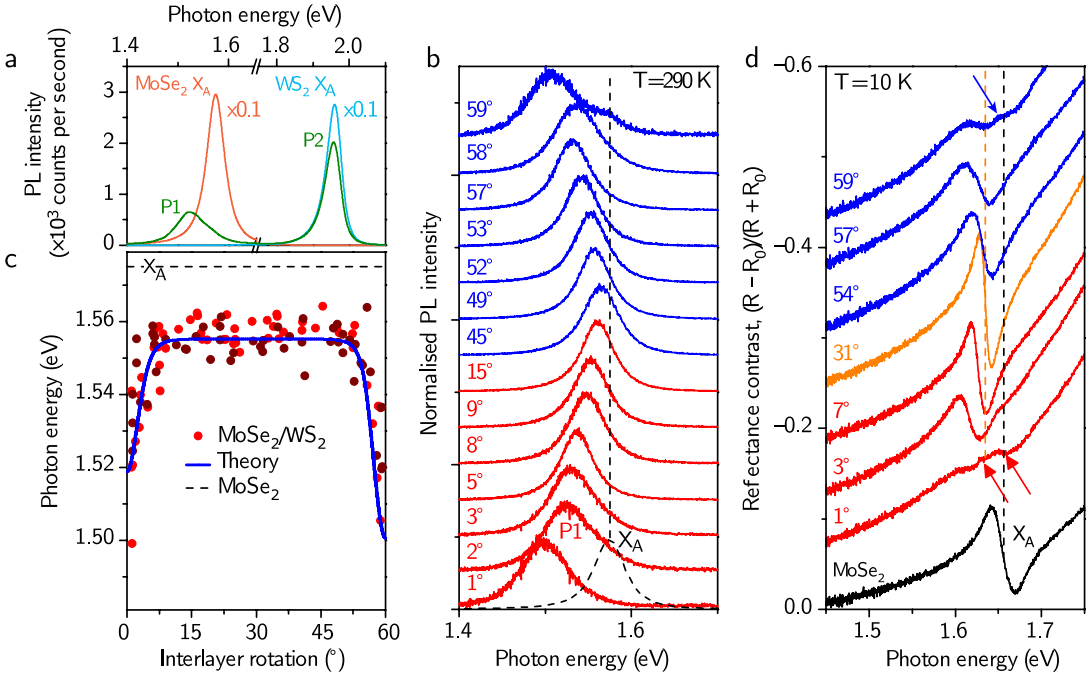

Figure 6.8: Photoluminescence and reflectance contrast spectra obtained from heterobilayers with various twist angles constructed from CVD grown monolayers of WS_2 and $MoSe_2$. (a) PL from isolated CVD grown monolayers (orange and blue) and mechanically exfoliated heterobilayer (green) with a twist angle $\theta = 2°$. (b) Normalised room temperature PL from P1 peak for CVD grown heterobilayers of various twist angles close to alignment and anti-alignment. The dashed spectra and line show the position of the isolated $MoSe_2$ X_a exciton PL peak. (c) The variation of the PL from P1 peak with interlayer rotation alongside the theoretical predictions for the energy of hybridised exciton states. (d) Low temperature RC spectra from heterobilayers of various twist angles close to alignment and anti-alignment. The RC spectra of $MoSe_2$ is shown in black for comparison reference. As published in [224].

$MoSe_2/WS_2$ heterobilayers constructed through mechanical exfoliation in a glovebox are presented in Fig. 6.9, where a significant enhancement in spectral clarity and resolution is immediately evident. This is suggested to be due to the fabrication of higher quality heterobilayers through the use of cleaner techniques. The upper graph in Fig. 6.9 presents normalised PL from the monolayer WS_2 region. This matches PL spectra previously reported for monolayer WS_2 with an exciton peak (denoted X_A), two trion peaks (denoted X_1^* and X_2^*) and lower energy peaks, suggested to be associated with localised excitons bound to impurities (denoted L_N), observable [216, 230]. The upper middle graph in Fig. 6.9 presents normalised PL spectra for a closely aligned ($\theta = 1.8°$) heterobilayer (red)

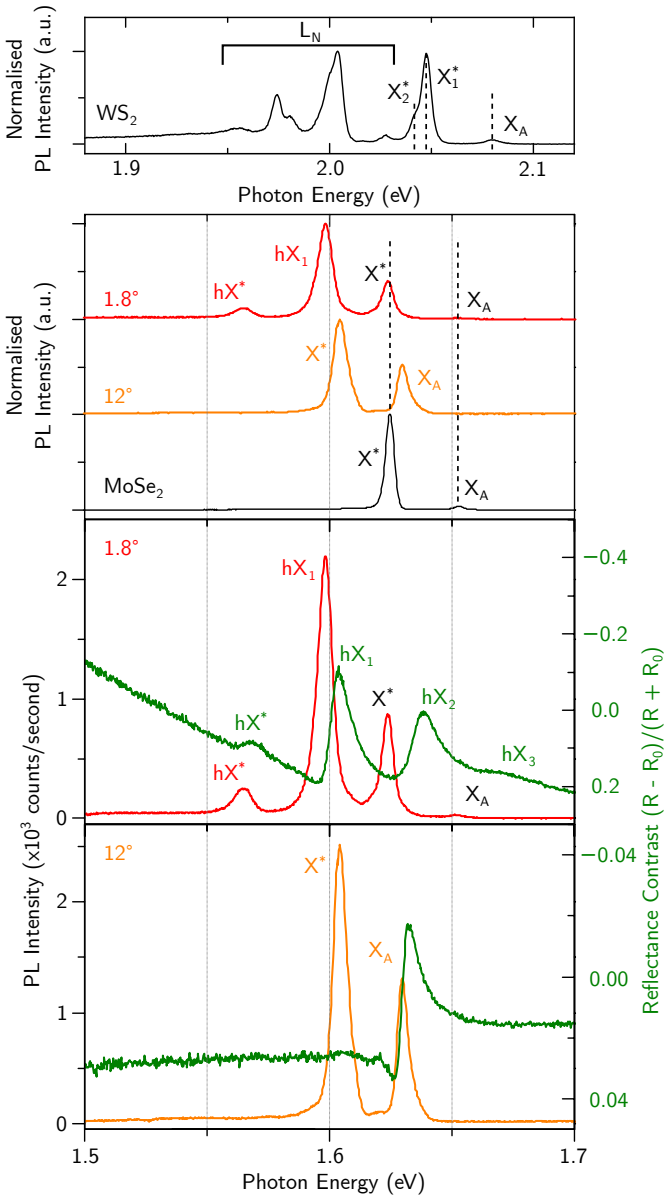

Figure 6.9: Low temperature (T=10K) photoluminescence and reflectance contrast spectra obtained from encapsulated $MoSe_2$ and WS_2 monolayers and heterobilayers fabricated with mechanically exfoliated monolayers of WS_2 and $MoSe_2$. Top: Normalised PL spectra for a WS_2 monolayer. Upper Middle: Normalised PL spectra for a closely aligned heterobilayer (red), a misaligned heterobilayer (orange) and a $MoSe_2$ monolayer (black) with peaks labelled as different excitons. The closely aligned heterobilayer (red) and $MoSe_2$ monolayer (black) spectra were obtained from the same sample. Lower Middle: PL (red) and RC (green) spectra for a closely aligned heterobilayer. Bottom: PL (orange) and RC (green) spectra for a misaligned heterobilayer. Adapted from image published in [224].

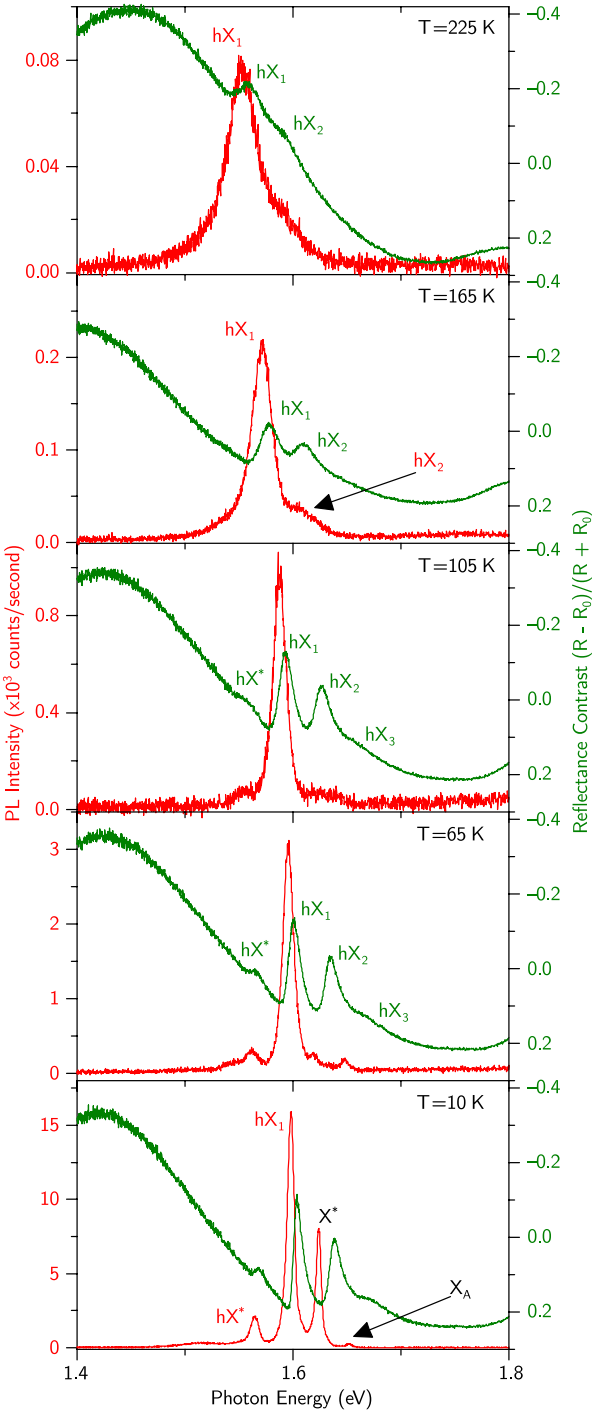

Figure 6.10: Photoluminescence (red) and reflectance contrast (green) spectra obtained at various temperatures for a closely aligned encapsulated heterobilayer fabricated with mechanically exfoliated monolayers of WS_2 and $MoSe_2$ (same sample in red in Fig. 6.9). Exciton peaks are labelled as in Fig. 6.9. As published in [224].

alongside a misaligned ($\theta = 12°$) heterobilayer (orange) and a $MoSe_2$ monolayer region (black) from the same sample as the aligned heterobilayer for reference. In the monolayer $MoSe_2$ PL spectrum, two salient peaks are visible and labelled as a trion (denoted X^*) and an exciton (denoted X_A) respectively; in agreement with previous PL studies on $MoSe_2$ monolayers [227, 231, 232]. A trion is a charged exciton, a quasiparticle formed through the addition of a charge to an exciton. Trions in $MoSe_2$ monolayers have been previously shown to be bright for PL measurements but nearly undetectable for RC measurements; an effect of the excess, or lack of, carriers available in either process [233–235]. This characteristic feature is observed in the PL and RC spectra for the monolayer $MoSe_2$ as well as for the misaligned heterobilayer; see the lower graph in Fig. 6.9.

Thus, despite red-shifts in the PL peaks of ∼20meV for the misaligned sample, they are suggested to be of trion and exciton origin. A similar red-shift is also observed for misaligned CVD fabricated heterobilayers (cf. Fig. 6.8). The aligned heterobilayer PL (red) also contains these two spectral features but lacking any red-shift, which is suspected to be due to the accumulation of strong PL from a monolayer $MoSe_2$ in a nearby region. Additionally, two other PL peaks at significantly red-shifted energies with respect to the misaligned heterobilayer PL are also observed. This is consistent with the trend observed in the CVD fabricated heterobilayers. These two PL peaks are suggested to originate from a hybridised exciton state as well as from another that is also bound to an extra charge carrier; labelled as hX_1 and hX^*, respectively. The RC spectra of the aligned heterobilayer (middle graph in Fig. 6.9), reveals four spectral features. The two lower energy features correlate directly to those of the hX PL peaks whilst the two higher energy features do not match those of the X^* and X_A peaks observed for monolayer $MoSe_2$. These higher energy spectral features are proposed to originate from the higher energy hybridised exciton states predicted in Fig. 6.2b, and hence labelled as hX_2 and hX_3. Further evidence of this is corroborated in Fig. 6.10 which demonstrates the temperature dependence of the PL (red) and RC (green) measurements for this aligned heterobilayer. As temperature increases from 10K to 65K, the X^* and X_A PL peaks vanish whilst all of the hX states in the RC spectrum remain. These hX features remain in the RC spectra up to 105K whilst in the PL spectra they progressively disappear; with the exception of the hX_2 peak that appears at 165K. From 10K to 225K, the strongest PL peak remains as hX_1 with a directly corresponding RC spectra

also following this continuous red-shift with temperature (an expected shift for a semiconductor). As hX_1 remains the brightest up to higher temperatures, the determination that the PL peak P1 in Fig. 6.8 originates from hybridised exciton states is further supported.

Overall, PL and RC measurements at various twist angles have provided initial evidence for the resonant hybridisation of interlayer and intralayer excitonic states in hBN encapsulated $MoSe_2/WS_2$ heterobilayers. This effect is observable as the CBM of both monolayer crystals are nearly degenerate, causing a resonant hopping of electrons when the two BZ's of the crystals are aligned in momentum-space.

6.6 Summary

In this chapter, the observations of resonantly hybridised excitons in a closely aligned TMDC/TMDC heterobilayer were given. The close proximity of the CB minima in energy and momentum-space for small twist angles promoted the hybridisation of the interlayer and intralayer states, revealing new states that inherit the properties of each excitonic component, in contrast to the properties predicted for 'moiré excitons'.

Chapter 7

Future Studies

Beyond the methods and results presented in the previous chapters, there are many more investigations that are possible to continue to improve our understanding of 2D materials and their heterostructures. In this chapter, some of these proposed investigations are given. Initially, further work on the fabrication of van der Waals heterostructures in an ultra-high vacuum is discussed. Then, further investigations to examine the optical properties of PTMCs and TMDC/PTMC heterostructures at low temperatures are considered. Further to this, the possibility of observing interlayer exciton condensation in TMDC/hBN/PTMC heterostructures is outlined. Afterwards, studies to confirm the existence of resonantly hybridised excitons in $MoSe_2/WS_2$ heterobilayers are suggested. Lastly, transport and electrical studies of PTMCs as well as the creation of type-I band alignment in van der Waals heterostructure are proposed.

7.1 Ultra-high Vacuum Fabrication

As introduced in Ch. 2, efforts to investigate the fabrication of van der Waals heterostructures under an ultra-high vacuum have begun at Manchester. The aim of the ultra-high vacuum system is to produce van der Waals heterostructures without using polymers or solvents which may introduce hydrocarbon contamination and reduce device quality. Within this overall effort, two particular aspects require further investigation and optimisation; 2D material exfoliation and transfer.

Mechanical exfoliation under an ultra-high vacuum, that aims to not use polymers, disallows for the standard techniques used thus far in van der Waals heterostructures. Neither tape nor direct manipulation of the 2D crystals with hand-held tweezers is possible. Thus, new techniques must be investigated. A possible method for exfoliating such materials is to use soft inorganic materials such as indium and various alloys. The 2D bulk crystal may be pre-loaded onto a soft metal and pressed into it. This may then be placed in the vacuum system, annealed and stamped onto a SiO_2 substrate with a mechanical press. The soft inorganic material should be selected so that its adhesive strength allows for cleaving of the 2D crystal.

Once bulk crystals are successfully exfoliated into thin crystals, they may then be selectively transferred using a new method that also does not rely on the use of polymers or hand-held tweezers. An inorganic material that mimics the properties of PMMA or PPC must be identified for this process. This material needs to be transparent, ideally flexible and have a similar adhesion strength to these polymers. A possible candidate is that of thin ($\sim$100nm) SiN films. These are transparent enough for crystal identification, are flexible, atomically flat and may have their adhesive strength altered through surface modification.

7.2 Low Temperature Optical Measurements on PTMCs

The optical properties of GaSe and InSe presented in Ch. 4 were reported for room temperature. Whilst this temperature still exhibits many interesting features, further investigations at low temperatures could reveal more. Thus far, no LT PL measurements have been systematically reported for hBN encapsulated few-layer GaSe or InSe crystals. Through these measurements, the exact origin of the PL observed at room temperature may be better understood, as well as potentially revealing further information about their band structures. To support this, absorption spectra may also be taken systematically via PLE and RC measurements. Moreover, LT Raman measurements may reveal Davydov splitting in few-layer GaSe and InSe crystals, as has been observed for their bulk counterparts [166–168]. Overall, these measurements would lay an important foundation for further work on PTMC-based van der Waals heterostructures.

7.3 Studies on TMDC/PTMC Heterostructures

Further to the previous section, continued LT optical measurements on TMDC-/PTMC heterostructures are suggested. Already, the possibility of band mixing between the materials has been demonstrated. However, further investigations into this phenomenon are possible. For example, the verification of this mixing may be achieved through the application of an electric field. By forming a graphene/hBN/PTMC/TMDC/hBN heterostructure, the interlayer excitons may be top and back gated. In this, one may be able to diminish the band mixing as well as tune the interlayer exciton energy or even create a light-emitting diode with an added graphene layer and the hBN layers acting as tunnelling barriers. Furthermore, the underlying mechanism for which charge carriers relax from the BZ corners to the centre may be explored further. Possible routes for analysis are time-resolved photoluminescence and pump-probe spectroscopy.

Another route of research is the use of other TMDCs and PTMCs for arranging more interlayer exciton energies. Other possible 2D semiconductors include GaSe, GaS, InS and $MoTe_2$. With these, it may be possible to obtain interlayer exciton energies in the telecommunications range, presenting them as potential candidates for 2D material integrated optical fibre technologies.

7.4 Γ Point Interlayer Exciton Condensation in TMDC/hBN/PTMC Heterostructures

Recently, interlayer exciton condensation was demonstrated for a graphene/h-BN/$MoSe_2$/hBN/WSe_2/hBN/graphene heterostructure up to temperatures of ∼100K [236]. The interlayer excitons, formed between the TMDC monolayers, were suggested to be able to condense because of their separation with 2-3 layer hBN; creating long lifetimes. By applying bias and gate voltages, the carrier density in each TMDC was also controllable; allowing for high carrier densities. A combination of these factors allowed for the observation of "electroluminescence [exhibiting] a threshold dependence on exciton density, a sensitive dependence on charge imbalance, and critical fluctuations, which are consistent with exciton condensation" [236]. Interestingly, this condensation was not observed for misaligned TMDCs, suggested to be because the large momentum of the interlayer excitons does not favour condensation. The newly discovered Γ-point interlayer

excitons reported here, inherently having minimum momentum, may also be able to form this condensate. A potential advantage is that no aligning is required, making fabrication easier.

7.5 Resonantly Hybridised Excitons

As discussed in Ch. 5, the resonantly hybridised excitons in $WS_2/MoSe_2$ heterobilayers are composed of interlayer and intralayer exciton states. As the interlayer exciton state has an out-of-plane dipole moment, it may couple to a similarly directed electric field and shift in energy. This, then, can allow for the decoupling of the exciton states and directly prove the existence of the hybridised exciton state.

To show this, one may construct an aligned, hBN encapsulated $WS_2/MoSe_2$ heterobilayer that demonstrates the hybridised exciton states. Then, a graphene layer may be transferred on top of the encapsulated heterobilayer and used alongside the underlying Si substrate to create an electric field across the device. The dependence of the absorption and PL spectra from the heterobilayer with electric field may then be observed.

7.6 Other Possible Investigations

7.6.1 Transport & Electrical Measurements of PTMCs

Transport measurements on few-layer GaSe may also be further investigated. Thus far, few-layer InSe has shown interesting properties, with the quantum hall effect and quantum confinement obtainable through graphene contacting and hBN encapsulation [94, 237]. Similar measurements may be possible for GaSe by also utilising hBN and graphene.

As reported in Ch. 1, the electronic band gaps for few-layer InSe and GaSe are either sparsely reported or not at all. Further investigations into these values would be beneficial for understanding the band structures and exciton binding energies in these crystals. This may be achieved through the use of STS spectroscopy, with the initial exfoliation performed under an UHV in order to protect the surfaces from oxidation and contamination.

7.6.2 Type-I Band Alignment in van der Waals Heterostructures

Thus far, the majority of van der Waals heterostructures involving 2D semiconductors form type-II band alignment. However, type-I alignment is also an important feature for modern optoelectronics, especially in LED technology [191]. By the use of wider band gap 2D materials (such as GaS) or careful doping of currently known 2D semiconductors, it may be possible to form atomically thin type-I band alignments. This has the potential to create more efficient van der Waals heterostructure devices, adding to the capabilities that 2D materials present.

Chapter 8

Conclusions

In this thesis the methods to exfoliate and protect air-sensitive materials through the use of a glovebox were given. This allowed for the fabrication of high quality van der Waals heterostructures that revealed new insights into the optical properties of few-layer air sensitive 2D materials and their heterostructures. Specifically, the lack of oxidation due to encapsulation enabled the observation of Raman and SHG for monolayer InSe and Raman and PL for few-layer GaSe crystals for the first time.

These isolated 2D semiconductors were then transferred onto one another to form type-II heterojunctions. These heterojunctions revealed new interlayer excitonic states with an energy that may be tuned by layer thickness selection. The recombination of these exciton states is suggested to be direct or quasi-direct in momentum-space around the Γ point, in contrast to previous attempts that demonstrated indirect interlayer excitonic states near the BZ corners. As this recombination is direct in momentum-space around the Γ point, the resultant luminescence remains bright without the need for crystal alignment. These interlayer excitonic states increase the spectral coverage available for van der Waals heterostructure design as well as allowing for further investigation of TMDCs.

Finally, the high quality fabrication methods presented here also enabled the first observation of resonantly hybridised excitons between two closely aligned TMDC monolayers. This gave direct evidence of the crystallographic alignment, revealing excitonic states that differ to those reported for 'moiré excitons'.

Overall, 2D materials present an accessible, exciting field of material research that continues to reveal new physical phenomena and show promise for future applications.

Bibliography

[1] P. Horowitz and W. Hill, *The Art of Electronics*. Cambridge: Cambridge University Press, 2015.

[2] A. K. Geim and I. V. Grigorieva, "Van der Waals heterostructures," *Nature*, vol. 499, no. 7459, pp. 419–425, 2013.

[3] K. S. Novoselov, A. K. Geim, S. V. Morozov, D. Jiang, Y. Zhang, S. V. Dubonos, I. V. Grigorieva, and A. A. Firsov, "Electric field effect in atomically thin carbon films," *Science*, vol. 306, no. 5696, pp. 666–669, 2004.

[4] "The Nobel Prize in Physics 2010." NobelPrize.org. Nobel Media AB 2019. Available at https://www.nobelprize.org/prizes/physics/2010/summary/, Accessed: 2019-06-12.

[5] A. H. Castro Neto, F. Guinea, N. M. R. Peres, K. S. Novoselov, and A. K. Geim, "The electronic properties of graphene," *Rev. Mod. Phys.*, vol. 81, pp. 109–162, 2009.

[6] C. Lee, X. Wei, J. W. Kysar, and J. Hone, "Measurement of the elastic properties and intrinsic strength of monolayer graphene," *Science*, vol. 321, no. 5887, pp. 385–388, 2008.

[7] M. I. Katsnelson, *Graphene: Carbon in Two Dimensions*. Cambridge: Cambridge University Press, 2012.

[8] K. Bolotin, K. Sikes, Z. Jiang, M. Klima, G. Fudenberg, J. Hone, P. Kim, and H. Stormer, "Ultrahigh electron mobility in suspended graphene," *Solid State Communications*, vol. 146, no. 9, pp. 351–355, 2008.

[9] K. S. Novoselov, A. K. Geim, S. V. Morozov, D. Jiang, M. I. Katsnelson, I. V. Grigorieva, S. V. Dubonos, and A. A. Firsov, "Two-dimensional gas of

massless dirac fermions in graphene," *Nature*, vol. 438, no. 7065, pp. 197–200, 2005.

[10] Y. B. Zhang, Y. W. Tan, H. L. Stormer, and P. Kim, "Experimental observation of the quantum Hall effect and Berry's phase in graphene," *Nature*, vol. 438, no. 7065, pp. 201–204, 2005.

[11] R. R. Nair, P. Blake, A. N. Grigorenko, K. S. Novoselov, T. J. Booth, T. Stauber, N. M. R. Peres, and A. K. Geim, "Fine structure constant defines visual transparency of graphene," *Science*, vol. 320, no. 5881, pp. 1308–1308, 2008.

[12] T. Ando, "Screening effect and impurity scattering in monolayer graphene," *Journal of the Physical Society of Japan*, vol. 75, no. 7, p. 074716, 2006.

[13] E. H. Hwang, S. Adam, and S. D. Sarma, "Carrier transport in two-dimensional graphene layers," *Physical Review Letters*, vol. 98, no. 18, p. 186806, 2007.

[14] J.-H. Chen, C. Jang, S. Xiao, M. Ishigami, and M. S. Fuhrer, "Intrinsic and extrinsic performance limits of graphene devices on SiO_2," *Nature Nanotechnology*, vol. 3, p. 206, 2008.

[15] J. Martin, N. Akerman, G. Ulbricht, T. Lohmann, J. H. Smet, K. von Klitzing, and A. Yacoby, "Observation of electron-hole puddles in graphene using a scanning single-electron transistor," *Nature Physics*, vol. 4, p. 144, 2007.

[16] S. V. Morozov, K. S. Novoselov, M. I. Katsnelson, F. Schedin, D. C. Elias, J. A. Jaszczak, and A. K. Geim, "Giant intrinsic carrier mobilities in graphene and its bilayer," *Physical Review Letters*, vol. 100, no. 1, p. 016602, 2008.

[17] E. V. Castro, H. Ochoa, M. Katsnelson, R. Gorbachev, D. Elias, K. Novoselov, A. Geim, and F. Guinea, "Limits on charge carrier mobility in suspended graphene due to flexural phonons," *Physical review letters*, vol. 105, no. 26, p. 266601, 2010.

[18] C. R. Dean, A. F. Young, I. Meric, C. Lee, L. Wang, S. Sorgenfrei, K. Watanabe, T. Taniguchi, P. Kim, K. L. Shepard, and J. Hone, "Boron

nitride substrates for high-quality graphene electronics," *Nature Nanotechnology*, vol. 5, no. 10, pp. 722–726, 2010.

[19] N. Ooi, V. Rajan, J. Gottlieb, Y. Catherine, and J. B. Adams, "Structural properties of hexagonal boron nitride," *Modelling and Simulation in Materials Science and Engineering*, vol. 14, no. 3, pp. 515–535, 2006.

[20] R. V. Gorbachev, I. Riaz, R. R. Nair, R. Jalil, L. Britnell, B. D. Belle, E. W. Hill, K. S. Novoselov, K. Watanabe, T. Taniguchi, A. K. Geim, and P. Blake, "Hunting for monolayer boron nitride: Optical and raman signatures," *Small*, vol. 7, no. 4, pp. 465–468, 2011.

[21] L. Banszerus, H. Janssen, M. Otto, A. Epping, T. Taniguchi, K. Watanabe, B. Beschoten, D. Neumaier, and C. Stampfer, "Identifying suitable substrates for high-quality graphene-based heterostructures," *2D Materials*, vol. 4, no. 2, p. 025030, 2017.

[22] M. Ishigami, J. H. Chen, W. G. Cullen, M. S. Fuhrer, and E. D. Williams, "Atomic structure of graphene on SiO_2," *Nano Letters*, vol. 7, no. 6, pp. 1643–1648, 2007.

[23] V. Sudarsan, A. K. Tyagi, and S. Banerjee, *Chapter 4 - Materials for Hostile Chemical Environments*, pp. 129–158. Amsterdam: Elsevier, 2017.

[24] L. Britnell, R. V. Gorbachev, R. Jalil, B. D. Belle, F. Schedin, M. I. Katsnelson, L. Eaves, S. V. Morozov, A. S. Mayorov, N. M. R. Peres, A. H. Castro Neto, J. Leist, A. K. Geim, L. A. Ponomarenko, and K. S. Novoselov, "Electron tunneling through ultrathin boron nitride crystalline barriers," *Nano Letters*, vol. 12, no. 3, pp. 1707–1710, 2012.

[25] A. Laturia, M. L. Van de Put, and W. G. Vandenberghe, "Dielectric properties of hexagonal boron nitride and transition metal dichalcogenides: from monolayer to bulk," *NPJ 2D Materials and Applications*, vol. 2, no. 1, p. 6, 2018.

[26] Y. Hattori, T. Taniguchi, K. Watanabe, and K. Nagashio, "Layer-by-layer dielectric breakdown of hexagonal boron nitride," *ACS Nano*, vol. 9, no. 1, pp. 916–921, 2015.

[27] S. M. Sze, *Physics of semiconductor devices*. Hoboken, N.J: Wiley-Interscience, 3rd ed., 2007.

[28] K. Watanabe, T. Taniguchi, and H. Kanda, "Direct-bandgap properties and evidence for ultraviolet lasing of hexagonal boron nitride single crystal," *Nature Materials*, vol. 3, no. 6, pp. 404–409, 2004.

[29] G. Cassabois, P. Valvin, and B. Gil, "Hexagonal boron nitride is an indirect bandgap semiconductor," *Nature Photonics*, vol. 10, p. 262, 2016.

[30] B. Arnaud, S. Lebgue, P. Rabiller, and M. Alouani, "Huge excitonic effects in layered hexagonal boron nitride," *Physical Review Letters*, vol. 96, no. 2, p. 026402, 2006.

[31] A. S. Mayorov, R. V. Gorbachev, S. V. Morozov, L. Britnell, R. Jalil, L. A. Ponomarenko, P. Blake, K. S. Novoselov, K. Watanabe, T. Taniguchi, and A. K. Geim, "Micrometer-scale ballistic transport in encapsulated graphene at room temperature," *Nano Letters*, vol. 11, no. 6, pp. 2396–2399, 2011.

[32] L. Wang, I. Meric, P. Y. Huang, Q. Gao, Y. Gao, H. Tran, T. Taniguchi, K. Watanabe, L. M. Campos, D. A. Muller, J. Guo, P. Kim, J. Hone, K. L. Shepard, and C. R. Dean, "One-dimensional electrical contact to a two-dimensional material," *Science*, vol. 342, no. 6158, pp. 614–617, 2013.

[33] A. V. Kretinin, Y. Cao, J. S. Tu, G. L. Yu, R. Jalil, K. S. Novoselov, S. J. Haigh, A. Gholinia, A. Mishchenko, M. Lozada, T. Georgiou, C. R. Woods, F. Withers, P. Blake, G. Eda, A. Wirsig, C. Hucho, K. Watanabe, T. Taniguchi, A. K. Geim, and R. V. Gorbachev, "Electronic properties of graphene encapsulated with different two-dimensional atomic crystals," *Nano Letters*, vol. 14, no. 6, pp. 3270–3276, 2014.

[34] Y. Cao, A. Mishchenko, G. L. Yu, E. Khestanova, A. P. Rooney, E. Prestat, A. V. Kretinin, P. Blake, M. B. Shalom, C. Woods, J. Chapman, G. Balakrishnan, I. V. Grigorieva, K. S. Novoselov, B. A. Piot, M. Potemski, K. Watanabe, T. Taniguchi, S. J. Haigh, A. K. Geim, and R. V. Gorbachev, "Quality heterostructures from two-dimensional crystals unstable in air by their assembly in inert atmosphere," *Nano Letters*, vol. 15, no. 8, pp. 4914–4921, 2015.

[35] F. Cadiz, E. Courtade, C. Robert, G. Wang, Y. Shen, H. Cai, T. Taniguchi, K. Watanabe, H. Carrere, D. Lagarde, M. Manca, T. Amand, P. Renucci, S. Tongay, X. Marie, and B. Urbaszek, "Excitonic linewidth approaching the homogeneous limit in MoS_2-based van der Waals heterostructures," *Physical Review X*, vol. 7, no. 2, p. 021026, 2017.

[36] T. Taniguchi and K. Watanabe, "Synthesis of high-purity boron nitride single crystals under high pressure by using Ba-BN solvent," *Journal of Crystal Growth*, vol. 303, no. 2, pp. 525–529, 2007.

[37] L. Schu, I. Stenger, F. Fossard, A. Loiseau, and J. Barjon, "Characterization methods dedicated to nanometer-thick hBN layers," *2D Materials*, vol. 4, no. 1, p. 015028, 2016.

[38] P. San-Jose, A. Gutirrez-Rubio, M. Sturla, and F. Guinea, "Spontaneous strains and gap in graphene on boron nitride," *Physical Review B*, vol. 90, no. 7, p. 075428, 2014.

[39] C. R. Woods, L. Britnell, A. Eckmann, R. S. Ma, J. C. Lu, H. M. Guo, X. Lin, G. L. Yu, Y. Cao, R. . Gorbachev, A. V. Kretinin, J. Park, L. A. Ponomarenko, M. I. Katsnelson, Y. . Gornostyrev, K. Watanabe, T. Taniguchi, C. Casiraghi, H. J. Gao, A. K. Geim, and K. . Novoselov, "Commensurate-incommensurate transition in graphene on hexagonal boron nitride," *Nature Physics*, vol. 10, p. 451, 2014.

[40] L. A. Ponomarenko, R. V. Gorbachev, G. L. Yu, D. C. Elias, R. Jalil, A. A. Patel, A. Mishchenko, A. S. Mayorov, C. R. Woods, J. R. Wallbank, M. Mucha-Kruczynski, B. A. Piot, M. Potemski, I. V. Grigorieva, K. S. Novoselov, F. Guinea, V. I. Fal'ko, and A. K. Geim, "Cloning of dirac fermions in graphene superlattices," *Nature*, vol. 497, p. 594, 2013.

[41] B. Hunt, J. D. Sanchez-Yamagishi, A. F. Young, M. Yankowitz, B. J. LeRoy, K. Watanabe, T. Taniguchi, P. Moon, M. Koshino, P. Jarillo-Herrero, and R. C. Ashoori, "Massive dirac fermions and hofstadter butterfly in a van der Waals heterostructure," *Science*, vol. 340, no. 6139, p. 1427, 2013.

[42] M. Chhowalla, H. S. Shin, G. Eda, L.-J. Li, K. P. Loh, and H. Zhang, "The chemistry of two-dimensional layered transition metal dichalcogenide nanosheets," *Nat Chem*, vol. 5, no. 4, pp. 263–275, 2013.

[43] I. Verzhbitskiy, G. Eda, T. Nakato, J. Kawamata, and S. Takagi, *Chalcogenide Nanosheets: Optical Signatures of Many-Body Effects and Electronic Band Structure*, pp. 133–162. Tokyo: Springer Japan, 2017.

[44] Q. H. Wang, K. Kalantar-Zadeh, A. Kis, J. N. Coleman, and M. S. Strano, "Electronics and optoelectronics of two-dimensional transition metal dichalcogenides," *Nature nanotechnology*, vol. 7, no. 11, p. 699, 2012.

[45] K. F. Mak, C. Lee, J. Hone, J. Shan, and T. F. Heinz, "Atomically thin MoS_2: A new direct-gap semiconductor," *Physical Review Letters*, vol. 105, no. 13, p. 136805, 2010.

[46] A. Splendiani, L. Sun, Y. Zhang, T. Li, J. Kim, C.-Y. Chim, G. Galli, and F. Wang, "Emerging photoluminescence in monolayer MoS_2," *Nano Letters*, vol. 10, no. 4, pp. 1271–1275, 2010.

[47] B. Radisavljevic, A. Radenovic, J. Brivio, V. Giacometti, and A. Kis, "Single-layer MoS_2 transistors," *Nature Nanotechnology*, vol. 6, p. 147, 2011.

[48] S. Ahmed and J. Yi, "Two-dimensional transition metal dichalcogenides and their charge carrier mobilities in field-effect transistors," *Nano-Micro Letters*, vol. 9, no. 4, p. 50, 2017.

[49] S. Manzeli, D. Ovchinnikov, D. Pasquier, O. V. Yazyev, and A. Kis, "2D transition metal dichalcogenides," *Nature Reviews Materials*, vol. 2, p. 17033, 2017.

[50] F. Withers, O. Del Pozo-Zamudio, A. Mishchenko, A. P. Rooney, A. Gholinia, K. Watanabe, T. Taniguchi, S. J. Haigh, A. K. Geim, A. I. Tartakovskii, and K. S. Novoselov, "Light-emitting diodes by band-structure engineering in van der Waals heterostructures," *Nature Materials*, vol. 14, no. 3, pp. 301–306, 2015.

[51] O. Lopez-Sanchez, D. Lembke, M. Kayci, A. Radenovic, and A. Kis, "Ultrasensitive photodetectors based on monolayer MoS_2," *Nature Nanotechnology*, vol. 8, p. 497, 2013.

[52] E. Cappelluti, R. Roldán, J. A. Silva-Guillén, P. Ordejón, and F. Guinea, "Tight-binding model and direct-gap/indirect-gap transition in single-layer and multilayer mos_2," *Phys. Rev. B*, vol. 88, p. 075409, 2013.

[53] G.-B. Liu, D. Xiao, Y. Yao, X. Xu, and W. Yao, "Electronic structures and theoretical modelling of two-dimensional group-VIB transition metal dichalcogenides," *Chemical Society Reviews*, vol. 44, no. 9, pp. 2643–2663, 2015.

[54] A. Kormányos, G. Burkard, M. Gmitra, J. Fabian, V. Zólyomi, N. D. Drummond, and V. Fal'ko, "Corrigendum: k.p theory for two-dimensional transition metal dichalcogenide semiconductors," *2D Materials*, vol. 2, no. 4, p. 049501, 2015.

[55] H. Schmidt, F. Giustiniano, and G. Eda, "Electronic transport properties of transition metal dichalcogenide field-effect devices: surface and interface effects," *Chem. Soc. Rev.*, vol. 44, pp. 7715–7736, 2015.

[56] W. Zhao, R. M. Ribeiro, and G. Eda, "Electronic structure and optical signatures of semiconducting transition metal dichalcogenide nanosheets," *Accounts of Chemical Research*, vol. 48, no. 1, pp. 91–99, 2015.

[57] G. Wang, A. Chernikov, M. M. Glazov, T. F. Heinz, X. Marie, T. Amand, and B. Urbaszek, "Colloquium: Excitons in atomically thin transition metal dichalcogenides," *Reviews of Modern Physics*, vol. 90, no. 2, p. 021001, 2018.

[58] K. K. Kam and B. A. Parkinson, "Detailed photocurrent spectroscopy of the semiconducting group VIB transition metal dichalcogenides," *The Journal of Physical Chemistry*, vol. 86, no. 4, pp. 463–467, 1982.

[59] D. Xiao, G.-B. Liu, W. Feng, X. Xu, and W. Yao, "Coupled spin and valley physics in monolayers of MoS_2 and other group-VI dichalcogenides," *Physical Review Letters*, vol. 108, no. 19, p. 196802, 2012.

[60] H. Yu, W. Yao, P. Avouris, T. Low, and T. F. Heinz, *Valley-Spin Physics in 2D Semiconducting Transition Metal Dichalcogenides*, pp. 279–294. Cambridge: Cambridge University Press, 2017.

[61] Y. M. Koroteev, G. Bihlmayer, J. E. Gayone, E. V. Chulkov, S. Blügel, P. M. Echenique, and P. Hofmann, "Strong spin-orbit splitting on bi surfaces," *Phys. Rev. Lett.*, vol. 93, p. 046403, 2004.

[62] S. LaShell, B. A. McDougall, and E. Jensen, "Spin splitting of an au(111) surface state band observed with angle resolved photoelectron spectroscopy," *Physical Review Letters*, vol. 77, no. 16, pp. 3419–3422, 1996.

[63] M. Dresselhaus, G. Dresselhaus, and A. Jorio, *Group Theory.* Berlin, Heidelberg: Springer Berlin Heidelberg, 2008.

[64] Z. Y. Zhu, Y. C. Cheng, and U. Schwingenschlgl, "Giant spin-orbit-induced spin splitting in two-dimensional transition-metal dichalcogenide semiconductors," *Physical Review B*, vol. 84, no. 15, p. 153402, 2011.

[65] K. Kośmider, J. W. Gonzlez, and J. Fernández-Rossier, "Large spin splitting in the conduction band of transition metal dichalcogenide monolayers," *Physical Review B*, vol. 88, no. 24, p. 245436, 2013.

[66] G.-B. Liu, W.-Y. Shan, Y. Yao, W. Yao, and D. Xiao, "Three-band tight-binding model for monolayers of group-VIB transition metal dichalcogenides," *Physical Review B*, vol. 88, no. 8, p. 085433, 2013.

[67] T. Cao, G. Wang, W. Han, H. Ye, C. Zhu, J. Shi, Q. Niu, P. Tan, E. Wang, B. Liu, and J. Feng, "Valley-selective circular dichroism of monolayer molybdenum disulphide," *Nature Communications*, vol. 3, p. 887, 2012.

[68] J. J. Sakurai, *Modern quantum mechanics.* Addison-Wesley, revised ed., 1994.

[69] I. Souza and D. Vanderbilt, "Dichroic f-sum rule and the orbital magnetization of crystals," *Physical Review B*, vol. 77, no. 5, p. 054438, 2008.

[70] Z. M. Wang, *MoS_2 : Materials, Physics, and Devices.* Lecture Notes in Nanoscale Science and Technology, 21, Cham: Springer International Publishing, 2014.

[71] G.-B. Liu, H. Pang, Y. Yao, and W. Yao, "Intervalley coupling by quantum dot confinement potentials in monolayer transition metal dichalcogenides," *New Journal of Physics*, vol. 16, no. 10, p. 105011, 2014.

[72] M. Dyakonov, *Basics of Semiconductor and Spin Physics*, vol. 157. Berlin, Heidelberg: Springer, 2008.

[73] H. Kamimura and K. Nakao, "Band structures and optical properties of semiconducting layer compounds GaS and GaSe," *Journal of the Physical Society of Japan*, vol. 24, no. 6, pp. 1313–1325, 1968.

[74] O. Del Pozo-Zamudio, S. Schwarz, J. Klein, R. C. Schofield, E. A. Chekhovich, O. Ceylan, E. Margapoti, A. I. Dmitriev, G. V. Lashkarev, D. N. Borisenko, N. N. Kolesnikov, J. J. Finley, and A. I. Tartakovskii, "Photoluminescence and raman investigation of stability of InSe and GaSe thin films," 2015.

[75] A. Gouskov, J. Camassel, and L. Gouskov, "Growth and characterization of III-VI layered crystals like GaSe, GaTe, InSe, $GaSe_{1-x}Te_x$ and $Ga_xIn_{1-x}Se$," *Progress in Crystal Growth and Characterization*, vol. 5, no. 4, pp. 323–413, 1982.

[76] D. V. Rybkovskiy, N. R. Arutyunyan, A. S. Orekhov, I. A. Gromchenko, I. V. Vorobiev, A. V. Osadchy, E. Y. Salaev, T. K. Baykara, K. R. Allakhverdiev, and E. D. Obraztsova, "Size-induced effects in gallium selenide electronic structure: The influence of interlayer interactions," *Physical Review B*, vol. 84, no. 8, p. 085314, 2011.

[77] V. Zólyomi, N. D. Drummond, and V. I. Fal'ko, "Electrons and phonons in single layers of hexagonal indium chalcogenides from ab initio calculations," *Physical Review B*, vol. 89, no. 20, 2014.

[78] A. Kuhn, R. Chevalier, and A. Rimsky, "Atomic structure of a 4h GaSe polytype named δ-type," *Acta Crystallographica Section B*, vol. 31, no. 12, pp. 2841–2842, 1975.

[79] S. Nagel, A. Baldereschi, and K. Maschke, "Tight-binding study of the electronic states in GaSe polytypes," *Journal of Physics C: Solid State Physics*, vol. 12, no. 9, p. 1625, 1979.

[80] J. V. McCanny and R. B. Murray, "The band structures of gallium and indium selenide," *Journal of Physics C: Solid State Physics*, vol. 10, no. 8, p. 1211, 1977.

[81] D. J. Late, B. Liu, H. S. S. R. Matte, C. N. R. Rao, and V. P. Dravid, "Rapid characterization of ultrathin layers of chalcogenides on SiO_2/Si substrates," *Advanced Functional Materials*, vol. 22, no. 9, pp. 1894–1905, 2012.

[82] G. W. Mudd, S. A. Svatek, T. Ren, A. Patanè, O. Makarovsky, L. Eaves, P. H. Beton, Z. D. Kovalyuk, G. V. Lashkarev, Z. R. Kudrynskyi, and A. I. Dmitriev, "Tuning the bandgap of exfoliated InSe nanosheets by quantum confinement," *Advanced Materials*, vol. 25, no. 40, pp. 5714–5718, 2013.

[83] N. C. Fernelius, "Properties of gallium selenide single crystal," *Progress in Crystal Growth and Characterization of Materials*, vol. 28, no. 4, pp. 275–353, 1994.

[84] J. Srour, M. Badawi, F. E. H. Hassan, and A. Postnikov, "Comparative study of structural and electronic properties of GaSe and InSe polytypes," *The Journal of Chemical Physics*, vol. 149, no. 5, p. 054106, 2018.

[85] D. E. Bode and H. Levinstein, "Photoconductivity of indium selenide," *Journal of the Optical Society of America*, vol. 43, no. 12, pp. 1209–1210, 1953.

[86] J. Camassel, P. Merle, H. Mathieu, and A. Chevy, "Excitonic absorption edge of indium selenide," *Physical Review B*, vol. 17, no. 12, pp. 4718–4725, 1978.

[87] P. A. Hu, Z. Z. Wen, L. F. Wang, P. H. Tan, and K. Xiao, "Synthesis of few-layer GaSe nanosheets for high performance photodetectors," *ACS Nano*, vol. 6, no. 7, pp. 5988–5994, 2012.

[88] S. J. Magorrian, V. Zólyomi, and V. I. Fal'ko, "Electronic and optical properties of two-dimensional InSe from a DFT-parametrized tight-binding model," *Physical Review B*, vol. 94, no. 24, p. 245431, 2016.

[89] X. Zhou, J. X. Cheng, Y. B. Zhou, T. Cao, H. Hong, Z. M. Liao, S. W. Wu, H. L. Peng, K. H. Liu, and D. P. Yu, "Strong second-harmonic generation in atomic layered GaSe," *Journal of the American Chemical Society*, vol. 137, no. 25, pp. 7994–7997, 2015.

[90] L. Karvonen, A. Saynatjoki, S. Mehravar, R. D. Rodriguez, S. Hartmann, D. R. T. Zahn, S. Honkanen, R. A. Norwood, N. Peyghambarian, K. Kieu,

H. Lipsanen, and J. Riikonen, "Investigation of second- and third-harmonic generation in few-layer gallium selenide by multiphoton microscopy," *Scientific Reports*, vol. 5, 2015.

[91] S. Deckoff-Jones, J. J. Zhang, C. E. Petoukhoff, M. K. L. Man, S. D. Lei, R. Vajtai, P. M. Ajayan, D. Talbayev, J. Madeo, and K. M. Dani, "Observing the interplay between surface and bulk optical nonlinearities in thin van der Waals crystals," *Scientific Reports*, vol. 6, 2016.

[92] J. M. Auerhammer and E. R. Eliel, "Frequency doubling of mid-infrared radiation in gallium selenide," *Optics Letters*, vol. 21, no. 11, pp. 773–775, 1996.

[93] G. B. Abdullaev, K. R. Allakhverdiev, L. A. Kulevskii, A. M. Prokhorov, E. Y. Salaev, A. D. Savelev, and V. V. Smirnov, "Parametric conversion of infrared radiation in GaSe crystal," *Kvantovaya Elektronika*, vol. 2, no. 6, pp. 1228–1233, 1975.

[94] D. A. Bandurin, A. V. Tyurnina, G. L. Yu, A. Mishchenko, V. Zólyomi, S. V. Morozov, R. K. Kumar, R. V. Gorbachev, Z. R. Kudrynskyi, S. Pezzini, Z. D. Kovalyuk, U. Zeitler, K. S. Novoselov, A. Patanè, L. Eaves, I. V. Grigorieva, V. I. Fal'ko, A. K. Geim, and Y. Cao, "High electron mobility, quantum Hall effect and anomalous optical response in atomically thin InSe," *Nature Nanotechnology*, vol. 12, no. 3, pp. 223–227, 2017.

[95] V. Zólyomi, N. D. Drummond, and V. I. Fal'ko, "Band structure and optical transitions in atomic layers of hexagonal gallium chalcogenides," *Physical Review B*, vol. 87, no. 19, p. 195403, 2013.

[96] G. W. Mudd, M. R. Molas, X. Chen, V. Zólyomi, K. Nogajewski, Z. R. Kudrynskyi, Z. D. Kovalyuk, G. Yusa, O. Makarovsky, L. Eaves, M. Potemski, V. I. Fal'ko, and A. Patanè, "The direct-to-indirect band gap crossover in two-dimensional van der Waals indium selenide crystals," *Scientific Reports*, vol. 6, p. 39619, 2016.

[97] A. Morales-García, R. Valero, and F. Illas, "An empirical, yet practical way to predict the band gap in solids by using density functional band structure calculations," *The Journal of Physical Chemistry C*, vol. 121, no. 34, pp. 18862–18866, 2017.

[98] S. J. Magorrian, *Theory of Electronic and Optical Properties of Atomically Thin Films of Indium Selenide*. PhD thesis, The University of Manchester, 2019.

[99] P. Gomes da Costa, R. G. Dandrea, R. F. Wallis, and M. Balkanski, "First-principles study of the electronic structure of γ-InSe and β-InSe," *Physical Review B*, vol. 48, no. 19, pp. 14135–14141, 1993.

[100] M. J. Hamer, J. Zultak, A. V. Tyurnina, V. Zólyomi, D. Terry, A. Barinov, A. Garner, J. Donoghue, A. P. Rooney, V. Kandyba, A. Giampietri, A. Graham, N. Teutsch, X. Xia, M. Koperski, S. J. Haigh, V. I. Fal'ko, R. V. Gorbachev, and N. R. Wilson, "Indirect to direct gap crossover in two-dimensional InSe revealed by angle-resolved photoemission spectroscopy," *ACS nano*, vol. 13, no. 2, pp. 2136–2142, 2019.

[101] M. V. Andriyashik, M. Y. Sakhnovskii, V. B. Timofeev, and A. S. Yakimova, "Optical transitions in the spectra of the fundamental absorption and reflection of InSe single crystals," *physica status solidi (b)*, vol. 28, no. 1, pp. 277–285, 1968.

[102] E. Aulich, J. L. Brebner, and E. Mooser, "Indirect energy gap in GaSe and GaS," *physica status solidi (b)*, vol. 31, no. 1, pp. 129–131, 1969.

[103] X. F. Li, M. W. Lin, A. A. Puretzky, J. C. Idrobo, C. Ma, M. F. Chi, M. Yoon, C. M. Rouleau, I. I. Kravchenko, D. B. Geohegan, and K. Xiao, "Controlled vapor phase growth of single crystalline, two-dimensional GaSe crystals with high photoresponse," *Scientific Reports*, vol. 4, 2014.

[104] H. Henck, D. Pierucci, J. Zribi, F. Bisti, E. Papalazarou, J.-C. Girard, J. Chaste, F. Bertran, P. Le Fvre, F. Sirotti, L. Perfetti, C. Giorgetti, A. Shukla, J. E. Rault, and A. Ouerghi, "Evidence of direct electronic band gap in two-dimensional van der Waals indium selenide crystals," *Physical Review Materials*, vol. 3, no. 3, p. 034004, 2019.

[105] P. K. Larsen, S. Chiang, and N. V. Smith, "Determination of the valence band structure of InSe by angle-resolved photoemission using synchrotron radiation," *Physical Review B*, vol. 15, no. 6, pp. 3200–3210, 1977.

[106] Z. Ben Aziza, H. Henck, D. Pierucci, M. G. Silly, E. Lhuillier, G. Patriarche, F. Sirotti, M. Eddrief, and A. Ouerghi, "van der Waals epitaxy of GaSe/graphene heterostructure: Electronic and interfacial properties," *ACS Nano*, vol. 10, no. 10, pp. 9679–9686, 2016.

[107] G. Lévêque, "Direct display of the valence-band dispersion in ultraviolet photoemission spectroscopy: Application to GaSe," *Review of scientific instruments*, vol. 59, no. 6, pp. 859–861, 1988.

[108] M. O. D. Camara, A. Mauger, and I. Devos, "Electronic structure of the layer compounds GaSe and InSe in a tight-binding approach," *Physical Review B*, vol. 65, no. 12, p. 125206, 2002.

[109] Z. Ben Aziza, D. Pierucci, H. Henck, M. G. Silly, C. David, M. Yoon, F. Sirotti, K. Xiao, M. Eddrief, J.-C. Girard, and A. Ouerghi, "Tunable quasiparticle band gap in few-layer GaSe/graphene van der Waals heterostructures," *Physical Review B*, vol. 96, no. 3, p. 035407, 2017.

[110] Z. Ben Aziza, V. Zólyomi, H. Henck, D. Pierucci, M. G. Silly, J. Avila, S. J. Magorrian, J. Chaste, C. Chen, M. Yoon, K. Xiao, F. Sirotti, M. C. Asensio, E. Lhuillier, M. Eddrief, V. I. Fal'ko, and A. Ouerghi, "Valence band inversion and spin-orbit effects in the electronic structure of monolayer GaSe," *Physical Review B*, vol. 98, no. 11, p. 115405, 2018.

[111] G. A. Akhundov, N. A. Gasanova, and M. A. Nizametdinova, "Optical absorption, reflection, and dispersion of GaS and GaSe layer crystals," *physica status solidi (b)*, vol. 15, no. 2, pp. K109–K113, 1966.

[112] R. H. Bube and E. L. Lind, "Photoconductivity of gallium selenide crystals," *Physical Review*, vol. 115, no. 5, pp. 1159–1164, 1959.

[113] C. S. Jung, F. Shojaei, K. Park, J. Y. Oh, H. S. Im, D. M. Jang, J. Park, and H. S. Kang, "Red-to-ultraviolet emission tuning of two-dimensional gallium sulfide/selenide," *ACS Nano*, vol. 9, no. 10, pp. 9585–9593, 2015.

[114] S. J. Magorrian, V. Zólyomi, and V. I. Fal'ko, "Spin-orbit coupling, optical transitions, and spin pumping in monolayer and few-layer InSe," *Physical Review B*, vol. 96, no. 19, p. 195428, 2017.

[115] M. Zastrow, "Meet the crystal growers who sparked a revolution in graphene electronics.," *Nature*, vol. 572, pp. 429–432, 2019.

[116] K. Kokh, Y. M. Andreev, V. Svetlichnyi, G. Lanskii, and A. Kokh, "Growth of GaSe and GaS single crystals," *Crystal Research and Technology*, vol. 46, no. 4, pp. 327–330, 2011.

[117] J. Guo, J.-J. Xie, D.-J. Li, G.-L. Yang, F. Chen, C.-R. Wang, L.-M. Zhang, Y. M. Andreev, K. A. Kokh, G. V. Lanskii, and V. A. Svetlichnyi, "Doped GaSe crystals for laser frequency conversion," *Light: Science and Applications*, vol. 4, p. e362, 2015.

[118] J. F. Molloy, *Solid Solution $GaSe_{1-x}S_x$ Single Crystals for THz Generation.* PhD thesis, Heriot-Watt University, 2016.

[119] M. S. A. Bhuyan, M. N. Uddin, M. M. Islam, F. A. Bipasha, and S. S. Hossain, "Synthesis of graphene," *International Nano Letters*, vol. 6, no. 2, pp. 65–83, 2016.

[120] Y. Huang, E. Sutter, N. N. Shi, J. Zheng, T. Yang, D. Englund, H.-J. Gao, and P. Sutter, "Reliable exfoliation of large-area high-quality flakes of graphene and other two-dimensional materials," *ACS Nano*, vol. 9, no. 11, pp. 10612–10620, 2015.

[121] P. Blake, E. Hill, A. Castro Neto, K. Novoselov, D. Jiang, R. Yang, T. Booth, and A. Geim, "Making graphene visible," *Applied physics letters*, vol. 91, no. 6, p. 063124, 2007.

[122] F. Pizzocchero, L. Gammelgaard, B. S. Jessen, J. Caridad, L. Wang, J. Hone, P. Bøggild, and T. Booth, "The hot pick-up technique for batch assembly of van der Waals heterostructures," *Nature Communications*, vol. 7, p. 11894, 2016.

[123] R. Frisenda, E. Navarro-Moratalla, P. Gant, D. P. De Lara, P. Jarillo-Herrero, R. V. Gorbachev, and A. Castellanos-Gomez, "Recent progress in the assembly of nanodevices and van der Waals heterostructures by deterministic placement of 2D materials," *Chemical Society Reviews*, vol. 47, no. 1, pp. 53–68, 2018.

[124] J. Gao, B. Li, J. Tan, P. Chow, T.-M. Lu, and N. Koratkar, "Aging of transition metal dichalcogenide monolayers," *ACS Nano*, vol. 10, no. 2, pp. 2628–2635, 2016.

[125] Q. Li, Q. Zhou, L. Shi, Q. Chen, and J. Wang, "Recent advances in oxidation and degradation mechanisms of ultrathin 2D materials under ambient conditions and their passivation strategies," *J. Mater. Chem. A*, vol. 7, pp. 4291–4312, 2019.

[126] B. Huang, G. Clark, E. Navarro-Moratalla, D. R. Klein, R. Cheng, K. L. Seyler, D. Zhong, E. Schmidgall, M. A. McGuire, D. H. Cobden, W. Yao, D. Xiao, P. Jarillo-Herrero, and X. Xu, "Layer-dependent ferromagnetism in a van der Waals crystal down to the monolayer limit," *Nature*, vol. 546, no. 7657, p. 270, 2017.

[127] D. Shcherbakov, P. Stepanov, D. Weber, Y. Wang, J. Hu, Y. Zhu, K. Watanabe, T. Taniguchi, Z. Mao, W. Windl, J. Goldberger, M. Bockrath, and C. N. Lau, "Raman spectroscopy, photocatalytic degradation, and stabilization of atomically thin chromium tri-iodide," *Nano Letters*, vol. 18, no. 7, pp. 4214–4219, 2018.

[128] S. I. Drapak, S. V. Gavrylyuk, Z. D. Kovalyuk, and O. S. Lytvyn, "Native oxide emerging of the cleavage surface of gallium selenide due to prolonged storage," *Semiconductors*, vol. 42, no. 4, pp. 414–421, 2008.

[129] T. E. Beechem, B. M. Kowalski, M. T. Brumbach, A. E. McDonald, C. D. Spataru, S. W. Howell, T. Ohta, J. A. Pask, and N. G. Kalugin, "Oxidation of ultrathin GaSe," *Applied Physics Letters*, vol. 107, no. 17, 2015.

[130] V. M. Katerynchuk and Z. D. Kovalyuk, "Surface morphology and electrical resistance of the oxide film on InSe," *Inorganic Materials*, vol. 47, no. 7, pp. 749–752, 2011.

[131] O. A. Balitskii, V. P. Savchyn, and V. O. Yukhymchuk, "Raman investigation of InSe and GaSe single-crystals oxidation," *Semiconductor Science and Technology*, vol. 17, no. 2, p. L1, 2002.

[132] J. F. Sánchez-Royo, G. Muñoz-Matutano, M. Brotons-Gisbert, J. I. Martínez-Pastor, A. Segura, A. Cantarero, R. G. Mata, J. Canet-Ferrer,

G. Tobias, E. Canadell, J. Marques-Hueso, and B. D. Gerardot, "Electronic structure, optical properties, and lattice dynamics in atomically thin indium selenide flakes," *Nano Research*, vol. 7, pp. 1556–1568, 2014.

[133] G. W. Mudd, A. Patanè, Z. R. Kudrynskyi, M. W. Fay, O. Makarovsky, L. Eaves, Z. D. Kovalyuk, V. Zólyomi, and V. Fal'ko, "Quantum confined acceptors and donors in InSe nanosheets," *Applied Physics Letters*, vol. 105, no. 22, p. 221909, 2014.

[134] D. Rhodes, S. H. Chae, R. Ribeiro-Palau, and J. Hone, "Disorder in van der Waals heterostructures of 2D materials," *Nature materials*, vol. 18, no. 6, p. 541, 2019.

[135] S. Haigh, A. Gholinia, R. Jalil, S. Romani, L. Britnell, D. Elias, K. Novoselov, L. Ponomarenko, A. Geim, and R. Gorbachev, "Cross-sectional imaging of individual layers and buried interfaces of graphene-based heterostructures and superlattices," *Nature materials*, vol. 11, no. 9, p. 764, 2012.

[136] E. Khestanova, F. Guinea, L. Fumagalli, A. Geim, and I. Grigorieva, "Universal shape and pressure inside bubbles appearing in van der Waals heterostructures," *Nature communications*, vol. 7, p. 12587, 2016.

[137] M. R. Rosenberger, H.-J. Chuang, K. M. McCreary, A. T. Hanbicki, S. V. Sivaram, and B. T. Jonker, "Nano-'squeegee' for the creation of clean 2D material interfaces," *ACS applied materials & interfaces*, vol. 10, no. 12, pp. 10379–10387, 2018.

[138] C. Kittel, *Introduction to Solid State Physics*. Wiley, 8th ed., 2004.

[139] C. Klingshirn, *Semiconductor Optics*. Graduate Texts in Physics, Springer Berlin Heidelberg, 2012.

[140] P. Yu and M. Cardona, *Fundamentals of Semiconductors: Physics and Materials Properties*. Graduate Texts in Physics, Springer Berlin Heidelberg, 2010.

[141] R. Cox, V. Huard, K. Kheng, S. Lovisa, R. Miller, K. Saminadayar, A. Arnoult, J. Cibert, S. Tatarenko, and M. Potemski, "Exciton trions

in II-VI heterostructures," *Acta Physica Polonica A*, vol. 94, no. 2, pp. 99–109, 1998.

[142] G. New, *Introduction to Nonlinear Optics*. Cambridge University Press, 2011.

[143] G. D. Stucky, S. R. Marder, and J. E. Sohn, *Linear and Nonlinear Polarizability*, ch. 1, pp. 2–30. American Chemical Society, 1991.

[144] R. Powell, *Symmetry, Group Theory, and the Physical Properties of Crystals*. Lecture Notes in Physics, Springer New York, 2010.

[145] M. Cardona and G. Güntherodt, *Light scattering in solids II: basic concepts and instrumentation*. Topics in applied physics, Springer-Verlag, 1982.

[146] L. D. Landau, *The classical theory of fields*, vol. 2. Elsevier, 2013.

[147] A. Autere, H. Jussila, Y. Dai, Y. Wang, H. Lipsanen, and Z. Sun, "Nonlinear optics with 2D layered materials," *Advanced Materials*, vol. 30, no. 24, p. 1705963, 2018.

[148] R. W. Boyd, *Nonlinear Optics, Third Edition*. Academic Press, Inc., 3rd ed., 2008.

[149] Y. R. Shen, "Optical second harmonic generation at interfaces," *Annual Review of Physical Chemistry*, vol. 40, no. 1, pp. 327–350, 1989.

[150] T. F. Heinz, "Second-order nonlinear optical effects at surfaces and interfaces," in *Modern Problems in Condensed Matter Sciences*, vol. 29, pp. 353–416, Elsevier, 1991.

[151] Y. Li, Y. Rao, K. F. Mak, Y. You, S. Wang, C. R. Dean, and T. F. Heinz, "Probing symmetry properties of few-layer MoS_2 and h-BN by optical second-harmonic generation," *Nano Letters*, vol. 13, no. 7, pp. 3329–3333, 2013.

[152] R. M. Hoff, J. Irwin, and R. Lieth, "Raman scattering in GaSe," *Canadian Journal of Physics*, vol. 53, no. 17, pp. 1606–1614, 1975.

[153] Y. Tang, K. C. Mandal, J. A. McGuire, and C. W. Lai, "Layer-and frequency-dependent second harmonic generation in reflection from GaSe atomic crystals," *Physical Review B*, vol. 94, no. 12, p. 125302, 2016.

[154] P. R. J. Ed, *CRC Handbook of Lasers - with Selected Data on Optical Technology*. Chemical Rubber Co., 1971.

[155] T. F. Heinz, M. M. T. Loy, and W. A. Thompson, "Study of symmetry and disordering of Si(111)-7 x 7 surfaces by optical second harmonic generation," *Journal of Vacuum Science Technology B: Microelectronics and Nanometer Structures*, vol. 3, pp. 1467–1470, 1985.

[156] L. M. Malard, T. V. Alencar, A. P. M. Barboza, K. F. Mak, and A. M. de Paula, "Observation of intense second harmonic generation from MoS_2 atomic crystals," *Phys. Rev. B*, vol. 87, p. 201401, 2013.

[157] N. Leisgang, J. G. Roch, G. Froehlicher, M. Hamer, D. Terry, R. Gorbachev, and R. J. Warburton, "Optical second harmonic generation in encapsulated single-layer InSe," *AIP Advances*, vol. 8, no. 10, p. 105120, 2018.

[158] C. Weisbuch and B. Vinter, *Quantum semiconductor structures: fundamentals and applications*. San Diego: Academic Press, 1991.

[159] J. McIntyre and D. Aspnes, "Differential reflection spectroscopy of very thin surface films," *Surface Science*, vol. 24, no. 2, pp. 417 – 434, 1971.

[160] K. Dhakal, D. Duong, J. Lee, H. Nam, M. Kim, M. Kan, Y. Lee, and J. Kim, "Confocal absorption spectral imaging of MoS_2: optical transitions depending on the atomic thickness of intrinsic and chemically doped MoS_2.," *Nanoscale*, vol. 6, no. 21, p. 13028, 2014.

[161] D. J. Terry, V. Zólyomi, M. Hamer, A. V. Tyurnina, D. G. Hopkinson, A. M. Rakowski, S. J. Magorrian, N. Clark, Y. M. Andreev, O. Kazakova, K. Novoselov, S. J. Haigh, V. I. Fal'ko, and R. V. Gorbachev, "Infrared-to-violet tunable optical activity in atomic films of GaSe, InSe, and their heterostructures," *2D Materials*, vol. 5, no. 4, p. 041009, 2018.

[162] M. R. Molas, A. V. Tyurnina, V. Zólyomi, A. Ott, D. J. Terry, M. J. Hamer, C. Yelgel, A. G. Nasibulin, A. C. Ferrari, V. I. Fal'ko, and R. Gorbachev, "Raman spectroscopy of atomically thin GaSe and InSe crystals," *Under review*, 2019.

[163] N. M. Gasanly, B. M. Yavadov, V. I. Tagirov, and E. A. Vinogradov, "Infrared and raman spectra of layer InSe single crystals," *physica status solidi (b)*, vol. 89, no. 1, pp. K43–K48, 1978.

[164] N. Kuroda and Y. Nishina, "Resonant raman scattering at higher M_0 exciton edge in layer compound InSe," *Solid State Communications*, vol. 28, no. 6, pp. 439–443, 1978.

[165] R. M. Hoff, *Raman scattering in GaSe.* PhD thesis, Simon Fraser University. Theses (Dept. of Physics), 1975.

[166] K. Allakhverdiev, E. Y. Salaev, M. Tagyev, S. Babaev, and L. Genzel, "Davydov doublets in Raman spectra of ϵ-GaSe," *Solid state communications*, vol. 59, no. 3, pp. 133–136, 1986.

[167] H. Yoshida, S. Nakashima, and A. Mitsuishi, "Phonon raman spectra of layer compound GaSe," *physica status solidi (b)*, vol. 59, no. 2, pp. 655–666, 1973.

[168] S. Jandl and C. Carlone, "Raman spectrum of crystalline InSe," *Solid State Communications*, vol. 25, no. 1, pp. 5–8, 1978.

[169] I.-H. Choi and P. Y. Yu, "Properties of phase-pure InSe films prepared by metalorganic chemical vapor deposition with a single-source precursor," *Journal of Applied Physics*, vol. 93, no. 8, pp. 4673–4677, 2003.

[170] S. Ashokan, K. Jain, M. Balkanski, and C. Julien, "Resonant raman scattering in quasi-two-dimensional InSe near the M_0 and M_1 critical points," *Physical Review B*, vol. 44, no. 20, p. 11133, 1991.

[171] Z. Chen, K. Gacem, M. Boukhicha, J. Biscaras, and A. Shukla, "Anodic bonded 2D semiconductors: from synthesis to device fabrication," *Nanotechnology*, vol. 24, no. 41, p. 415708, 2013.

[172] J. Zhou, J. Shi, Q. Zeng, Y. Chen, L. Niu, F. Liu, T. Yu, K. Suenaga, X. Liu, J. Lin, and Z. Liu, "InSe monolayer: synthesis, structure and ultrahigh second-harmonic generation," *2D Materials*, vol. 5, no. 2, p. 025019, 2018.

[173] G. Froehlicher, E. Lorchat, O. Zill, M. Romeo, and S. Berciaud, "Rigid-layer raman-active modes in n-layer transition metal dichalcogenides: interlayer force constants and hyperspectral raman imaging," *Journal of Raman Spectroscopy*, vol. 49, no. 1, pp. 91–99, 2017.

[174] L. Liang, J. Zhang, B. G. Sumpter, Q.-H. Tan, P.-H. Tan, and V. Meunier, "Low-frequency shear and layer-breathing modes in raman scattering of two-dimensional materials," *ACS nano*, vol. 11, no. 12, pp. 11777–11802, 2017.

[175] A. Chernikov, T. C. Berkelbach, H. M. Hill, A. Rigosi, Y. Li, O. B. Aslan, D. R. Reichman, M. S. Hybertsen, and T. F. Heinz, "Exciton binding energy and nonhydrogenic rydberg series in monolayer WS_2," *Physical review letters*, vol. 113, no. 7, p. 076802, 2014.

[176] D. G. Hopkinson, V. Zólyomi, A. P. Rooney, N. Clark, D. J. Terry, M. Hamer, D. J. Lewis, C. S. Allen, A. I. Kirkland, Y. Andreev, Z. Kudrynskyi, Z. Kovalyuk, A. Patanè, V. I. Fal'ko, R. Gorbachev, and S. J. Haigh, "Formation and healing of defects in atomically thin GaSe and InSe," *ACS nano*, vol. 13, no. 5, pp. 5112–5123, 2019.

[177] Q. Hao, H. Yi, H. Su, B. Wei, Z. Wang, Z. Lao, Y. Chai, Z. Wang, C. Jin, J. Dai, and W. Zhang, "Phase identification and strong second harmonic generation in pure ϵ-InSe and its alloys," *Nano Letters*, vol. 19, no. 4, pp. 2634–2640, 2019.

[178] R. M. Hoff and J. C. Irwin, "Resonant raman scattering in GaSe," *Phys. Rev. B*, vol. 10, pp. 3464–3470, 1974.

[179] V. Sobolev and V. Donetskich, "Reflectivity spectra of GaSe and inse crystals," *physica status solidi (b)*, vol. 45, no. 1, pp. K15–K19, 1971.

[180] D. J. Late, B. Liu, J. Luo, A. Yan, H. R. Matte, M. Grayson, C. Rao, and V. P. Dravid, "GaS and GaSe ultrathin layer transistors," *Advanced Materials*, vol. 24, no. 26, pp. 3549–3554, 2012.

[181] L. Quan, Y. Song, Y. Lin, G. Zhang, Y. Dai, Y. Wu, K. Jin, H. Ding, N. Pan, Y. Luo, and X. Wang, "The raman enhancement effect on a thin GaSe flake and its thickness dependence," *J. Mater. Chem. C*, vol. 3, pp. 11129–11134, 2015.

[182] R. Longuinhos and J. Ribeiro-Soares, "Ultra-weak interlayer coupling in two-dimensional gallium selenide," *Phys. Chem. Chem. Phys.*, vol. 18, pp. 25401–25408, 2016.

[183] O. Del Pozo-Zamudio, S. Schwarz, M. Sich, I. A. Akimov, M. Bayer, R. C. Schofield, E. A. Chekhovich, B. J. Robinson, N. D. Kay, O. V. Kolosov, A. I. Dmitriev, G. V. Lashkarev, D. N. Borisenko, N. N. Kolesnikov, and A. I. Tartakovskii, "Photoluminescence of two-dimensional GaTe and GaSe films," *2d Materials*, vol. 2, no. 3, 2015.

[184] Y. Wu, D. Zhang, K. Lee, G. S. Duesberg, A. Syrlybekov, X. Liu, M. Abid, M. Abid, Y. Liu, L. Zhang, C. . Coilein, H. Xu, J. Cho, M. Choi, B. S. Chun, H. Wang, H. Liu, and H.-C. Wu, "Quantum confinement and gas sensing of mechanically exfoliated GaSe," *Advanced Materials Technologies*, vol. 2, no. 1, p. 1600197, 2017.

[185] D. Andres-Penares, A. Cros, J. P. Martinez-Pastor, and J. F. Sanchez-Royo, "Quantum size confinement in gallium selenide nanosheets: band gap tunability versus stability limitation," *Nanotechnology*, vol. 28, no. 17, 2017.

[186] M. Rahaman, R. D. Rodriguez, M. Monecke, S. A. Lopez-Rivera, and D. R. T. Zahn, "GaSe oxidation in air: from bulk to monolayers," *Semiconductor Science and Technology*, vol. 32, no. 10, 2017.

[187] J. Susoma, J. Lahtinen, M. Kim, J. Riikonen, and H. Lipsanen, "Crystal quality of two-dimensional gallium telluride and gallium selenide using raman fingerprint," *Aip Advances*, vol. 7, no. 1, 2017.

[188] A. Bergeron, J. Ibrahim, R. Leonelli, and S. Francoeur, "Oxidation dynamics of ultrathin GaSe probed through raman spectroscopy," *Applied Physics Letters*, vol. 110, no. 24, 2017.

[189] V. Capozzi, "Direct and indirect excitonic emission in GaSe," *Physical Review B*, vol. 23, no. 2, p. 836, 1981.

[190] K. Allakhverdiev, N. Akhmedov, Z. Ibragimov, Ş. Ellialtioğlu, K. Lothar, and D. Haarer, "Low-temperature second harmonic generation in gallium selenide under resonant excitation of the direct free excitons," *Solid state communications*, vol. 93, no. 2, pp. 147–150, 1995.

[191] S. Nakamura, "Nobel lecture: Background story of the invention of efficient blue InGaN light emitting diodes," *Rev. Mod. Phys.*, vol. 87, pp. 1139–1151, 2015.

[192] L. Esaki, "A bird's-eye view on the evolution of semiconductor superlattices and quantum wells," *IEEE Journal of Quantum Electronics*, vol. 22, no. 9, pp. 1611–1624, 1986.

[193] M. Mikhailova and A. Titkov, "Type II heterojunctions in the GaInAsSb/GaSb system," *Semiconductor science and technology*, vol. 9, no. 7, p. 1279, 1994.

[194] J. Chen and A. Cho, "The effects of GaSb/InAs broken gap on interband tunneling current of a GaSb/InAs/GaSb/AlSb/InAs tunneling structure," *Journal of applied physics*, vol. 71, no. 9, pp. 4432–4435, 1992.

[195] C. Zhang, A. Johnson, C.-L. Hsu, L.-J. Li, and C.-K. Shih, "Direct imaging of band profile in single layer MoS_2 on graphite: quasiparticle energy gap, metallic edge states, and edge band bending," *Nano letters*, vol. 14, no. 5, pp. 2443–2447, 2014.

[196] C.-H. Lee, G.-H. Lee, A. M. Van Der Zande, W. Chen, Y. Li, M. Han, X. Cui, G. Arefe, C. Nuckolls, T. F. Heinz, *et al.*, "Atomically thin p-n junctions with van der Waals heterointerfaces," *Nature nanotechnology*, vol. 9, no. 9, p. 676, 2014.

[197] P. Rivera, H. Yu, K. L. Seyler, N. P. Wilson, W. Yao, and X. Xu, "Interlayer valley excitons in heterobilayers of transition metal dichalcogenides," *Nature nanotechnology*, p. 1, 2018.

[198] C. Jin, E. Y. Ma, O. Karni, E. C. Regan, F. Wang, and T. F. Heinz, "Ultrafast dynamics in van der Waals heterostructures," *Nature nanotechnology*, vol. 13, no. 11, p. 994, 2018.

[199] P. Rivera, J. R. Schaibley, A. M. Jones, J. S. Ross, S. Wu, G. Aivazian, P. Klement, K. Seyler, G. Clark, N. J. Ghimire, J. Yan, D. G. Mandrus, W. Yao, and X. Xu, "Observation of long-lived interlayer excitons in monolayer $MoSe_2$-WSe_2 heterostructures," *Nature communications*, vol. 6, p. 6242, 2015.

[200] P. K. Nayak, Y. Horbatenko, S. Ahn, G. Kim, J.-U. Lee, K. Y. Ma, A.-R. Jang, H. Lim, D. Kim, S. Ryu, H. Cheong, N. Park, and H. S. Shin, "Probing evolution of twist-angle-dependent interlayer excitons in $MoSe_2/WSe_2$ van der Waals heterostructures," *ACS Nano*, vol. 11, no. 4, pp. 4041–4050, 2017.

[201] H. Heo, J. H. Sung, S. Cha, B.-G. Jang, J.-Y. Kim, G. Jin, D. Lee, J.-H. Ahn, M.-J. Lee, J. H. Shim, H. Choi, and M.-H. Jo, "Interlayer orientation-dependent light absorption and emission in monolayer semiconductor stacks," *Nature communications*, vol. 6, p. 7372, 2015.

[202] J. Kunstmann, F. Mooshammer, P. Nagler, A. Chaves, F. Stein, N. Paradiso, G. Plechinger, C. Strunk, C. Schüller, G. Seifert, D. R. Reichman, and T. Korn, "Momentum-space indirect interlayer excitons in transition-metal dichalcogenide van der Waals heterostructures," *Nature Physics*, vol. 14, no. 8, p. 801, 2018.

[203] D. Fargues, L. Brahim-Otsmane, M. Eddrief, C. Sébenne, and M. Balkanski, "Study of the heterointerfaces InSe on GaSe and GaSe on InSe," *Applied surface science*, vol. 65, pp. 661–666, 1993.

[204] O. Lang, A. Klein, C. Pettenkofer, W. Jaegermann, and A. Chevy, "Band lineup of lattice mismatched InSe/GaSe quantum well structures prepared by van der Waals epitaxy: Absence of interfacial dipoles," *Journal of applied physics*, vol. 80, no. 7, pp. 3817–3821, 1996.

[205] O. Lang, A. Klein, R. Schlaf, T. Löher, C. Pettenkofer, W. Jaegermann, and A. Chevy, "InSe-GaSe heterointerfaces prepared by van der Waals epitaxy," *Journal of crystal growth*, vol. 146, no. 1-4, pp. 439–443, 1995.

[206] N. Balakrishnan, Z. R. Kudrynskyi, M. W. Fay, G. W. Mudd, S. A. Svatek, O. Makarovsky, Z. D. Kovalyuk, L. Eaves, P. H. Beton, and A. Patanè, "Room temperature electroluminescence from mechanically formed van der Waals III-VI homojunctions and heterojunctions," *Advanced Optical Materials*, vol. 2, no. 11, pp. 1064–1069, 2014.

[207] F. Yan, L. Zhao, A. Patanè, P. Hu, X. Wei, W. Luo, D. Zhang, Q. Lv,

Q. Feng, C. Shen, *et al.*, "Fast, multicolor photodetection with graphene-contacted p-GaSe/n-InSe van der Waals heterostructures," *Nanotechnology*, vol. 28, no. 27, p. 27LT01, 2017.

[208] W. Zhao, Z. Ghorannevis, L. Chu, M. Toh, C. Kloc, P.-H. Tan, and G. Eda, "Evolution of electronic structure in atomically thin sheets of WS_2 and WSe_2," *ACS Nano*, vol. 7, no. 1, pp. 791–797, 2013.

[209] M. Amani, P. Taheri, R. Addou, G. H. Ahn, D. Kiriya, D.-H. Lien, J. W. Ager III, R. M. Wallace, and A. Javey, "Recombination kinetics and effects of superacid treatment in sulfur-and selenium-based transition metal dichalcogenides," *Nano letters*, vol. 16, no. 4, pp. 2786–2791, 2016.

[210] N. Ubrig, E. Ponomarev, D. J. Terry, D. Domaretskiy, V. Zólyomi, J. Zultak, J. Howarth, I. Gutiérrez-Lezama, A. Zhukov, Z. R. Kudrynskyi, Z. D. Kovalyuk, A. Patanè, T. Taniguchi, K. Watanabe, R. V. Gorbachev, V. I. Fal'ko, and A. F. Morpurgo, "Design of van der Waals interfaces for broad-spectrum optoeletronics," *Nature Materials*, p. awaiting publication, 2019.

[211] X. Li, G. Jia, J. Du, X. Song, C. Xia, Z. Wei, and J. Li, "Type-II InSe/$MoSe_2$ (WSe_2) van der Waals heterostructures: vertical strain and electric field effects," *Journal of Materials Chemistry C*, vol. 6, no. 37, pp. 10010–10019, 2018.

[212] J. Zhang, X. Lang, Y. Zhu, and Q. Jiang, "Strain tuned InSe/MoS_2 bilayer van der Waals heterostructures for photovoltaics or photocatalysis," *Physical Chemistry Chemical Physics*, vol. 20, no. 26, pp. 17574–17582, 2018.

[213] H. Jiang, "Electronic band structures of molybdenum and tungsten dichalcogenides by the GW approach," *The Journal of Physical Chemistry C*, vol. 116, no. 14, pp. 7664–7671, 2012.

[214] P. Nagler, G. Plechinger, M. V. Ballottin, A. Mitioglu, S. Meier, N. Paradiso, C. Strunk, A. Chernikov, P. C. M. Christianen, C. Schller, and T. Korn, "Interlayer exciton dynamics in a dichalcogenide monolayer heterostructure," *2D Materials*, vol. 4, no. 2, p. 025112, 2017.

[215] B. Laikhtman and R. Rapaport, "Exciton correlations in coupled quantum wells and their luminescence blue shift," *Phys. Rev. B*, vol. 80, p. 195313, 2009.

[216] M. R. Molas, K. Nogajewski, A. O. Slobodeniuk, J. Binder, M. Bartos, and M. Potemski, "The optical response of monolayer, few-layer and bulk tungsten disulfide," *Nanoscale*, vol. 9, no. 35, pp. 13128–13141, 2017.

[217] C. Zhang, C.-P. Chuu, X. Ren, M.-Y. Li, L.-J. Li, C. Jin, M.-Y. Chou, and C.-K. Shih, "Interlayer couplings, moiré patterns, and 2D electronic superlattices in MoS_2/WSe_2 hetero-bilayers," *Science Advances*, vol. 3, no. 1, p. 1601459, 2017.

[218] F. Wu, T. Lovorn, and A. H. MacDonald, "Theory of optical absorption by interlayer excitons in transition metal dichalcogenide heterobilayers," *Physical Review B*, vol. 97, no. 3, p. 035306, 2018.

[219] H. Yu, G.-B. Liu, J. Tang, X. Xu, and W. Yao, "Moiré excitons: From programmable quantum emitter arrays to spin-orbit coupled artificial lattices," *Science Advances*, vol. 3, no. 11, p. 1701696, 2017.

[220] K. Tran, G. Moody, F. Wu, X. Lu, J. Choi, K. Kim, A. Rai, D. A. Sanchez, J. Quan, A. Singh, J. Embley, A. Zepeda, M. Campbell, T. Autry, T. Taniguchi, K. Watanabe, N. Lu, S. K. Banerjee, K. L. Silverman, S. Kim, E. Tutuc, L. Yang, A. H. MacDonald, and X. Li, "Evidence for moiré excitons in van der Waals heterostructures," *Nature*, vol. 567, no. 7746, pp. 71–75, 2019.

[221] C. Jin, E. C. Regan, A. Yan, M. Iqbal Bakti Utama, D. Wang, S. Zhao, Y. Qin, S. Yang, Z. Zheng, S. Shi, K. Watanabe, T. Taniguchi, S. Tongay, A. Zettl, and F. Wang, "Observation of moiré excitons in WSe_2/WS_2 heterostructure superlattices," *Nature*, vol. 567, no. 7746, pp. 76–80, 2019.

[222] K. L. Seyler, P. Rivera, H. Yu, N. P. Wilson, E. L. Ray, D. G. Mandrus, J. Yan, W. Yao, and X. Xu, "Signatures of moiré-trapped valley excitons in $MoSe_2/WSe_2$ heterobilayers," *Nature*, vol. 567, no. 7746, pp. 66–70, 2019.

[223] D. A. Ruiz-Tijerina and V. I. Fal'ko, "Interlayer hybridization and moiré superlattice minibands for electrons and excitons in heterobilayers of transition-metal dichalcogenides," *Phys. Rev. B*, vol. 99, p. 125424, 2019.

[224] E. M. Alexeev, D. A. Ruiz-Tijerina, M. Danovich, M. J. Hamer, D. J. Terry, P. K. Nayak, S. Ahn, S. Pak, J. Lee, J. I. Sohn, M. R. Molas, M. Koperski,

K. Watanabe, T. Taniguchi, K. S. Novoselov, R. V. Gorbachev, H. S. Shin, V. I. Fal'ko, and A. I. Tartakovskii, "Resonantly hybridized excitons in moiré superlattices in van der Waals heterostructures," *Nature*, vol. 567, no. 7746, pp. 81–86, 2019.

[225] C. Gong, H. Zhang, W. Wang, L. Colombo, R. M. Wallace, and K. Cho, "Band alignment of two-dimensional transition metal dichalcogenides: Application in tunnel field effect transistors," *Applied Physics Letters*, vol. 103, no. 5, p. 053513, 2013.

[226] K. Xu, Y. Xu, H. Zhang, B. Peng, H. Shao, G. Ni, J. Li, M. Yao, H. Lu, H. Zhu, and C. M. Soukoulis, "The role of anderson's rule in determining electronic, optical and transport properties of transition metal dichalcogenide heterostructures," *Physical Chemistry Chemical Physics*, vol. 20, no. 48, pp. 30351–30364, 2018.

[227] D. Kozawa, A. Carvalho, I. Verzhbitskiy, F. Giustiniano, Y. Miyauchi, S. Mouri, A. H. Castro Neto, K. Matsuda, and G. Eda, "Evidence for fast interlayer energy transfer in $MoSe_2/WS_2$ heterostructures," *Nano Letters*, vol. 16, no. 7, pp. 4087–4093, 2016.

[228] J. A. Wilson and A. D. Yoffe, "The transition metal dichalcogenides discussion and interpretation of the observed optical, electrical and structural properties," *Advances in Physics*, vol. 18, no. 73, pp. 193–335, 1969.

[229] W.-T. Hsu, Z.-A. Zhao, L.-J. Li, C.-H. Chen, M.-H. Chiu, P.-S. Chang, Y.-C. Chou, and W.-H. Chang, "Second harmonic generation from artificially stacked transition metal dichalcogenide twisted bilayers," *ACS Nano*, vol. 8, no. 3, pp. 2951–2958, 2014.

[230] D. Vaclavkova, J. Wyzula, K. Nogajewski, M. Bartos, A. Slobodeniuk, C. Faugeras, M. Potemski, and M. Molas, "Singlet and triplet trions in WS_2 monolayer encapsulated in hexagonal boron nitride," *Nanotechnology*, vol. 29, no. 32, p. 325705, 2018.

[231] G. Wang, X. Marie, I. Gerber, T. Amand, D. Lagarde, L. Bouet, M. Vidal, A. Balocchi, and B. Urbaszek, "Giant enhancement of the optical second-harmonic emission of WSe_2 monolayers by laser excitation at exciton resonances," *Physical Review Letters*, vol. 114, no. 9, p. 097403, 2015.

[232] A. Arora, K. Nogajewski, M. Molas, M. Koperski, and M. Potemski, "Exciton band structure in layered $MoSe_2$: from a monolayer to the bulk limit," *Nanoscale*, vol. 7, pp. 20769–20775, 2015.

[233] M. Koperski, M. R. Molas, A. Arora, K. Nogajewski, A. O. Slobodeniuk, C. Faugeras, and M. Potemski, "Optical properties of atomically thin transition metal dichalcogenides: observations and puzzles," *Nanophotonics*, vol. 6, no. 6, pp. 1289–1308, 2017.

[234] M. R. Molas, A. O. Slobodeniuk, K. Nogajewski, M. Bartos, Ł. Bala, A. Babiński, K. Watanabe, T. Taniguchi, C. Faugeras, and M. Potemski, "Energy spectrum of two-dimensional excitons in a non-uniform dielectric medium," *arXiv e-prints*, p. arXiv:1902.03962, 2019.

[235] K. F. Mak, K. He, C. Lee, G. H. Lee, J. Hone, T. F. Heinz, and J. Shan, "Tightly bound trions in monolayer MoS_2," *Nature materials*, vol. 12, no. 3, p. 207, 2013.

[236] Z. Wang, D. A. Rhodes, K. Watanabe, T. Taniguchi, J. C. Hone, J. Shan, and K. F. Mak, "Evidence of high-temperature exciton condensation in two-dimensional atomic double layers," *Nature*, vol. 574, no. 7776, pp. 76–80, 2019.

[237] M. Hamer, E. Tóvári, M. Zhu, M. D. Thompson, A. Mayorov, J. Prance, Y. Lee, R. P. Haley, Z. R. Kudrynskyi, A. Patanè, *et al.*, "Gate-defined quantum confinement in InSe-based van der Waals heterostructures," *Nano letters*, vol. 18, no. 6, pp. 3950–3955, 2018.